



**QUANTITATIVE ANALYSIS OF A
TURBULENT WIND TUNNEL WITH
OBSTRUCTIONS FOR USE IN LIQUID
FLAME SPREAD EXPERIMENTS**

THESIS

Beau M. C. Brantley, 2dLt, USAF

AFIT/GAE/ENY/06-M04

**DEPARTMENT OF THE AIR FORCE
AIR UNIVERSITY**

AIR FORCE INSTITUTE OF TECHNOLOGY

Wright-Patterson Air Force Base, Ohio

APPROVED FOR PUBLIC RELEASE; DISTRIBUTION UNLIMITED

The views expressed in this thesis are those of the author and do not reflect the official policy or position of the United States Air Force, Department of Defense, or the United States Government.

AFIT/GAE/ENY/06-M04

QUANTITATIVE ANALYSIS OF A TURBULENT WIND TUNNEL WITH
OBSTRUCTIONS FOR USE IN LIQUID FLAME SPREAD EXPERIMENTS

THESIS

Presented to the Faculty

Department of Aeronautics & Astronautics

Graduate School of Engineering and Management

Air Force Institute of Technology

Air University

Air Education and Training Command

In Partial Fulfillment of the Requirements for the

Degree of Master of Science in Aeronautical Engineering

Beau M. C. Brantley

2nd Lieutenant, USAF

March 2006

APPROVED FOR PUBLIC RELEASE; DISTRIBUTION UNLIMITED.

AFIT/GAE/ENY/06-M04

QUANTITATIVE ANALYSIS OF A TURBULENT WIND TUNNEL WITH
OBSTRUCTIONS FOR USE IN LIQUID FLAME SPREAD EXPERIMENTS

Beau M. Brantley, BS
2nd Lt, USAF

Approved:

//signed//

Ralph A. Anthenien (Chairman)

date

//signed//

Peter J. Disimile (Member)

date

//signed//

Paul I. King (Member)

date

Abstract

The research was done as part of an effort to develop alternative fire suppressant technologies for aircraft engine nacelles. The turbulent shear flow behind a surface mounted fence inside an open circuit wind tunnel was investigated experimentally. The tunnel test section was designed to be 2-D and exhibit flow qualities similar to those found in typical engine nacelles. A 279 mm wide fuel pan was inserted approximately four fence heights downstream of the fence location. The fuel pan was filled using water to simulate fuel with a depth of 32 mm. Cold flow tests were done on different fence configurations with turbulent airflow. The average turbulence intensity in the streamwise direction was 12% at the forward edge of the pan and with no fence in place. The Reynolds number was 2×10^4 in the free stream and based on a fence height of 50.8 mm. Several fences were used to simulate general types of clutter elements. The height, length, degree of perforation, and distance to the fuel pan were all fence geometries that were tested. Measurements were taken of the 2-D flow field along the centerline of the test section using Particle Image Velocimetry (PIV). A separation region with strong reverse flow was found to exist above the pan and have flow characteristics that were sensitive to fence dimensions. It was also found that the results for different configurations can be collapsed using the appropriate non-dimensional parameters. Future work will involve the flame spread over ethanol behind the same fence geometries in an effort to determine a correlation between nacelle clutter and liquid fuel flame spread.

AFIT/GAE/ENY/06-M04

To my Parents

Acknowledgments

I would like to give thanks to my advisor, Dr. Anthenien, for sharing with me his incredible depth and breadth of knowledge and for teaching me important aspects in engineering as both a science and a profession. I would also like to give my appreciation to Dr. Disimile, John Davis, and John Pyles with the 46th test wing for their invaluable assistance with this research endeavor.

My deepest gratitude goes to my parents for their unconditional love and support during my many years of education, and for all their funding too of course. Their humor, sincerity and wisdom are a rare combination. I would like to give special thanks to my father for instilling in me a desire to learn and for teaching me that I don't have to reach for the stars, but I should at least learn how they got there.

Beau M. C. Brantley

Table of Contents

	Page
Abstract.....	iv
Table of Contents	vii
List of Figures.....	ix
List of Tables	xiii
List of Symbols.....	xiv
Chapter 1. Introduction	1
1.1 - Problem Statement	1
1.1 - Objective.....	3
1.3 - Overview	4
1.4 - Preview	4
Chapter 2. Literature Review.....	6
2.1 - Background.....	6
2.2 - Historical Perspective.....	11
2.3 - Flame Spread Over a Liquid.....	15
2.4 - Pulsating and Precursor Flame Spread	19
2.5 - Flame Spread Regimes	21
2.6 - Effects of Fuel Pan Dimensions	27
2.7 - Flame Spread in Forced Airflow	28
2.8 - Separation Behind a 2-D Fence	35
2.9 - Particle Image Velocimetry	38
Chapter 3. Experimental Setup	41
3.1 - Wind Tunnel	41
3.2 - Clutter Elements	44
3.3 - PIV	47
3.4 - Preliminary Flame Spread Tests.....	57
Chapter 4. Results and Analysis	59
4.1 - Vorticity.....	60
4.2 - Turbulence Intensity	67
4.3 - Reynolds Stress.....	74
4.4 - Integral Length Scale.....	76
4.5 - Velocity Comparisons	79
4.6 - Curve Fitting.....	84
4.7 - Flame Spread Rates	87

Chapter 5. Conclusion.....	90
5.1 - Test Matrix Reduction.....	90
5.2 - Effects on Flame Spread Rate	91
5.3 - Recommendations for Future Work	93
Appendix A. Raw Data Velocity Contours.....	95
Bibliography	102

List of Figures

	Page
Figure 1. General representation of a recirculation region behind a two-dimensional fence in duct flow.....	11
Figure 2. General representation of flame spread rate over a liquid fuel [7].....	15
Figure 3. Diagram depicting induced liquid convection ahead of the flame due to surface tension gradient.	16
Figure 4. The flame spread rate for methanol at different bulk temperatures below and above the flash point [10].	22
Figure 5. Flame spread rate measurements for isopentanol and pentanol at 15 °C [12].....	30
Figure 6. Opposed and concurrent flow flame spread over methanol at various temperatures [14].	32
Figure 7. The recirculation length as a function of the blockage ratio for various fence aspect ratios [16].....	37
Figure 8. A typical PIV set up depicting the illumination and recording of particles to be correlated for each interrogation area.....	40
Figure 9. A diagram of the wind tunnel used in present research.....	41
Figure 10. Photograph of the inside of the wind tunnel showing the fuel pan, clutter element, and viewing windows.....	42
Figure 11. Photograph showing the underside of the fuel pan.	43
Figure 12. Grid spacing for the turbulence grid.....	44
Figure 13. Photograph of the turbulence grid.	44
Figure 14. Diagram showing the fence parameters varied.	46
Figure 15. Photograph of laser system used for PIV illumination.....	48
Figure 16. Photographs of the optical head (left) and the entire light guide (right), including the base mount, extension arm and optical head.	49
Figure 17. Redlake Megaplus CCD camera used for taking particle images.	50

Figure 18. Photograph of cyclone seeder used for injecting aluminum oxide particles into air stream.....	51
Figure 19. Diagram depicting the PIV setup used for the present research.....	51
Figure 20. Photograph showing the entire set up for PIV.....	52
Figure 21. Diagram depicting the streamwise range of the PIV images and the blind spot due to the distance between observation windows.	54
Figure 22. Picture of data acquisition location above the fuel pan. Tape measure extends to the edge of the original clutter location. The edge of the pan can be seen at approximately the 9 in mark.	60
Figure 23. Vorticity plots over the fuel pan for the three blockage ratios tested. Values are time averaged over 20 samples.....	62
Figure 24. Vorticity plots over the fuel pan for the three fence distances, lengths and perforation levels tested. Values are time averaged over 20 samples.....	64
Figure 25. Vorticity profiles for the blockage ratios tested at five different locations downstream of fence.....	66
Figure 26. Vorticity profiles for the levels of perforation tested at five different locations downstream of fence.....	67
Figure 27. Turbulence intensity (TI) over the fuel pan for 3 different blockage ratios.	69
Figure 28. Turbulence intensity (TI) over the fuel pan for 3 fence distances, perforation levels, and fence lengths.....	70
Figure 29. Non-dimensional TI profile comparisons for blockage ratios of $h/H = 1/9, 2/9, 3/9$	72
Figure 30. Turbulence profile comparisons for perforation levels of $P = 0, 7.6, 12.5$ and 19.1%	73
Figure 31. Reynolds stress above the fuel pan for different blockage ratios, h/H	75
Figure 32. Reynolds stress above the fuel pan for different fence positions, perforation levels and fence lengths.	76
Figure 33. Spatially determined streamwise integral length scale for all fence heights tested.	77

Figure 34. Spatially determined streamwise integral length scale for all fence distances tested, $x_p = 222, 171, 114$, and 57mm	78
Figure 35. Spatially determined streamwise integral length scale for all fence perforation tested, $P = 0, 7.6, 12.5$, and 19.1% . The length scale is averaged over 20 samples in time. Length scales were obtained from integration over a streamwise distance of 3 fence heights.....	78
Figure 36. Spatially determined streamwise integral length scale for all fence lengths tested, $L = 152, 305, 610$ and 1829mm	79
Figure 37. Non-dimensional velocity profile comparisons for blockage ratios of $h/H = 1/9, 2/9, 3/9$	80
Figure 38. Velocity profile comparisons for perforation levels of $P = 0, 7.6, 12.5$ and 19.1%	81
Figure 39. Velocity profile comparisons for fence lengths of $L/h = 12, 6$, and 3	82
Figure 40. Non-dimensional profile comparison for time averaged PIV data and data from Good and Joubert [0] for a blockage ratio of $1/9$	83
Figure 41. Comparison of curve fit equation and data for a blockage ratio of $2/9$. The Velocity is non-dimensionalized with the free stream velocity.....	85
Figure 42. Averaged velocity contour plot with overlaid streamlines at a location over the pan and for a fence height of 50.8 mm (original fence).....	95
Figure 43. Averaged velocity contour plot with overlaid streamlines at a location over the pan and for a fence height of 25.4 mm	96
Figure 44. Averaged velocity contour plot with overlaid streamlines at a location over the pan and for a fence height of 76.2 mm	96
Figure 45. Averaged velocity contour plot with overlaid streamlines at a location over the pan and for a fence perforation of 7.6%	97
Figure 46. Averaged velocity contour plot with overlaid streamlines at a location over the pan and for a fence perforation of 12.5%	97
Figure 47. Averaged velocity contour plot with overlaid streamlines at a location over the pan and for a fence perforation of 19.1%	98
Figure 48. Averaged velocity contour plot with overlaid streamlines at a location over the pan. Fence is located 57 mm upstream of leading edge of pan.....	98

Figure 49. Averaged velocity contour plot with overlaid streamlines at a location over the pan. Fence is located 114 mm upstream of leading edge of pan.....	99
Figure 50. Averaged velocity contour plot with overlaid streamlines at a location over the pan. Fence is located 171 mm upstream of leading edge of pan.....	99
Figure 51. Averaged velocity contour plot with overlaid streamlines at a location over the pan. The fence length is 152 mm along the width of the tunnel and is centered on the pan.....	100
Figure 52. Averaged velocity contour plot with overlaid streamlines at a location over the pan. The fence length is 305 mm along the width of the tunnel and is centered on the pan.....	100
Figure 53. Averaged velocity contour plot with overlaid streamlines at a location over the pan. The fence length is 610 mm along the width of the tunnel and is centered on the pan.....	101
Figure 54. Averaged velocity contour plot with overlaid streamlines at a location over the pan and with no fence in place.....	101

List of Tables

	Page
Table 1. Fence dimensions.....	46
Table 2. Test matrix.	46
Table 3. Flame spread rate for different fence configurations.	87
Table 4. Comparison of the average flame spread rate to the average air speed above the upstream half of the fuel pan. Negative air speeds indicate opposed direction of flow or lack of reverse flow.	88

List of Symbols

Nomenclature

CCD = Charged Couple Device

CTA = Constant Temperature Anemometry

D = Damköhler Number, or diameter of fence holes [mm]

d = Distance between fence holes [mm]

FFT = Fast Fourier Transform

H = Height of wind tunnel [mm]

h = Fence height [mm]

h_f = Fuel depth [mm]

LDA = Laser Doppler Anemometer

L = Fence length [mm]

L_r = Length of recirculation region [mm]

m = Row number

N_H = Number of fence holes

n = Number of data points, or column number

PIV = Particle Image Velocimetry

P = Percent perforation

RMS = Root Mean Square

Re = Reynolds number

Re_h = Reynolds number based on fence height

S = Vorticity scalar [1/s]

s = Surface point

T = Temperature [$^{\circ}$ C]

TI = Turbulence Intensity

t_{flow} = Residence time [s]

t_{chem} = Chemical reaction time [s]

U = Velocity in streamwise direction [m/s]

\bar{U} = Average velocity in streamwise direction [m/s]

U_{rms} = Root mean square velocimetry [m/s]

U_1 = Average streamwise velocity without a fence [m/s]

U_o = Average free stream velocity for original fence configuration [m/s]

U_∞ = Free stream velocity [m/s]

u' = Fluctuating component of streamwise velocity [m/s]

u = Liquid surface velocity [m/s]

V = Velocity in crosswise direction [m/s]

V_f = Flame spread rate [cm/s]

V_L = Laminar burning velocity [cm/s]

v' = Fluctuating component of crosswise velocity [m/s]

X_p = Distance from fence face to forward edge of fuel pan [mm]

x = Direction parallel to tunnel surface, or distance downstream of fence [mm]

y = Direction perpendicular to tunnel surface, or distance above tunnel surface [mm]

Symbols

α = Constant for predicting flame spread rate

Δ = Change in

Λ = Integral length scale [m]

μ = Viscosity [N·s/m²]

ρ = Density [kg/m³]

ρ_b = Density of products [kg/m³]

ρ_u = Density of unburned gas [kg/m³]

σ = Standard deviation or surface tension [N]

τ = Shear stress [N/m²]

QUANTITATIVE ANALYSIS OF A TURBULENT WIND TUNNEL
WITH OBSTRUCTIONS FOR USE IN LIQUID FLAME SPREAD
EXPERIMENTS

Chapter 1. Introduction

1.1 Problem Statement

Aircraft engine nacelles create an environment amenable to fires due to multiple fuel and ignition sources, thereby making fire suppression and prevention of re-ignition difficult. There exist many types of obstructions in the form of avionics, fluid lines, wiring, and structural components, such as ribs [1]. These sources of clutter within the nacelle provide many possible locations for fuel to accumulate. The accumulation of fuel forms a pool of liquid that can be ignited from one of the many ignition sources within the nacelle [1]. These conditions are exacerbated by the temperature of the fuel under normal operating conditions, which can be as high as 150 °C [2].

Successful suppression of a nacelle fire depends on the concentration and effectiveness of the suppressing agent and the flow field dynamics [3]. Extinction of the flame occurs when the time required to complete the necessary chemical reaction is much longer than the residence time of the reactants [4]. That is, the combustion process lacks the time required for completion when the chemical rate of reaction is smaller than the flow rate. As a result, the flame cannot sustain itself without the heat produced by the

chemical reaction. The ratio of the chemical time to the flow time is called the Damköhler number.

$$D = \frac{t_{flow}}{t_{chem}} \quad (1)$$

It is a parameter that represents the aforementioned effects [3]. The dependence of the Damköhler number on the flow time makes it very sensitive to the flow field characteristics, especially when dealing with opposed flow, as can be the case inside an engine nacelle. Opposed flow will decrease the fuel vapor residence time and reduce the vapor pressure. The Damköhler number decreases with increasing velocity of the forced air flow [4]. It decreases until reaching a critical value and then the flame becomes extinct [3]. The clutter contained inside the nacelle can essentially alter the airflow experienced by the flame and affect its ability to sustain itself or spread. This is why it is so important to understand the flow field dynamics within a typical engine nacelle.

For the past several decades, a fire suppressing agent called trifluorobromomethane (CF_3Br) [3], known as halon 1301, has been used to control engine fires [1]. Halon extinguishes the fire by robbing the combustion process of its much needed hydrogen radicals. Halon 1301 is very effective because only a small concentration (6% for 0.5 seconds) is required for successful suppression [5]. In fact, it was so effective that there was never any need to characterize the flow field to optimize dispersion inside an engine nacelle [1]. It also has other beneficial characteristics, such as a large effectiveness to weight ratio and physical properties that allow it to be transported as a liquid [5]. These properties make halon ideal for use in aviation. Unfortunately, halon also depletes the stratosphere of ozone and the Montreal Protocol

stopped its production in 1994 [5]. Several alternatives to halon have been developed and tested, but of those that meet health and environmental standards, none provide the effectiveness needed in terms of suppression effectiveness per weight of the system [1]. The effectiveness is also dependent on the engine environment since clutter in the nacelle can obstruct and alter the transport of fire suppressant. As mentioned before, nacelle clutter also affects the flow field and can directly influence flame spread.

Obstructions in the nacelle can cause turbulent shear flow, creating areas of entrainment that can increase the residence time of the chemical reactants and retain heat. For this reason, fires often form and stabilize behind an obstruction when in strong air flows. The clutter inside an engine nacelle can also influence flame spread characteristics by affecting vital heat transfer mechanisms, such as gas-phase and liquid-phase convection. Little or no research has been conducted on liquid fuel flame spread under turbulent flow conditions and only a handful have investigated the effects of laminar flow. As a result, the information on this topic is lacking and further investigation is required.

1.2 Objective

The purpose of this research is to characterize the various flow field geometries using general clutter elements so as to provide improved understanding of the engine nacelle environment and its influence on liquid flame spread. This information is needed by those researching a suppressant transport model to use with the computational fire code in development at Sandia National Laboratory. The data acquired in collaboration

with the 46th Test Wing at Wright-Patterson AFB will provide further insight into the clutter/flame spread interactions and the nacelle environment.

1.3 Overview

A two-dimensional engine nacelle was simulated by utilizing a narrow wind tunnel with turbulent flow. Several configurations of obstructions were placed within the tunnel to simulate different types of clutter found inside a typical engine nacelle. Each type of obstruction consisted of a fence with a single parameter that varied from the original fence used by Disimile and Davis [6]. The parameters that varied consisted of the fence height, length, distance to the fuel pan, and level of perforation (holes placed along the fence). For each of these fence configurations, the flow fields behind the fence and over the fuel pan were measured using particle image velocimetry (PIV). The resulting images were analyzed using the Dantec Dynamics FlowManager software and the findings are reported in this paper.

1.4 Preview

Work done in previous investigations, and information on PIV is provided in the literature review in the following chapter, chapter 2. A section with background information is provided at the beginning of chapter 2 and provides general information on flame spread over liquids and turbulent shear flow behind a 2-D fence. Chapter 3 gives a comprehensive layout of the experimental methods employed. This section provides detailed information on the equipment, experimental parameters, and procedures used during testing. The results are reported in chapter 4, along with an analysis of the

acquired data. This section includes velocity profile comparisons, vorticity, turbulence intensity, and Reynolds stress contour plots, along with velocity curve-fit equations. A discussion of these results and their implications are provided in the final chapter, chapter 5. This chapter also mentions possibilities for future work and includes a conclusion that highlights the major findings. Appendices containing the raw data in the form of velocity contour plots overlaid with streamlines can be found in the back.

Chapter 2. Literature Review

2.1 Background

2.1.1 Flame Spread Across a Liquid Fuel

Flame spread is an area of research that has been the subject of numerous investigations due to its importance in fire safety. In past years, the flame spread over solids has been the primary focus of experimentation, because of its many applications to fire safety. Several studies have also been conducted on flame spread across liquids, although not enough to fully understand its complex nature. Most of the confusion about flame spread over liquids is due to the changing heat transfer mechanisms that can quickly give way to other mechanisms. The controlling mechanisms that govern flame spread over pools and when they are most important is still an issue of debate to this day.

Flame spread occurs when a sufficient amount of fuel has collected in one place within the vicinity of an ignition source. If the liquid bulk temperature is too low, the ignition source must raise the local temperature to increase the vapor pressure so as to create a combustible mixture [7]. There will be a momentary premixed flame once the fuel vapor and air mixture is ignited. This initial flame will stabilize if the local temperature is such that the vapor production is high enough to sustain the combustion process. The temperature at which this occurs and the temperature required for ignition is the same for several fuels such as alcohols [8]. However, these temperatures are different for hydrocarbons and this produces an interesting effect called precursor flame spread [7].

The flame propagates across a pool by heating the liquid ahead of the flame to the lowest temperature at which a combustible mixture will exist above the surface. The manner in which the fuel ahead of the flame is heated comprises of several different mechanisms, including liquid convection, gas-phase convection and conduction, and to some extent, radiation. The temperature of the fuel is the determining factor in which of these mechanisms are present and which ones control the rate of spread [8].

The temperature at which the air/fuel mixture above the fuel surface is within the lean limit of combustion is known as the flash point [7]. Flame spread behavior changes radically depending on the bulk temperature relative to the flash point. Flame spread is controlled by the liquid-phase at temperatures below the flash point, but is controlled by the gas-phase at temperatures above the flash point [9]. However, there exists a transition region in which both mechanisms apply and perhaps others. This region is called the uniform region and occurs just below the flash point and its complex nature is not yet entirely known [10].

The temperature region below the flash point is the most complicated and the most investigated region of flame spread over liquids. This region is often the area of interest, because of the liquid convection induced by the flame. Liquid convection is the primary mode of heat transfer for flame propagation below the flash point [11]. It is also known to play a major role in a phenomena known as pulsating or precursor flame spread. Pulsating and precursor flame spread is fundamentally different. However, the two are mentioned together because the visual effects are relatively similar. So much so, that early investigations into the topic produced conclusions that made little distinction between the two.

Pulsating/precursor flame spread is when the flame spread rate fluctuates between a high and a low velocity that are separated by an order of magnitude [10]. The high velocity, also known as the jump velocity, is around the same order of a premixed flame. The low, sometimes referred to as the creep, velocity has values associated with a normal diffusion flame [8].

After the liquid in front of the flame front has been heated to the flash point, the flame then leaps through the combustible mixture. This flame is known as a premixed flame and is called such, because the fuel vapor and oxidant are already mixed well before the combustion process takes place. The flame that anchors itself in a portion of the premixed region, just behind the premixed flame, is called the diffusion flame. A diffusion flame must first heat the fuel and transform it into a vapor so that it can diffuse and mix with the oxygen. The mixture is combusted once it is formed, creating the flame front. The diffusion flame propagates at speeds much slower than the premixed flame, because it has to continually heat the fuel, which requires time [8].

When the bulk temperature of the fuel is greater than the flash point, a fuel/air mixture with just enough fuel vapor to support combustion exists everywhere above the surface. It also exists at a distance that allows the flame to continually propagate without any deceleration in flame spread rate. The minimum distance from the fuel surface at which the flame can sustain itself is known as the quenching distance [7].

Flame propagation in the gas-phase region, which is above the flash point, is very simple in comparison to flame spread below the flash point. The only exception is that the equivalence ratio changes with height such that the mixture is stratified and non-uniform. The equivalence ratio is a parameter that compares the levels of oxidizer and

fuel. Flame spread above the flash point consists of a premixed flame and is controlled by gas-phase mechanisms [10].

From the above information, it is easy to understand why the flash point of a fuel is one of its most important characteristics. Fuels are often engineered to exhibit a desired flash point for reasons of safety and performance. The U.S. Navy currently uses modified kerosene called JP-5, which is a jet fuel with a high flash point of 60 °C. The high flash point helps prevent fires from fuel spills on the decks of aircraft carriers. JP-8 is a newer jet fuel used by the U.S. Air Force and has a lower specified flash point of 38 °C [9].

2.1.2 Flame Spread Across Liquid Fuels in Opposed Airflow

Very little experimental work has been done on forced flow flame spread over liquid fuels. What is known is that low velocity air currents have very little effect on flame spread rates [12, 13, 14]. The opposed velocity would have to be greater than that of the induced air velocity caused by buoyancy to significantly alter the flame spread characteristics. Also, the presence of the flame front slows the forced air speed in the vicinity of the flame. However, low velocity air currents can alter the pulsation frequency of the flame [13].

Like most liquid flame spread characteristics, the effects of opposed flow depend on the temperature of the fluid relative to its flash point. Changes in flame spread rate are greater when above the flash point than when below [12]. The flame travels by means of gas-phase mechanisms when above the flash point and is more susceptible to air currents. Flame spread below the flash point shows very little reaction to low and even moderate opposed air speeds and ceases to spread at velocities much greater than the zero opposed

flow flame spread rate [14]. How high speed air currents affect liquid-phase heat transfer mechanisms and their relative effects on spread rate is unknown and of great interest.

2.1.3 Downstream Effects of a 2-D Fence in Turbulent Flow

When a fence (or any blunt object) is placed in the path of oncoming flow, it causes the boundary layer to detach from the surface on which that object is placed. This phenomenon is known as separation. Separation occurs when an adverse pressure gradient causes the fluid particles adjacent to a surface to reverse in direction. These particles are particularly sensitive to changes in pressure because of their lack in momentum due to viscous effects. Because they have much less momentum than the particles in the upper regions of the boundary layer, they are unable to overcome any pressure “humps” due to sudden changes in flow direction, such as flow around a sharp corner or a vertical wall. The flow reversal of only the lower momentum particles causes a swirling motion that creates vortices.

The flow past a 2-D fence (shown in Figure 1) is especially complicated because it is both blunt and thin, forcing the flow to deal with multiple changes in flow direction over a short period of time. This creates two separation regions with reverse flow, a small region upstream of the fence and a much larger separation region downstream of the fence [15]. The reverse flow region downstream of the fence is separated from the free-stream by a shear layer. This boundary is marked by a thick line shown in Figure 1 extending from the tip of the fence and reattaching downstream. This figure is not drawn to scale and is a qualitative representation of a 2-D fence in duct-flow, such as the kind under current investigation. The length and height of the separation region is dependent

on many flow characteristics, but mainly on the height of the duct and fence, the Reynolds number, and the free stream turbulence level [16].

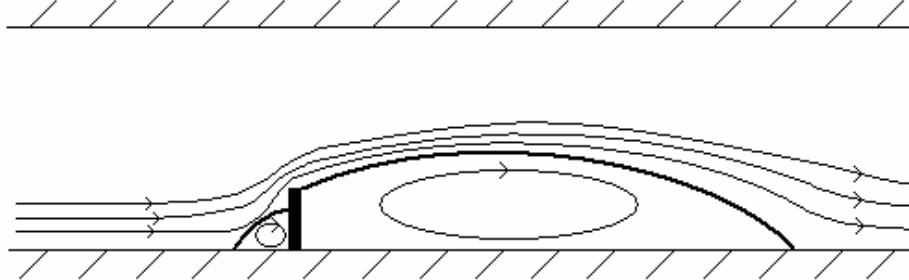


Figure 1. General representation of a recirculation region behind a two-dimensional fence in duct flow.

The presence of Turbulence has a direct effect on the separation region because of the transport of momentum from the free-stream to the wall. Increased levels of turbulence will delay the onset of separation for boundary-layer flow and decrease the length of the separation region for the case of a blunt object.

2.2 Historical Perspective

Flame spread is an area of extensive research. It is important because of its contribution to fire safety, which is why most experimental investigations have been focused on flame spread across solids and not liquids. However, many investigations have been focused on discovering the nature of flame spread across liquids and have revealed that this phenomenon is much more complicated than expected.

Burgoyne and Roberts [12] provided valuable observations and measurements on flame spread over liquid fuels. They conducted experiments on pools of propanol, butanol, isopentanol, and hexanol and examined the changes of flame spread rate with various changes in experimental conditions. Among these were liquid temperature, pool

depth, pool width, forced liquid currents, and forced air currents. Their work on forced air currents is especially important because only two other groups of researchers after them performed experimental investigations on opposed flow flame spread. Therefore, the amount of data available on this topic is limited.

Nearly a decade before his work with Burgoyne, Roberts [17] wrote his PhD thesis on flame spread over a liquid surface, in which he provided valuable observations on flame spread behavior. He noted the discrepancy between laminar premixed spread rates and the spread rates of a flame above a liquid surface. His work on low flash point fuels showed that propagation rates over a liquid fuel, whose bulk temperature was such that stoichiometric conditions existed above the surface, reached 200 cm/s. These measured velocities are four to five times greater than that for normal laminar stoichiometric flame spread [7]. Roberts [17] also noticed that the flame spread rate would pulsate at certain temperatures, cycling between velocities associated with diffusive flame spread and laminar flame spread. In addition to the above observations, Roberts determined that flame propagation above a liquid tended to induce currents in the liquid.

The primary focus of following investigations became the different phenomena associated with liquid flame spread and why they occur. A great deal of interest was focused on the induced liquid convection and the cause of this phenomenon. It would later be the work of Glassman [7, 11, 18] and his colleagues at Princeton that would determine the link between flame spread and induced liquid convection.

The work done at Princeton began shortly after that of Burgoyne and Roberts. They determined that the convection currents in a liquid fuel are caused by surface

tension gradients created by the high temperatures beneath the flame and the much lower surface temperatures away from the flame [18]. It was then determined that liquid convection is the main heat transfer mechanism responsible for flame spread at temperatures below the flash point [18]. This was shown through several experiments conducted by MacKinven et al. [11], including one where the viscosity of the liquid was altered in order to determine its relationship with the flame spread rate. They also discovered that radiation contributed little to the overall heat transferred to the liquid ahead. They determined this by blocking the radiation and observing insignificant changes in the flame spread rate.

In 1982, Suzuki and Hirano [14] published what seems to be the most extensive work done on opposed and concurrent flow flame spread across a liquid fuel. They performed experiments on methanol in a 100.8 cm long tray that was 4.2 cm wide and 3.3 cm deep. The flame behavior was examined using high-speed Schlieren photography. Flame spread rates were measured for air velocities ranging from -600 cm/s to 600 cm/s and liquid bulk temperatures ranging from 5 °C to 30 °C. Hirano and Suzuki [14] discovered that low air speeds only moderately affect the flame spread rate. They observed that the air speed at which the flame spread rate terminates is much greater than the zero flow flame spread rate. Even more interesting, was their discovery that the flame spread rate matches the concurrent air velocity at speeds greater than 200 cm/s, regardless of what the initial temperature of the fuel is.

Ross and Miller [13] appear to be the only other researchers to engage in experimental investigations of flame spread over liquids in forced air flow and published their work in 1998. They used an alcohol, 1-butanol, in a 30 cm long pan that was 2cm

wide by 2.5 cm deep with opposed and concurrent airflow ranging from 5 to 30 cm/s.

Unlike Suzuki and Hirano [14], or Burgoyne and Roberts [12], the work done by Ross and Miller [13] included the effects of forced air currents as they pertain to liquid convection and flame spread pulsation. They found that changes in slow forced air currents do not alter the flame spread rate, but they do influence the pulsation frequency. Lower opposed flow speeds create higher pulsation frequencies that continue to increase as the flow transitions to concurrent flow [13].

The flow of air past a 2-D obstacle is a topic that has received a great deal of attention because of its many applications. Good and Joubert [19] in 1967 were among the first to do extensive experimental research on 2-D fences immersed in turbulent flow. They used a blockage ratio (fence height over tunnel height), h/H , of 0.11 and a Reynolds number of $Re_h = 1.76 \times 10^5$. They discovered that the separation region under such conditions extended more than 13 fence heights downstream of the fence and that reverse flow velocities were as much as half the free-stream velocity, the largest of the reverse flow velocities being found close to the bottom surface of the duct.

Durst and Rastogi [16] studied turbulent flows over 2-D obstructions in 1979. They used blockage ratios varying from 0 to 0.5 and compared calculations done with the same flow conditions as that of Good and Joubert to their data. Their measured data on the separation region showed that the reattachment length is nearly the same for different fence heights that have the same width and blockage ratio. Their calculations showed that accurate results can be obtained using corrections for streamline curvature.

Schofield and Logan [15] studied both two-dimensional and three-dimensional surface mounted obstructions in turbulent flow over a wide range of flow fields and

obstacle geometries [15]. They determined that the recovery length for the separation region behind a three-dimensional object is significantly shorter than the region behind a two-dimensional object. The flow field around a three-dimensional object contains several interacting vortices that travel streamwise and pass through the separation region so as to disrupt the closed “bubble” that exists behind two-dimensional obstructions.

2.3 Flame Spread Over a Liquid

Flame propagation over liquids is a complicated phenomenon that is not yet entirely understood. There are different heat transfer mechanisms at work depending on the initial temperature of the liquid fuel. The most important factor that governs flame spread is whether the liquid bulk temperature is below or above the flash point of the fuel. A graphical representation of this relationship is shown in Figure 2 for a generic fuel and is based on the figure presented in Glassman et al. [7].

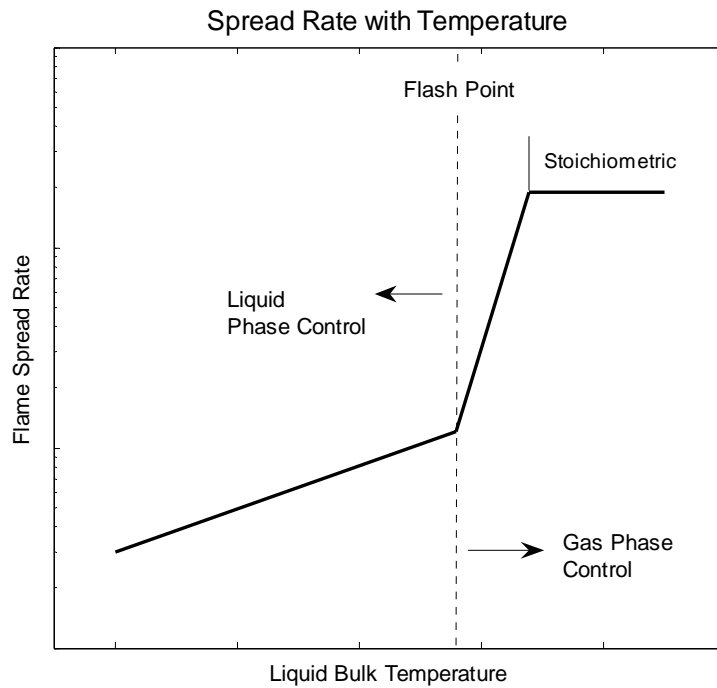


Figure 2. General representation of flame spread rate over a liquid fuel [7].

2.3.1 Liquid Convection

Flame spread below the flash point is liquid-phase controlled [9]. Meaning, that liquid convection controls the heat transfer to the liquid ahead of the flame front. This is accomplished through a liquid circulation region beneath the surface that extends out ahead of the flame front [8]. Liquid convection is a result of the surface tension gradients created by the temperature difference between the liquid below the flame front and the liquid ahead [4]. The surface tension far ahead of the flame is much larger than the surface tension below the flame, because it is inversely proportional to temperature and the liquid temperature below the flame is much higher than the bulk temperature [4]. This causes the surface tension to pull the liquid along the surface away from the flame. The fluid directly below the surface moves in the same direction due to the viscous nature of the fluid. The viscous forces create a flow that is similar in nature to the well-known Couette flow [7]. A diagram of this phenomenon is presented below as Figure 3.

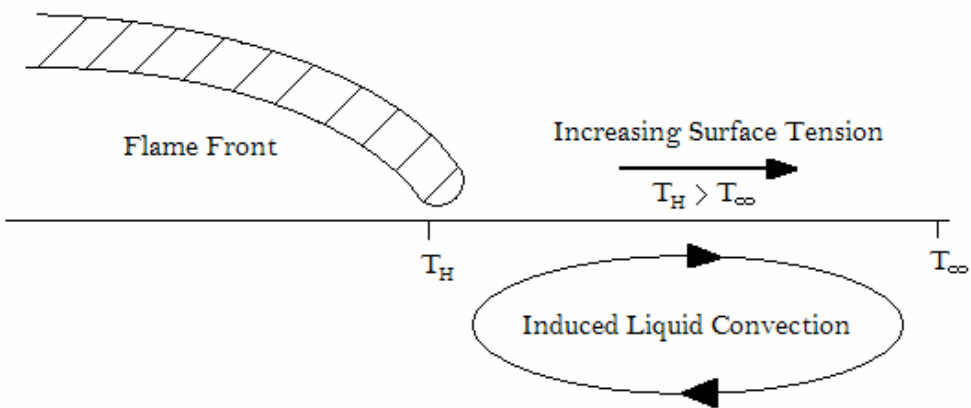


Figure 3. Diagram depicting induced liquid convection ahead of the flame due to surface tension gradient.

Sirignano and Glassman [18] worked on the theory of surface-tension-driven flows to predict the behavior of liquid-phase controlled flame spread. They postulated that the shear stress at the surface of the liquid is equal to the surface tension gradient.

$$\tau = \mu \left(\frac{\partial u}{\partial y} \right)_s = \sigma_x = \left(\frac{d\sigma}{dT} \right) \left(\frac{\partial T}{\partial x} \right) \quad (2)$$

Where τ is the liquid shear stress, μ is the viscosity, u the velocity along the surface, y is the direction perpendicular to the surface, s is the surface point, σ represents the surface tension, T is the temperature, and x is in the direction parallel to the surface. The above equation provides the following relation for the velocity of the liquid at the surface [18].

$$u_s \sim \frac{\sigma_x h_f}{\mu} \quad (3)$$

Here, h_f represents the height of the fuel, or fuel depth. The flame spread rate is dependent on the velocity at the surface, because liquid convection is the primary mode of heat transfer [18]. If the liquid convection were to decrease, then the flame spread rate must also decrease due to insufficient fuel vapor production caused by the decline in heat transfer. The above relation implies that the flame spread rate is inversely proportional to the viscosity and proportional to the surface tension and the fuel depth. Mackinven et al. [11] and Burgoyne and Roberts [12] confirmed this relation by varying temperature, fuel depth and viscosity.

2.3.2 Coupled liquid and gas convection

There also exists a naturally induced gas recirculation region ahead of the flame front due to the no-slip condition with the liquid surface [8]. As the liquid surface moves in the direction away from the flame, the gas directly above the surface is forced to travel with it. However, there is also gas convection traveling in the opposite direction due to buoyancy effects. The induced air flow towards the flame is on the order of 10 to 30 cm/s [13]. The air in front of the flame is hot and rises quickly, pulling along the air behind it. The combination of gas convection in opposite directions creates a recirculation region.

The gas recirculation region is very important to the combustion process, because it retains heat and fuel vapor in front of the flame. It also improves the mixing of the fuel vapor and oxygen and the dispersing of the mixture to be used by the flame [8]. The depth of the recirculation region is extremely small, typically less than a millimeter, as shown by particle streak photographs taken by Sanatro et al. [20]. LDV measurements taken by the same researchers were incapable of measuring the extremely shallow recirculation zone. They did, however, uncover a very complex flow pattern directly ahead of the flame. This is to be expected since there are conflicting directions of flow due to the rising of hot gas and the no-slip condition with the liquid surface.

The no-slip condition also acts to extend the gas recirculation zone to the far end of the liquid convection boundary. There is little data on the distance that liquid convection travels ahead of the flame front. However, Helmsetter found this distance to be approximately 21 cm when taking measurements of a flame traveling at an average velocity of 1.5 cm/s across an alcohol fuel [21].

Liquid convection is closely related to the pulsating phenomenon known to occur in flame spread over liquid fuels whose bulk temperatures are below the flash point. Ross [8] pointed out that Takeno and Hirano demonstrated the importance of liquid convection to pulsating flow by soaking the fuel in a bed of beads and then observing the elimination of pulsating behavior [22]. The beads restricted liquid convection and demonstrated that it is closely linked to pulsating flame spread.

2.4 Pulsating and Precursor Flame Spread

Pulsating flame spread is sometimes referred to as precursor flame spread and is a phenomenon that is unique to flame spread across liquid fuels. A faster moving premixed flame precedes the stabilized portion of the flame, also known as the diffusion flame. The fuel and oxidizer are already mixed and allows the flame to spread, or jump, through the mixture at a higher rate of speed. The flame stops when it reaches where the mixture is no longer in the flammability limit and must wait for pre-heat mechanisms to reestablish before jumping again [8].

2.4.1 Precursor Spread

Precursor flame spread and pulsating flame spread are sometimes referred to as the same phenomenon, but are actually separate occurrences. Precursor typically occurs in hydrocarbon fuels and is a result of there being a significant difference between the flash point temperature and the fire point temperature. The fire point is the temperature at which the production rate of vapor is enough to sustain a steady flame and is typically higher than the flash point for hydrocarbon fuels [7].

During precursor flame spread, the liquid ahead of the flame is heated to the flash point through liquid convection. A blue precursor flame quickly spreads though the combustible mixture above the surface and then extinguishes because the surface temperature is below the fire point. The process is repeated several times and the precursor flame eventually heats the surface temperature to the fire point and a stable flame can be supported [7].

2.4.2 Pulsating Spread

Pulsating flame spread is caused by complex interactions between liquid convection and gas-phase mechanisms. As with precursor flame spread, the pulsations are linked to liquid convection. Surface tension gradients cause the warmer liquid beneath the flame to travel to the regions ahead of the flame front [18]. This continues until the surface temperatures reach the flash point and a flame quickly accelerates though the fuel vapor above the surface. But unlike fuels that exhibit precursor flame spread behavior, pulsating spread occurs in fuels with similar flash and fire point temperatures and the flame is instantly stabilized after acceleration and does not retreat as it does in precursor flame spread [8]. Liquid convection is once again established beneath the diffusion flame and the cycle begins again.

The cause of the pulsations is not entirely agreed upon. However, one of the largely supported theories is that the pre-mixed flame catches the convective flow head of the liquid and is forced to stop and wait while new convective currents are established [10]. The flame can still advance in its diffusion state, but it must wait for the convective currents to form and heat the liquid ahead to the flash point before it can once again jump

forward. This implies a strong relationship between the pulsation frequency and the fuel warm up time.

Pulsating behavior may be closely linked to liquid-phase mechanisms, but it does not occur for all initial temperatures below the flash point. Experiments performed by Akita revealed that pulsating behavior only occurs within an initial temperature range he referred to as the uniform region [10]. The uniform region is just below the flash point and is one of several temperature regimes that will be discussed in the following section.

2.5 Flame Spread Regimes

Akita performed extensive tests on methanol in a wide variety of temperature ranges in order to get a better understanding of pulsating flame spread behavior as well as other flame spread behaviors [10]. He conducted experiments using a 100 cm long, 2.6 cm wide, and 1 cm long pan. Most of the flame spread measurements done around that time utilized relatively narrow pans. Akita found that flame spread, at least as it pertains to alcohols, can be grouped into three different spread regimes that exist under the flash point. Akita referred to these three regions as pseudo-uniform, pulsating, and uniform. Each regime is characterized by a specific temperature range and unique flame behavior. Two regimes with similar flame spread behavior exist above the flash point and are referred to as the gas-phase controlled and stoichiometric regions.

These five different flame spread regimes are each characterized by different changes in flame spread rate with initial fuel temperature. The different slopes make them easily distinguishable on a chart with a logarithmic vertical axis, as can be seen in Akita's results with methanol as shown in Figure 4 [10]. Each region is associated with a

temperature range relative to the flash point of the fuel and fall under the sub-flash category (liquid-phase controlled) or the super-flash category (gas-phase controlled). The heat transfer mechanisms that control the flame spread in each of these regions are not entirely agreed upon, but what is universally accepted is that the flame spread rate is greatly dependent on the temperature relative to the flash point.

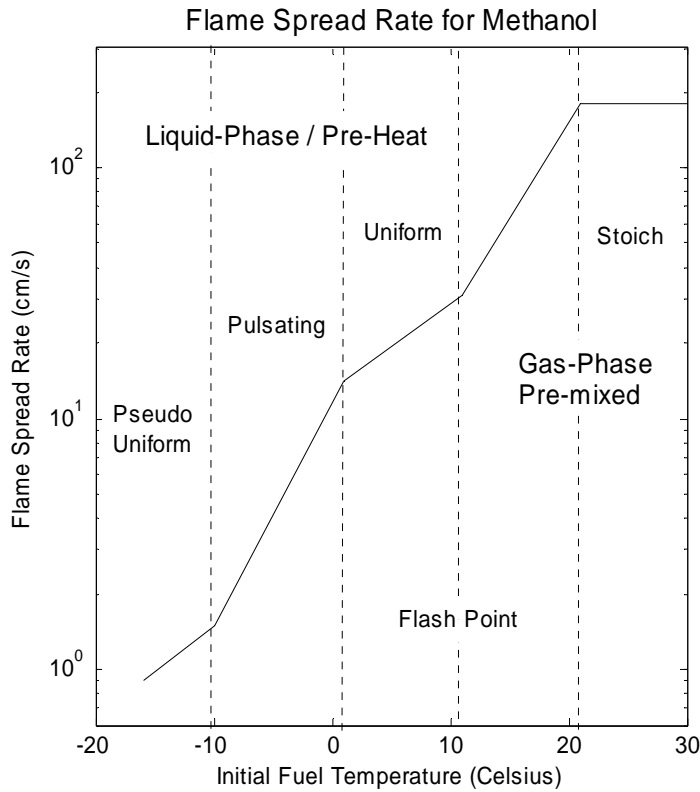


Figure 4. The flame spread rate for methanol at different bulk temperatures below and above the flash point [10].

2.5.1 Pseudo-Uniform

The pseudo-uniform stage lies at the coolest end of the liquid-phase, sub-flash region, also sometimes referred to as the pre-heat region, because the fuel ahead of the flame must first be pre-heated before flame spread can occur. This regime is given the name “pseudo-uniform”, because the pulsations in the flame spread rate seem to

disappear. However, it is thought that the flame spread rate is still pulsating, but the distance the flame jumps with every cycle is longer than the length of the pan [8]. Another possibility, as Akita mentioned, is that the interval between each cycle is large enough to give the appearance of uniform flame spread [10]. Akita noticed that, for methanol, the pulsation interval increases rapidly with decreasing initial fuel temperature. This is because the decrease in temperature results in a stronger surface tension gradient that extends the length of the liquid recirculation region. As mentioned before, the sub-flash region is dominated by liquid-phase heat transfer mechanisms, but this is particularly true for the pseudo-uniform regime.

2.5.2 Pulsating Regime

The pulsating regime is characterized by periodic acceleration and deceleration of the flame spread rate. These pulsations are strongly linked to the surface tension driven convection of the liquid as mentioned previously, but it is unsure whether or not convection is required for pulsating flame spread to occur. The temperature range, in which this behavior occurs, changes with different fuel types but also varies with fuel pan parameters [12, 11, 8, 23].

The pulsation characteristics are greatly dependent on liquid temperature, due to the strong connection between pulsating flame spread and surface flow. This is evident by the data presented by Akita and Fujiwara for methanol depicting the pulsation interval as a function of liquid temperature [24]. They observed that the pulsation interval climbs rapidly as the temperature is reduced, reaching 30 cm at -8 °C and continuing to climb exponentially as it approaches -10 °C. Their data also shows that the time interval for each pulsation cycle is approximately 1.5 seconds for methanol at -2.7 °C and fluctuates

between 4 and 16 cm/s. The crawl spread rate is that of a diffusion flame, and the jump velocity is on the order of a laminar pre-mixed flame.

2.5.3 Uniform Regime

As the name implies, the flame spread rate in the uniform regime is consistent with time. The pulsating behavior from the previous regime no longer exists. The uniform regime is by far the least understood temperature region of flame propagation across pools of liquid fuel [8]. There is wide debate over the controlling mechanisms that govern this particular region. The source of confusion is conflicting data that shows both the presence and absence of liquid convection ahead of the flame [8].

The uniform regime acts as a transition region between liquid-phase control and gas-phase control. It is most likely that the controlling mechanisms are a combination of both liquid and gas convection, since recirculation and induced convection exist in both the gas and the liquid ahead of the flame. However, the dominance of one over the other is dependent on the fuel temperature. Liquid-phase mechanisms are controlling at lower temperatures and gradually change to gas-phase mechanisms at higher temperatures near the flash point [10].

2.5.4 Super-Flash (Gas-phase) Regime

If the initial fuel temperature is at or above the flash point, then the flame will spread entirely by means of gas-phase mechanisms and liquid convection is no longer present ahead of the flame [7]. This temperature region is often referred to as the pre-mixed regime, because a flammable mixture exists everywhere above the surface of the fuel. The flame spreads continuously without ever having to pause and pre-heat the fuel.

This region is extremely sensitive to fuel temperature since the vapor pressure, and therefore the equivalence ratio, just above the fuel surface increases with temperature [7]. At the cooler end of this temperature regime, the fuel/air equivalence ratio is just inside the lean limit of the fuel. However, the equivalence ratio is stratified since the vapor pressure decreases with distance from the fuel surface. Therefore, not only must there be a flammable mixture, but it must also exist above the quenching distance of the fuel [7]. The quenching distance is the minimum distance that flame can exist above the fuel surface. When below the quenching distance the heat transfer from the flame to the fuel is too large and the flame can no longer sustain itself. However, the quenching distance for n-decane is extremely small, on the order of a few millimeters, and is much smaller for alcohols [25].

White et al. [23] produced extensive results on flame spread over hydrocarbon fuels, comparing JP-5 and JP-8 over a large temperature range of 10 – 90 °C. The flash point temperatures of JP-5 and JP 8 are 60 °C and 38 °C. It was found that the transition from liquid-phase to gas-phase controlled flame spread occurs at a flame spread rate of 12 m/s and reaches a maximum speed of 160 cm/s. These results are in excellent agreement with the predictions made by Feng et al. [26] as pointed out by White et al. [23].

$$V_f = \alpha V_L \sqrt{\frac{\rho_b}{\rho_u}} \quad (4)$$

Feng et al. used the above relation to predict flame spread velocities in the gas-phase controlled region, where ρ_b is the density of the products, ρ_u is the unburned gas density, α is a constant, and V_L is the fundamental laminar burning velocity of a pre-mixed flame.

A typical value for V_L is approximately 40 cm/s for pre-mixed stoichiometric flame spread over hydrocarbons. The density ratio, ρ_b / ρ_u , is ~ 7 . White et al. found $\alpha = 1.5$, based on the above equation and their experimental results for JP fuels. They predicted that the flame spread rate would be 12 cm/s using values obtained for laminar pre-mixed flame spread in the lean limit of flammability ($V_L \sim 3.5$ cm/s, $\rho_b / \rho_u \sim 5$). This is consistent with their measured value obtained at the transition region, where the equivalence ratio is just within the lean limit of the fuel.

2.5.5 Stoichiometric

The stoichiometric regime exists when the initial bulk temperature of the fuel is high enough to produce a vapor pressure necessary for a stoichiometric mixture [7]. The flame spread rate in this regime is at a maximum since stoichiometric implies ideal conditions for combustion. As the initial temperature increases, there is still a stoichiometric mixture, but its location increases in elevation. Therefore, stoichiometric flame spread is still present and the flame spread rate remains constant with initial fuel temperature.

During his experiments, Roberts [17] noticed that the maximum flame spread rates achieved for liquid fuels under stoichiometric conditions approached 200 cm/s. The stoichiometric spread rates are approximately 4 to 5 times faster than typical laminar burning velocities for pre-mixed flames [7, 23]. Roberts concluded that the excess speed is a result of un-reacted fuel vapor being accelerated by pressure build up behind the flame. Greater than laminar burning velocities are also achieved by flame curvature from the stratified vapor pressure that gives the flame front a larger surface area to burn [8].

The curvature also causes the flame surface to stretch thinner, causing an increase in the temperature gradient and resulting in a higher heat transfer rate.

Similar spread rates were found in mines, where the methane concentration near the ceiling was heavily stratified. A detailed discussion on this topic is provided by Glassman et al. [7] in regards to the work done by Feng et al. [26] on a uniform pre-mixed methane-air mixture.

2.6 Effects of Fuel Pan Dimensions

The dimensions of the tray in which the flame spread takes place have a strong influence on measured flame spread rates [12, 11, 23]. This is due to the restrictions that smaller trays place on liquid convection, on which flame spread is so highly dependent at lower temperatures. However, the effects of pan dimensions are also contributed to heat transfer to the pan. Mackineven et al. [11] did a comprehensive study on this subject. They took flame spread rate measurements for decane at 23 °C using a variety of different shaped fuel trays. The flash point temperature for decane is 46 °C. Along with pan dimensions, they also varied other laboratory parameters, such as pan material, fuel viscosity, and fuel temperature.

2.6.1 Pan Length

Mackinven et al. [11] found that the tray length has only moderate effects on the flame spread rate. The smallest length tested was 90 cm and corresponded to a spread rate of 2.8 cm/s. They observed the flame spread rate to increase with length until reaching a maximum velocity of 3.04 cm/s at a length of 180 cm. Their results showed

that the rate at which the spread rate decreases becomes large as the pan approaches 90 cm due to the shorter length impinging on the liquid convection ahead of the flame.

2.6.2 Pan Width

Burgoyne and Roberts [12] also performed experiments on the effects of pan dimensions. They determined the effects of channel width on flame spread rates for isopentanol by varying the temperature from 15 to 45 °C for 2.5, 3.3, and 6.3 cm wide pans. Their results showed that the flame spread rate decreases with width due to wall effects restricting the liquid convection, similar to the results obtained by Mackinven et al. for varying pan lengths. The flame spread rates for the three widths converge as the initial temperature approaches the flash point of isopentanol (41 °C). At this point, the controlling mechanisms are gas-phase and the width no longer has any influence on the flame spread.

Mackinven et al. [11] noticed similar trends and it was observed that increasing the pan width above 20 cm had little effect on the observed flame spread rate. This result could not be compared to the work done by Burgoyne and Roberts [12] since the largest pan width they tested was 6.3 cm. However, White et al. [23] reproduced their experiment with a 20 cm wide pan. The result was a relatively small slope that continued the trend of decreasing temperature independence with increased pan width. White et al. showed that the strong dependence on temperature observed by Akita [10] and Roberts and Burgoyne in the lower temperature region was a result of using relatively narrow fuel trays.

2.6.3 Fuel Depth

Burgoyne and Roberts [12] also studied the effects of liquid depth on flame spread rate by varying the temperature of isopentanol from 15 to 45 °C in a 3.3 cm wide pan and at depths of 0.2, 0.25, 0.3, 0.4 and 0.5 cm. The result was similar to varying the width and length of the tray. The spread rate increased with depth and the effects increased with decreasing temperature. The flame spread rate is more affected by the pan width at lower temperatures, because of the liquid-phase controlling, but becomes independent of changes in width at higher temperatures due to the transition to gas-phase mechanisms.

Mackinven et al. [11] performed similar experiments on decane at 23 °C in a 180 x 19.5 x 2.5 cm tray lined with glass. They also found the spread rate to decrease rapidly with temperature from about 6 cm/s at a depth of 20 mm to around 2 cm/s at a depth of about 2 mm. A propagating flame could not be stabilized at depths below 2 mm and was contributed to the inability of liquid currents to form at such shallow depths.

2.7 Flame Spread in Forced Airflow

Liquid flame spread in opposed and concurrent flow environments is a topic that has received very little interest. Most of the experimental work done on this subject has been for flame spread across solids, for obvious fire safety applications. However, there have been a few attempts to determine the behavior of flame spread across liquids when subjected to forced airflow [12, 13, 14]. However, it is important to note that the following results for liquid fuel flame spread are for laminar conditions, and that no literature has been found that present findings for turbulent airflow.

2.7.1 Effects on Flame Spread Rate

Burgoyne and Roberts [12] examined flame spread under forced airflow conditions as part of an effort to discover the effects of laboratory parameters on spread rates. They subjected flame spread across isopentanol and propanol at 15 °C to airflow speeds ranging from 0 to 200 cm/s for both opposed and concurrent flow. Their results are shown in the figure below.

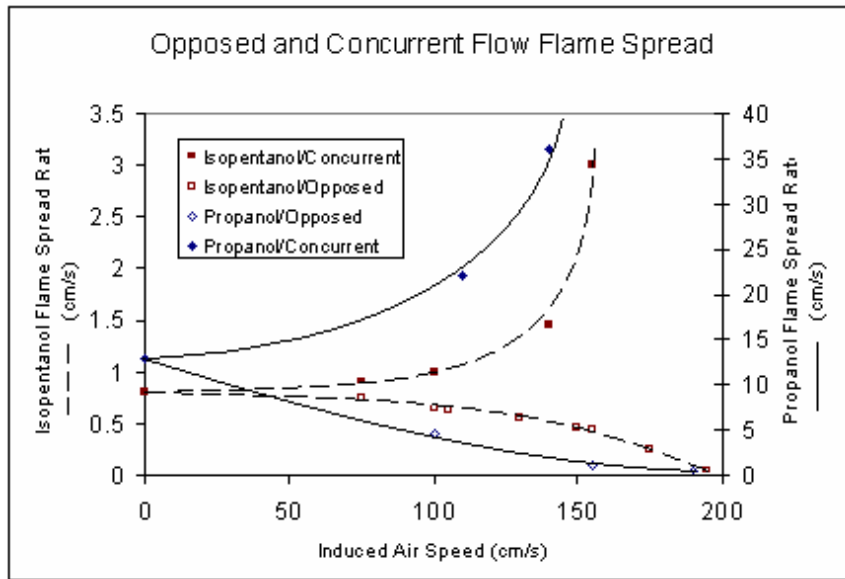


Figure 5. Flame spread rate measurements for isopentanol and pentanol at 15 °C [12].

Isopentanol, with a flash point of 41 °C, is clearly in the liquid-phase control region with a flame spread rate of only 0.8 cm/s at zero forced airflow [12]. That is why there is little change in the spread rate below an air speed of 100 cm/s for both opposed and concurrent airflow. For slow air speeds, buoyancy of the hot gases near the flame induces a flow that dominates the gas convection ahead of the flame [13]. The velocity of these induced air currents is large enough to suppress the effects of small forced air speeds. The flame spread rate for isopentanol in Figure 5 for opposed flow decreases very gradually, with an increasing rate of change as the opposed air speed approaches

200 cm/s, at which point the flame no longer spreads. However, the change in spread rate for concurrent airflow is extremely rapid, seeming to be almost vertically asymptotic, but this is because of the scale used by Roberts and Burgoyne [12] for the isopentanol.

Figure 5 shows that the propanol seems to be transitioning into the gas-phase region, with a flame spread rate of 14 cm/s with no forced airflow. This is why the propanol flame spread rate is affected by forced air flow at smaller velocities. Forced air currents will have more of an influence on flame spread rates when the controlling mechanisms are gas-phase. Unlike isopentanol, the change in spread rate for propanol is more rapid at low velocities and then decreases gradually to where, it too, ceases to spread at 200 cm/s opposed flow. The concurrent flow results for propanol are similar to that of isopentanol, in that the change in flame spread rate is very rapid at velocities higher than 100 cm/s. Also like isopentanol, the rate of change in the flame spread rate for propanol seems to continually increase with the concurrent air flow velocity. However, Suzuki and Hirano [14] later discovered that the rate of change would grow until the flame spread rate matches the concurrent flow velocity and then remain constant. The results obtained for propanol and isopentanol by Burgoyne and Roberts [12] show that there is a large difference on how forced convection affects flame spread depending on if it is below or above the flash point.

Suzuki and Hirano [14] studied the flame spread rates for methanol over a large range of forced air velocities ranging from 600 cm/s in the opposed direction to 600 cm/s in the concurrent direction. They also varied the fuel temperature, which gave an interesting view of the effects of forced airflow for different temperature regimes. These results can be seen in Figure 6 below.

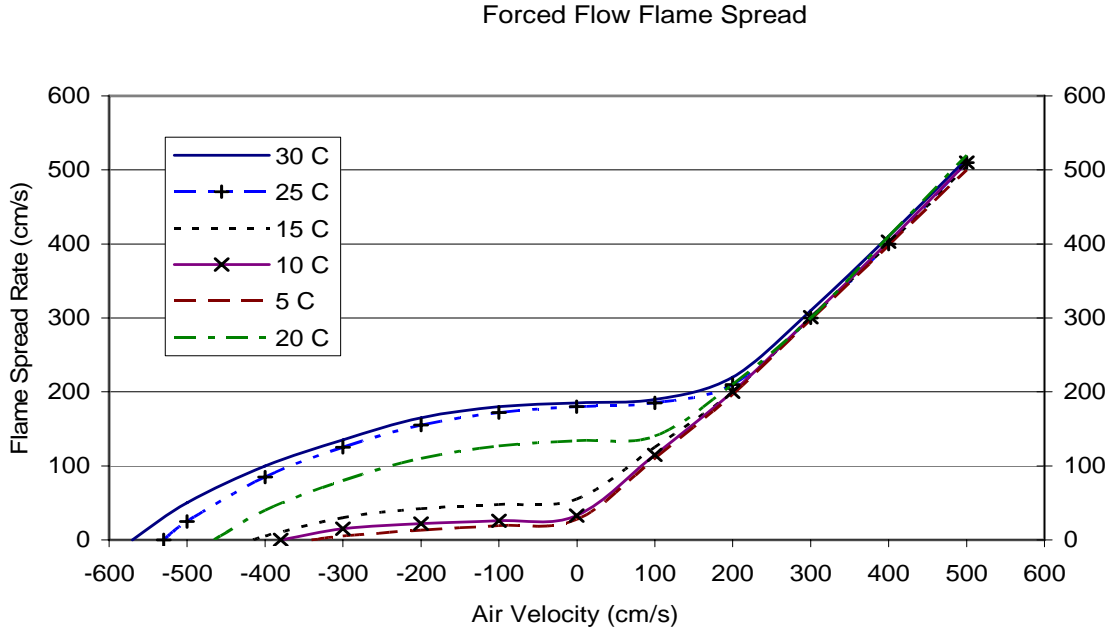


Figure 6. Opposed and concurrent flow flame spread over methanol at various temperatures [14].

The most noticeable aspect of the above results is the converging of all temperature regimes above a concurrent air velocity of 200 m/s, regardless of the initial temperature, implying that flame spread can be either gas or liquid-phase controlled. Hirano and Suzuki concluded that as the concurrent air velocity increases, it blows hot gas over the liquid ahead of the flame, causing the flame front to lean forward and drastically increase the rate of heat transfer to the liquid fuel ahead. Their measurements show that the flame spread in concurrent flow accelerates and matches the free stream velocity when the forced velocity grows larger than the flame spread rate for zero airflow. The flame spread rate increases, because it no longer has to wait for liquid-phase mechanisms to take effect and can continue to spread. Hirano and Suzuki were able to observe the shape of the flame front for different air stream velocities using high-speed schlieren photography.

Another result shown in Figure 6 is the minimal effect that low opposed air speeds have on flame spread rates. This coincides with the measurements obtained by Burgoyne and Roberts [12]. Similar to their results, the flame spread rates measured by Suzuki and Hirano [14] remain fairly constant until confronting an opposed air speed of about 100 cm/s. They mentioned that this is due to the deceleration of the air flow by the flame front. However, once the air speed is increased beyond that, the flame spread rate suffers a sudden decline. The decrease in flame speed is due to the opposed airflow reducing the residence time of the reactants, therefore, decreasing the Damköhler number [4]. The fuel vapor and oxygen are blown away before they can be combusted.

2.7.2 Effects on Flame Behavior

The work done by Burgoyne and Roberts [12] and Hirano and Suzuki [14] in regards to forced flow flame spread is insightful, however neither one mentioned any effects that forced air flow might have on pulsating behavior and liquid convection. It would be helpful to know the effects on these phenomena since they are the dominating features of flame spread across liquids below the flash point. Ross et al. [13] managed this for pools of 1-butanol subjected to very low-speed opposed and concurrent airflow. They found that such low opposed velocities have little effect on the spread rate and that the jump and crawl velocities remain the same, 1.5 and 10 cm/s. However, decreasing the opposed flow velocity does affect the flame spread pulsations, even as the air speed crosses over from opposed flow to concurrent flow. Ross et al. observed that at high concurrent air speeds, 20~30 cm/s, the flow dominates over buoyancy effects and the pulsations discontinue. Their results show that opposed airflow does not affect the liquid convection length. A liquid vortex forms beneath the surface for all opposed velocities

and extends to 2cm before the flame jumps and a new vortex forms. For concurrent flow, however, Ross et al. showed that liquid convection is influence by the forced convection. Their thermal measurements show a vortex for slow concurrent velocities but not for higher speeds. Heat transfer from the flame is large enough that liquid convection is no longer a controlling mechanism. Although liquid convection exists, it is not affected by the rapid fluctuations in flame spread rate [13].

2.7.3 Opposed Turbulent Flow

As far as it is known, there have been no experimental investigations into the influence of opposed turbulent flow on flame spread across liquids. However, there have been work done on solid fuels, and some of the results might be applicable to liquid fuels. Zhou et al. [27] studied the effects of opposed turbulent flow on flame spread over thick PMMA and thin filter paper sheets. They discovered that, for the PMMA, moderate turbulence levels increases the flame spread rate for all opposed air velocities tested (0.5 ~ 2.5 m/s). The flame spread rate reaches a peak at about 6% turbulence before decreasing with higher levels. These findings are concurrent with their temperature readings that show an increase in the surface temperature ahead of the flame front at 6% turbulence intensity. Zhou et al. proposed that the increase in flame spread rate is due to enhanced mixing of the reactants and an increase in conductive heat transfer to the solid fuel due to the flame (shown by interferometric photographs) being pushed closer to the fuel surface with increased levels of turbulence. However, these become dominated by other mechanisms that act to decrease the flame spread rate as the turbulence intensity is increased. These mechanisms, as mentioned by Zhou et al. are increased convective

cooling of the gas and the transportation of cooler air from the free stream to the surface by eddies.

It is difficult to say what parts of the results from the solid fuel testing done by Zhou et al. can be carried over to opposed turbulent flame spread for liquid fuels. Certainly the mentioned mechanisms such as increased convective cooling, increased conductive heat transfer and increased homogenization of the fuel mixture will also occur for liquid fuels. However, the effects of turbulence on liquid convection will have to be considered and will most likely dominate the other effects since it is the controlling mechanism for liquids below the flash point. And the effects of increased levels of turbulence will be purely in the gas-phase when dealing with flame spread above the flash point.

2.8 Turbulent Flow Separation Behind a 2-D Fence

The separation region behind the fence is an important aspect of the current research, because of the numerous effects that flow field conditions have on flame spread behavior as mentioned in the previous section. The separation region contains reverse flow that can influence the upstream spread of flames by aiding gas-phase and possibly liquid-phase mechanisms. These areas of recirculation might retain heat and fuel vapor to be used by the flame, instead of being blown away as would normally occur under large opposed flow velocities. The mixing of fuel and oxidant could be improved by the increased levels of turbulence, which might also decrease the flame spread rate by cooling the reaction with increased transportation of colder air from the free stream. In any case, it is apparent that turbulent shear flow is extremely complicated and it is

difficult to predict how it will affect flame spread rate measurements, which is the goal of this research.

The first step to understanding how a region of separated reverse flow might affect flame spread is to understand as much as possible about the region itself. Fortunately, there have been numerous studies on this topic done with both experimentation and simulation. Good and Joubert [19] provided valuable insight by placing a vertical fence with a tapered edge in turbulent airflow with a Reynolds number of 1.76×10^5 , based on the fence height and mean free stream velocity. Their fence height, h , was 4 inches and the tunnel height, H , was 36 inches, giving a blockage ratio, h/H , of 0.11. They took measurements at a few select locations using pitot static and yaw tubes. Good and Joubert [19] observed that the separation region extended as far as 13 fence heights down stream and contained reverse flow velocities as large as half the free stream velocity. The maximum forward velocities were found to be about half as much greater than the free stream velocity. They determined the height of the separation region to be the location where the stream function equaled zero and its maximum height was more than twice the fence height and occurred at about 5 to 7 fence heights downstream.

Durst and Rastogi [16] compared the results of Good and Joubert [19] to their calculations using the same setup and performing additional experiments using a range of blockage ratios from 0.0 to 0.5. Their calculations used the k- ϵ turbulence model with modifications to account for streamline curvature. They compared the results of these calculations to those done without the modifications and to experimental data. They produced results that were an improvement on the previous calculations when compared to the data obtained by Good and Joubert [19]. The calculations done by Durst and

Rastogi [16] predicted a recirculation length, L_r , of approximately 14 fence heights, and a max forward and reverse velocity of 1.19 and -0.86 times the free stream velocity. As can be seen from the previous paragraph, their predictions compare well with the data of Good and Joubert. However, their calculations under predicted and over predicted the maximum forward and reverse velocities, but it might have been the result of using intrusive measurement techniques at a select few locations.

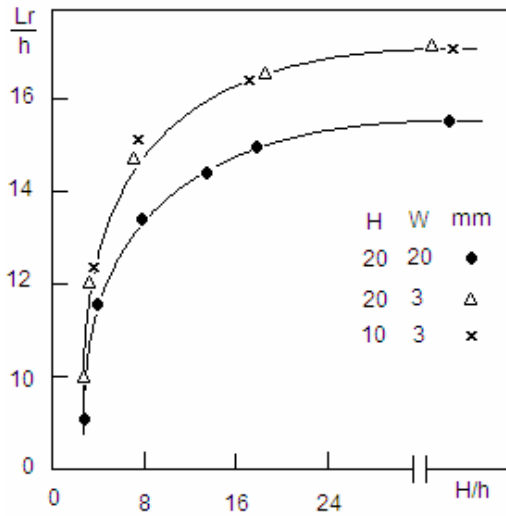


Figure 7. The recirculation length as a function of the blockage ratio for various fence aspect ratios [16].

Durst and Rastogi [16] also obtained experimental data in order to supplement existing data with large gaps in untested blockage ratios. Their experimental results are presented in non-dimensional form and one of their charts was recreated and shown in Figure 7. Their data shows that the length of the recirculation region is mostly independent of fence height for similar blockage ratios. However, the fence width does affect the recirculation length by decreasing it as the width is increased. It is also clear from Figure 7 that the length of the recirculation region is a strong function of the blockage ratio when the tunnel height is less than 16 times the fence height. But the

recirculation length levels off at about 17 fence heights when the tunnel height is increased.

Larousse et al. [28] studied obstructions with a 25 mm square cross section in turbulent channel flow with a Reynolds number of $Re = 10^5$. Data was taken on the separation region using a two-component laser Doppler anemometer (LDA). They used a blockage ratio of 0.5 and varied the length of the obstruction from being a cube to extending the entire width of the test section. The tunnel had a cross section of 600mm x 50 mm. Trip wires were fitted at the inlet of the tunnel and the obstructions were secured to the surface at 52 tunnel heights downstream. It was discovered that decreasing the length of the obstruction drastically reduces the length and height of the separation region. At large lengths, the flow behind the obstruction still maintained two-dimensional characteristics, but at smaller lengths multiple vortices developed that would intersect the separation region. These vortices originate from all sides of the obstruction and prevent the separation region from fully developing.

2.9 Particle Image Velocimetry

Particle Image Velocimetry (PIV) is a useful technique in obtaining instantaneous velocities of a flow field. An entire PIV system consists of lasers, seeding, cameras, synchronization, and processing. The lasers illuminate the plane of interest and allow the camera to record the positions of the seeding particles carried by the flow. The camera then transmits the images to the processor to be converted into velocity vectors. The velocity is found by dividing the distance the particles travel by a known time interval.

The laser is typically an Nd: Yag laser that fires a diverging beam into the flow. The laser creates a light sheet that illuminates the particles within a specific plane. The laser cannot run continuously and must pulsate due to the large amount of power required to illuminate micron size particles [29]. The result is a stroboscopic effect with a known and adjustable time between pulses. The user selects a time interval that is applicable to the type of flow being studied. The lasing cavity is Q-switched to provide short bursts of energy, usually on the order of a few nanoseconds [29]. This reduces the power requirement and provides better illumination of the particles. However, the minimum time interval available between light pulses is too large for many applications. Therefore, a second laser is provided so that the two lasers can alternate when acquiring data.

A CCD camera (Charged Couple Device) is placed perpendicular to the light sheet and detects the illuminated seeding particles. Two frames of particle images are required to provide the information necessary to perform velocity calculations. The CCD camera allows two successive images to be recorded on a double frame, thereby making it possible to record images with a small time interval. The CCD camera consists of a matrix of light-sensitive cells and storage cells [29]. When the laser emits the first pulse, the camera exposes the first frame and transfers it to the storage cells. The camera then exposes the second frame during the second pulse and transmits the two images to the processor. A synchronizing device sends signals to the laser and the camera so that the two are coordinated. Filters are installed on the cameras so that only light with a wavelength of that emitted by the laser will pass. The images appear as small specks of light scattered across a dark background, similar to stars in a night sky. A general representation of a PIV set up is shown in Figure 8 below.

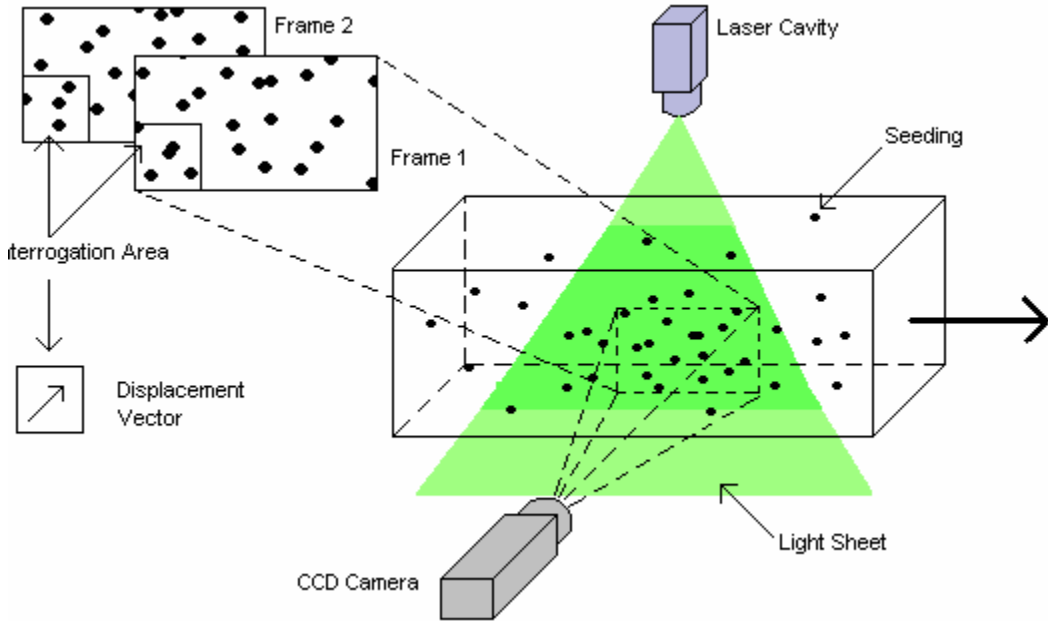


Figure 8. A typical PIV set up depicting the illumination and recording of particles to be correlated for each interrogation area.

The images are separated into square regions called interrogation areas. The interrogation areas from both frames are correlated using Fast Fourier Transformation (FFT) techniques [29]. An average displacement vector is produced and is representative of all the particles within the interrogation region. The displacement vector is divided by the pulse time interval to obtain a velocity vector. Particles often exit the interrogation area during the time interval between pulses and can reduce accuracy. This problem is referred to as “in-plane dropout” [29]. A modified correlation technique, called adaptive correlation, is often used to counteract in-plane drop out by using an iterative procedure with an initial-guessed offset value. This process is longer than traditional cross-correlation techniques but it increases signal strength and allows the user to refine the interrogation area while retaining the same number of acceptable vectors and without increasing seeding density.

Chapter 3. Experimental Setup

3.1 Wind Tunnel

A schematic drawing of the wind tunnel used to simulate a 2-dimensional engine nacelle is shown in Figure 9. The inside dimensions of the test section were 182.9 cm wide by 22.9 cm tall and 243.8 cm long. A fuel pan that was 27.9 cm wide and 39.4 cm long, with the length running parallel to the flow was placed inside the tunnel. The pan was installed so that the edges were flush with the bottom of the test section. The pan width was made to be greater than the 20 cm required to stem the influential wall effects created by small widths.

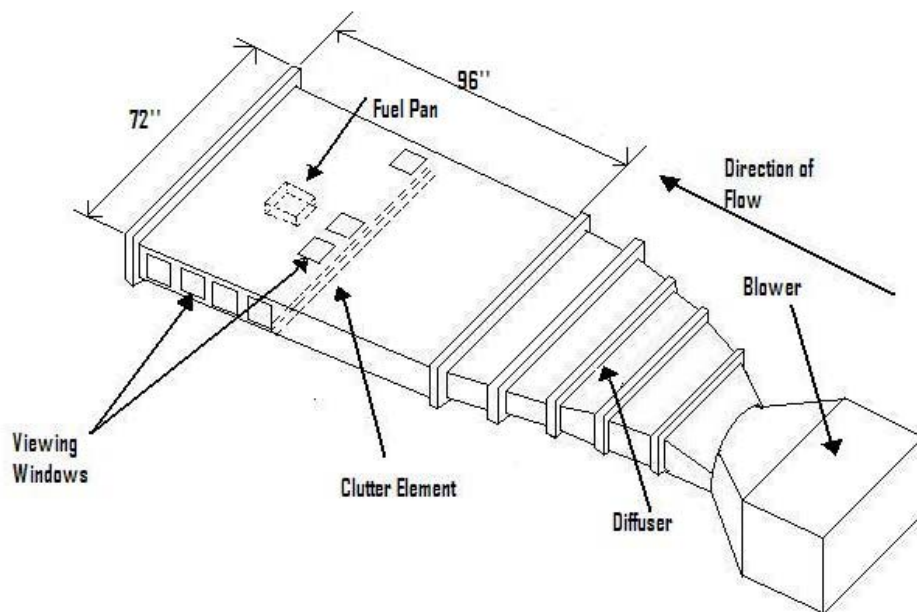


Figure 9. A diagram of the wind tunnel used in present research.

The depth of the pan was 3.81 cm. However, the pan was not filled to the edge, so as to prevent spill over. The depth of the liquid was 3.18 cm at the upstream end and

2.54 cm at the downstream end due to a slight incline in the tunnel. This should have little impact on flame spread rate measurements since the incline is relatively small ($< 1^\circ$) and because Mackinven et al. showed the flame spread rate is not significantly affected by changes in fuel depth above 2.5 cm. The inside of the fuel pan, along with a clutter element can be seen in Figure 10. The clutter element is the original size and is in the original location. The bottom of the fuel pan can be seen in Figure 11.



Figure 10. Photograph of the inside of the wind tunnel showing the fuel pan, clutter element, and viewing windows.



Figure 11. Photograph showing the underside of the fuel pan.

Observation windows were installed in the ceiling and in the right side of the test section when looking upstream. The windows were 20.32 cm wide and 16.51 cm tall and were made from either Robax tempered glass, ceramic, or quartz glass. The quartz was used when taking PIV measurements because of its superior optical qualities.

The tunnel was an open loop facility with a 6000 scfm centrifugal blower providing the opposed air flow conditions. A turbulence grid ran along the entire height and width of the junction between the diffuser and the test section. The width of the grid bars is 1.91 cm and 0.32 cm thick and made from mild steel. The spacing in between the bars is 3.81 cm, with exception to the sides, whose spacing can be seen below in Figure 12.

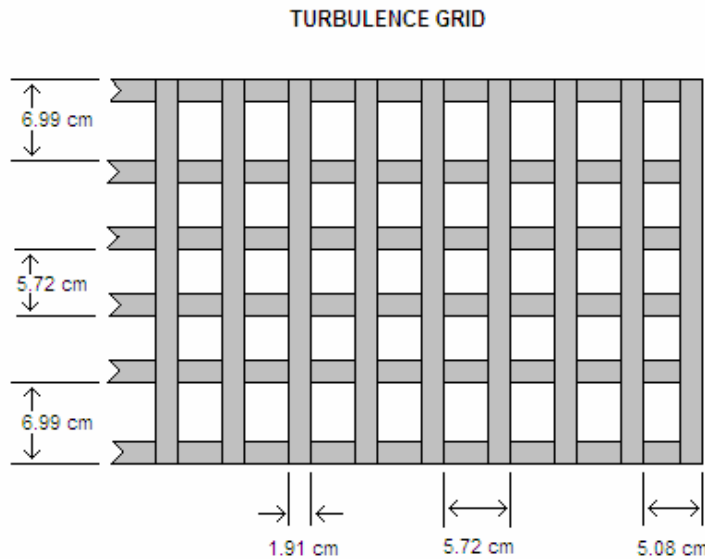


Figure 12. Grid spacing for the turbulence grid.

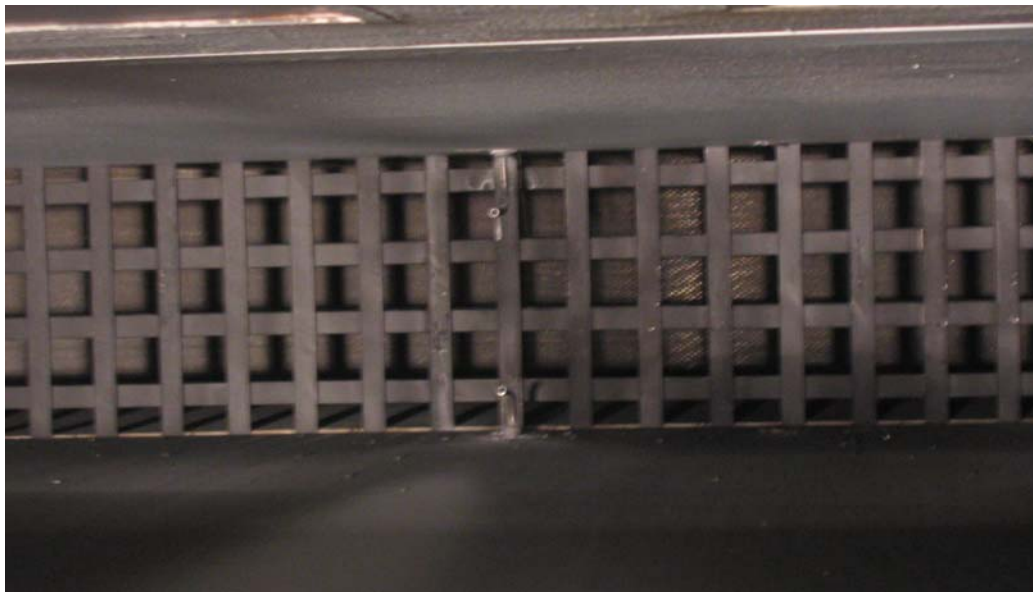


Figure 13. Photograph of the turbulence grid.

3.2 Clutter Elements

A variety of different clutter shapes and sizes were used to simulate the different kinds of clutter you might find in a generic engine nacelle. All the clutter elements were based off of the one used by Disimile and Davis. They used a 0.6 cm thick piece of angle

iron with 5.1 cm sides and a length such that the ends were flush with the sides of the tunnel. The clutter element was oriented so that the inside of the angle faced upstream and was placed 22.2 cm upstream from the edge of the fuel pan. This clutter element and its orientation are referred to as the original setup and provide a base line for the results. Also, the clutter element is sometimes referred to as the fence.

Four different configurations of clutter elements were chosen for the current research. Each configuration included three variations in the parameter that made it different from the original clutter. In some cases, the dimensions of the original clutter were used as one of the variations. Holes were placed with a diameter $D = 1.27$ cm at a distance d and centered along the entire length of the fence. The other parameters that were varied were the length, L , the height, h , and the distance to the fuel pan, X_p . A diagram depicting the dimensions of the clutter elements is shown below in Figure 14, and below that is table 10, which shows each of the fences tested and their dimensions. The level of perforation is also shown and is given in terms of a percentage. The percentage, P , represents the total area of the holes compared to the area of the fence facing the direction of the flow and is given by the following equation, where N_H is the number of holes.

$$P = \frac{N_H \pi D^2}{4hL} \times 100 \quad (5)$$

As can be seen in Table 1, only one dimension is changed for each fence, while the other dimensions maintain the parameters of the original clutter element. Below Table 1 is Table 2, which shows the test matrix used where each box represents a run and lists the variable dimension that was tested. There are 16 boxes, but only 12 runs were

made since several of the dimensions could be tested using the single piece of original clutter.

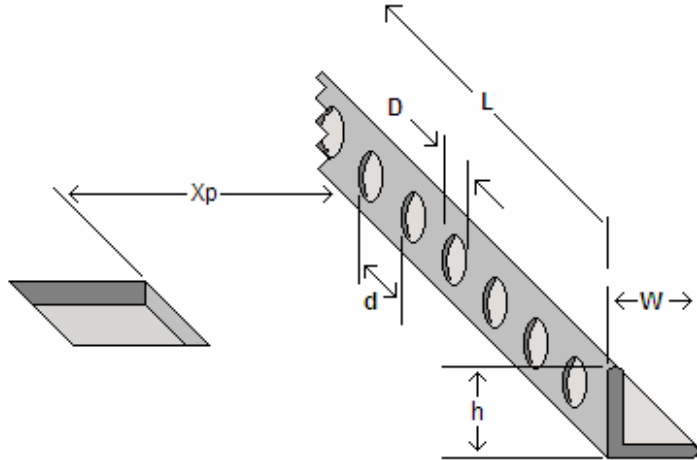


Figure 14. Diagram showing the fence parameters varied.

Table 1. Fence dimensions.

Fence #	h (cm)	L (cm)	d (cm)	P (%)
1	5.08	182.9	0	0
2	7.62	182.9	0	0
3	2.54	182.9	0	0
4	5.08	15.2	0	0
5	5.08	30.5	0	0
6	5.08	61.0	0	0
7	5.08	182.9	12.7	7.6
8	5.08	182.9	7.6	12.5
9	5.08	182.9	5.1	19.1

Table 2. Test matrix.

Clutter Variable	Variable Dimensions (cm)			
Distance to Fuel Pan (X_p)	22.2*	17.1	11.4	5.7
Height (h) [#]	7.62	5.08*	2.54	NA
Length (L)	182.9*	61.0	30.5	15.2
Number of 1" Holes (N_H)	35	23	14	0*

*Dimensions of original clutter, taken in a single run

[#]The height, h , and The width, W , are equal for all clutter elements

Disimile and Davis [6] characterized the flow field in the same wind tunnel using constant temperature anemometry (CTA). It was found that the mean velocity in the direction of the flow was 6.30 m/s with a margin of 10%. The turbulence intensity was measured to be 5.0% with a margin of 10%.

3.3 PIV

3.3.1 PIV Equipment

A New Wave Research Solo 120 Nd:Yag laser was used to provide the illumination for taking PIV measurements and is shown in Figure 15. The laser was hooked up to a power unit, which controlled the power output of the laser and cooled it using distilled water. The unit has two lasers that are housed side by side within the same unit and make use of optical components to combine the beams. The peak energy of the laser is 120 mJ and fires a laser with a wave length of 532 nm when operating at 15 Hz. This particular model had no power attenuator and only operated at two power settings, high and low.

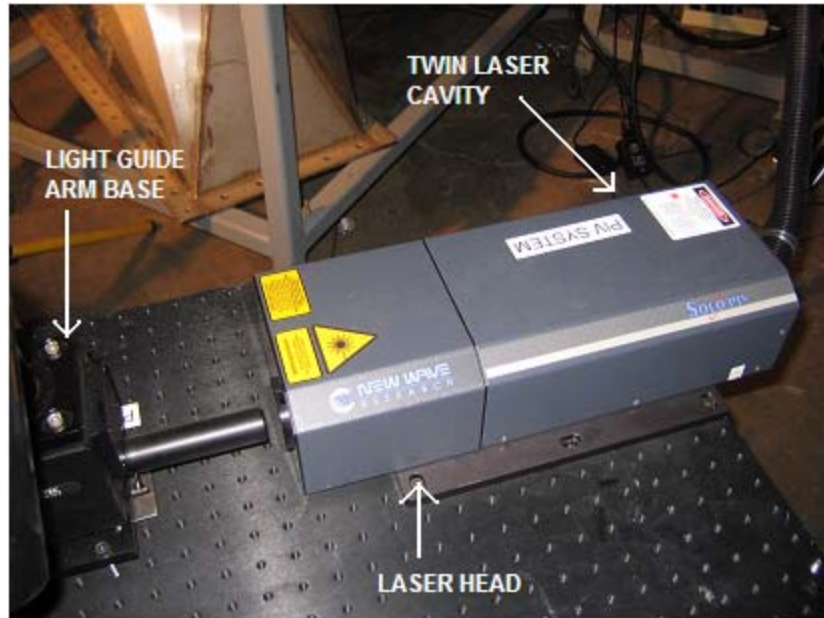


Figure 15. Photograph of laser system used for PIV illumination.

The path of the beam was directed using a light guide that was provided by Dantec Dynamics and consisted of a base mount, flexible arm, and an optical head. The beam enters the light guide through the base mount and travels through the flexible arm that has flexible rotating joints to allow the user to point the beam in any direction and orientation. Mirrors located at each joint relay the beam and prevent it from being interrupted. The optical head converts the beam into a light sheet. The thickness of the sheet can be adjusted using a knob located on the side of the head. The optical head and light guide are shown in Figure 16.

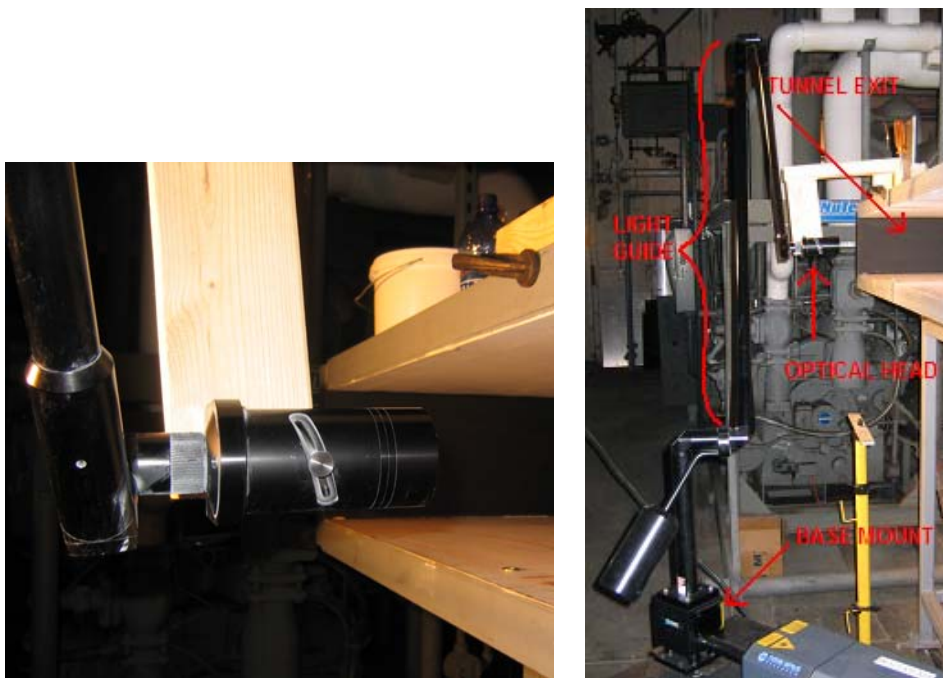


Figure 16. Photographs of the optical head (left) and the entire light guide (right), including the base mount, extension arm and optical head.

A Redlake Mega Plus 4.0/E 12 bit CCD camera was used for taking images and is shown below as Figure 17. The resolution of the camera is 2048 x 2048 pixels and was placed atop a tripod. A 532 nm filter was installed on the camera to filter out any light other than that coming from the illuminated particles. A 105 mm Nikon lens was used with the camera.



Figure 17. Redlake Megaplus CCD camera used for taking particle images.

3.3.2 PIV Setup

Seeding was accomplished by using micron size aluminum oxide particles. The seed was placed inside a cyclone seeder shown in Figure 18 and compressed air at 30 psi was used to mix the seed and inject it into the air stream. The seed was injected at the top and bottom of the test section, just in front of the turbulence grid and along the centerline of the tunnel. The 6.4 mm diameter steel pipes used to insert the seeding can be seen in Figure 13 directly downstream of the turbulence grid. They are bent at right angles so that the seed enters the tunnel in the same direction as the flow.

The optical head was attached to the tunnel outlet and oriented so that the laser sheet lied along the centerline of the tunnel. The very tip of the optical head lied 15.24 cm downstream of the tunnel exit. The camera was aimed through the side windows and perpendicular to the light sheet. The camera was then focused onto the same plane as the light sheet. Due to the small size of the particles, and decreased intensity of the second pulse, the laser had to be used at high power and the camera set to the lowest f-stop

setting to detect the small particles. A diagram and picture of the setup can be seen in Figure 19 and Figure 20.



Figure 18. Photograph of cyclone seeder used for injecting aluminum oxide particles into air stream.

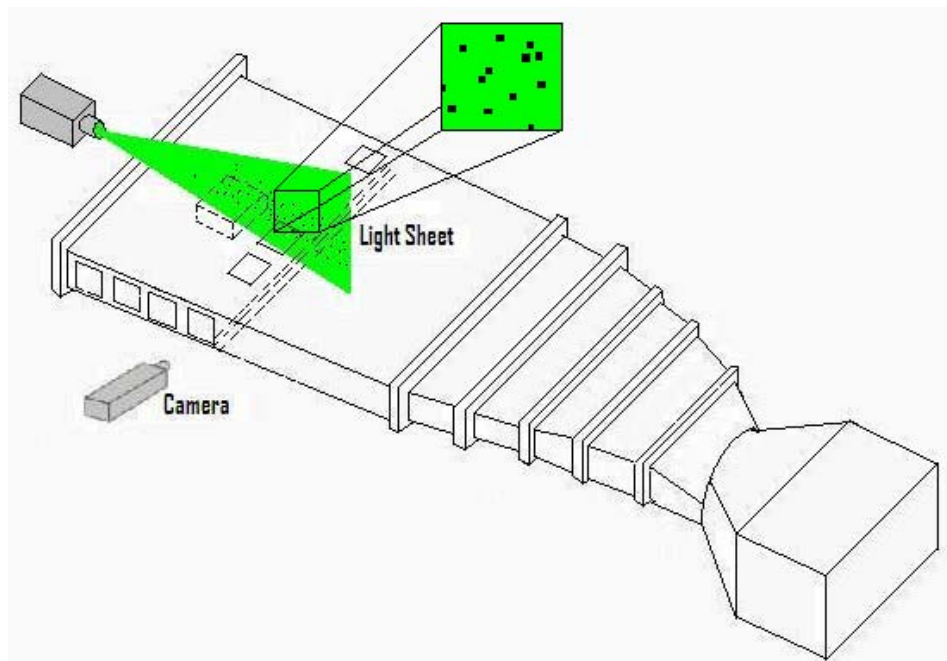


Figure 19. Diagram depicting the PIV setup used for the present research.

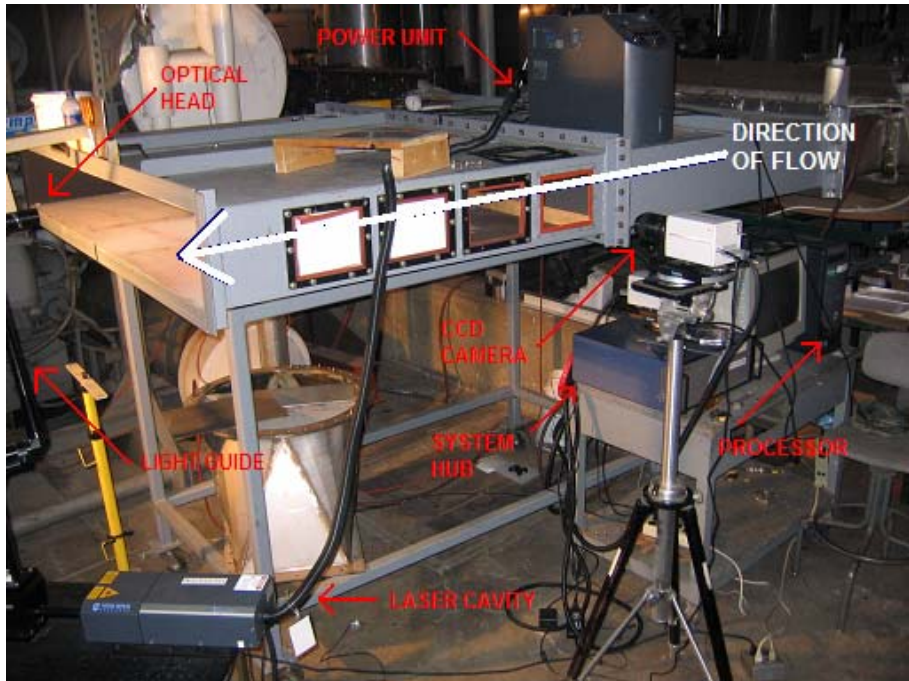


Figure 20. Photograph showing the entire set up for PIV.

The laser head was originally placed on top of the test section and fired down through the windows on top. However, a sufficient angle for taking images over the fuel pan was not obtainable and the laser had to be moved to the rear of the tunnel. During the move the laser became misaligned such that the second pulse coming from the second laser cavity could no longer be seen exiting the laser head. The head cover had to be removed and the beam combiner adjusted until the beams from the two lasers combined. Despite repeated attempts to adjust the beam combiner, a slight shaking persisted in the light sheet. The shaking was due to the beams from the two laser striking slightly different locations. The degree of shaking increased the further the beam was from the optical head. The optical head was moved to 7.62 cm downstream of the fuel pan to determine effects of shaking on the measurements. No difference in the results could be observed and it was, therefore, determined that the slight divergence of the two laser sheets had little or no effect on the measurements.

The camera was synchronized with the light sheet pulsations using a Dantec Dynamics System Hub. The duration of each pulse was $0.01\text{ }\mu\text{s}$ and the time interval between pulsations was set at $100\text{ }\mu\text{s}$. Each recording consisted of two light pulses, one for each frame. The time between recordings was 250 ms. The Hub used a 100 Mbit Ethernet adapter to transmit the images to a Pentium computer for processing.

The size of the images were 178×178 mm and were taken over the pan and behind the fence. The first location was taken through the second window downstream of the fence and covered from 15 mm upstream of the pan to 178 mm downstream. The height of the image started at 10 mm below the bottom surface of the test section and extended upward 178 mm. The second location was taken through the closest window to the fence and covered from 12 mm upstream of the fence to 178 mm downstream. The height included from 7 mm below the bottom surface of the tunnel to 178 mm upward. Unfortunately, the gap in between the two windows creates a blind spot of 53 mm that can be seen in the below diagram showing the locations where the images where taken. The location and size of the images must be taken into account when considering the spatial resolution and range of velocity measurements desired. If a particularly large region is being investigated, then the scaling factor will be correspondingly large (the size of one pixel). An increase in image size means an increase in the smallest unit of velocity discernable by the system. However, a larger image will enable larger velocities to be recorded by reducing the risk of particles exiting the interrogation areas between pulses. The details of these problems and the methods for dealing with them are discussed in the following section on PIV error.

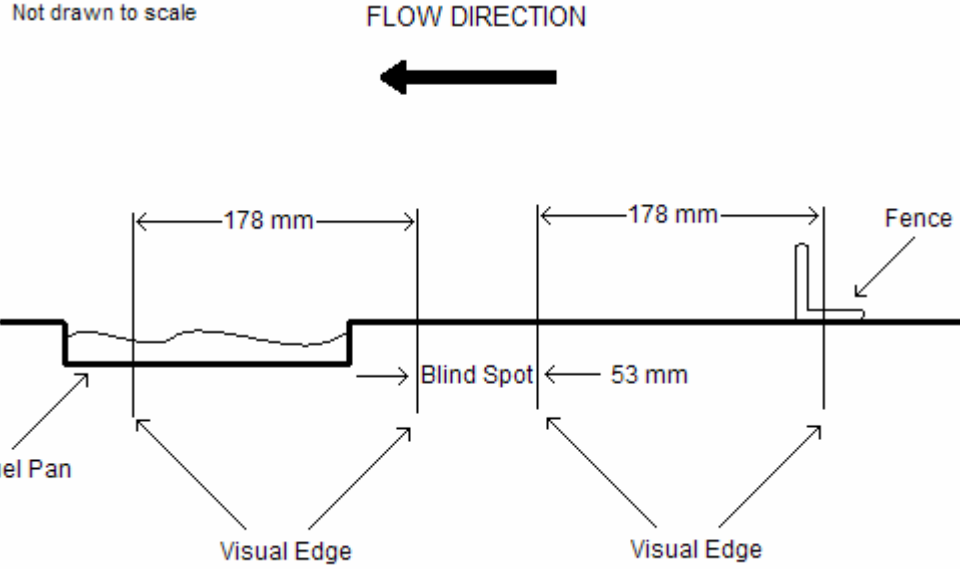


Figure 21. Diagram depicting the streamwise range of the PIV images and the blind spot due to the distance between observation windows.

3.3.3 PIV Error

The error associated with PIV is complicated and is a factor of many variables, including camera specifications, illumination wavelength, seed diameter, and experimental set up. However, the error can be divided into two categories, velocity dynamic range and sub-pixel resolution. The information provided below on these two topics is taken from the Dantec Dynamics FlowManager software guide and can be obtained by going to their website or contacting them by phone [29].

The dynamic range is dependent on the size of the interrogation area and the time in between frames. If the distance traveled by a single particle is greater than the interrogation area, then clearly its velocity is undetectable. Therefore, the maximum velocity is the size of the side of the interrogation area divided by the time in between images. However, the maximum displacement must be even less than that to reduce the affects of zero-velocity biasing. Zero-velocity biasing is the tendency of the average

velocity to lean towards the slower particles, because the faster particles have a higher probability of escaping the interrogation region. This problem is commonly referred to as in-plane dropout, and is the leading cause behind reduction in dynamic range.

In order to reduce in-plane dropout, it is generally recommended to select a time interval and interrogation size such that the maximum displacement is $\frac{1}{4}$ the length of the interrogation area. It is also advised that there be at least 5 particles per interrogation region. All of these factors lead to the conclusion that a larger interrogation region is a better choice. However, it is important to maintain less than 5 to 10% velocity variation to minimize zero-velocity biasing. Therefore, a smaller interrogation area will improve the signal-to-noise ratio. It immediately becomes clear that a trade off exists between obtaining a large velocity dynamic range and good spatial resolution.

Spatial resolution is dependent on the ability of the FlowMap processor to perform sub-pixel resolution. Without sub-pixel resolution, the minimum detectable velocity would simply be the size of one pixel divided by the time interval. The Fast Fourier Transform (FFT) process is not a continuous function and results in a discrete number of points. The number of points is the number of pixels on one side of the interrogation area. Therefore, each pixel correlates to only one velocity “bin” and only the velocity corresponding to each bin is observed. Fortunately, the theoretical FFT curve of the correlation plane can be interpolated to increase the number of velocity bins.

At least 3 data points are needed in order to perform a proper interpolation. This implies that the particle image should be at least 3 pixels in size. If a particle is only one pixel in size or smaller, then it would be impossible to determine the location of the particle within the pixel. If the particle is 2 pixels in size, then a curve-fit could still be

calculated. However, if the particle fell directly in between two pixels, then the interpolation would be vulnerable to noise and the result would most likely lean towards an integer value. The Dantec Dynamics FlowManager guide states that the processor is capable of 1/64 sub-pixel resolution, but suggests that a resolution of 1/10 pixels is more accurate when taking into account the camera and seeding considerations.

Considering the above, the current research into turbulent shear flow presents a challenge in obtaining accurate PIV results. The significant variation in velocity behind the fence required a large velocity dynamic range and good resolution was needed to observe the velocity structures in the separation region. Combined with micron size seeding particles and a small time interval for proper dynamic range, the above requirements made for a difficult compromise. An interrogation area of 64 x 64 pixels and a time interval of 100 μ s were chosen. A pixel spacing of 7.4 μ m and a scaling factor of 11.5, together with a maximum velocity of approximately 10 m/s gave a maximum displacement of 1 mm, or 11.5 pixels. This corresponded to about 20% of the interrogation length, well under the recommended maximum of 25%. Therefore, zero-velocity biasing was kept to a minimum and was further reduced by the use of adaptive correlation involving iterative interrogation areas. However, this resulted in a larger than desired minimum velocity of 0.087 m/s or 87 mm/s, using the 1/10 sub-pixel resolution. Therefore, the processor should only be able to discern a difference in velocity of 87 mm/s. Smaller velocities than this were recorded, indicating either the presence of noise or a better than 1/10 sub-pixel resolution. The resolution of 87 mm/s gives an error of approximately 1 to 2%, which is generally acceptable for engineering applications. The error due to resolution is also much smaller than the statistical error.

3.3.4 Statistical Error

The error associated with the given results stems from two sources, statistical error due to deviation in measurements and error due to the accuracy of the equipment and its operation.

The statistical error in this case is significant because of the large variations in velocity measurements due to turbulence and flow separation. The error was also effected by the use of a relatively small sampling size that was used to minimize processing time. The sampling size was large enough to obtain useful results, but a larger number of data points would have helped reduce statistical error, which was found using the formula below for 95% confidence [30].

$$\bar{U}_{error} = \bar{U} \pm \frac{1.96\sigma}{\sqrt{n}} \quad (6)$$

Where σ is the standard deviation and n is the number of samples. The error in finding the turbulence intensity is found by using the following relation.

$$Urms_{error} = Urms \pm \frac{1.96\sigma}{\sqrt{2n}} \quad (7)$$

3.4 Preliminary Flame Spread Tests

Flame spread tests were conducted by filling the fuel pan with approximately 32 mm, or 3.3 liters, of ethanol ($T_{flash} = 13^{\circ}\text{C}$). The fuel was then ignited at the downstream

edge of the fuel pan and the resulting flame spread was filmed using a 30 fps CCD camera. This was done once for each of the variations in clutter, including one run with no clutter. The flame spread rate was found by placing a white line every 38 mm perpendicular to the direction of flame spread and then visually inspecting the location of the flame relative to these markings. The distance traveled during each frame was multiplied by the frame rate of the camera to obtain the flame spread rate. Because the smallest discernible distance traveled by the flame is the distance between the markings, the error is +/- 19 mm. This results in a +/- 57 cm/s error in the determined flame spread rate. This is a considerable error that is not entirely conservative since the lighting, angle effects, and flame size make the location of the flame front difficult to determine. However, these are preliminary tests and were conducted simply to provide a better sense of the flame spread reaction to various clutter configurations and to give insight into where to go from here for future, more in depth, flame spread analysis.

Chapter 4. Results and Analysis

The raw data was obtained in the form of vector fields. Each vector representing an interrogation area (in this case 64 x 64 pixels) and displaying the average direction, velocity magnitude, and 2-D velocity components, U and V, for the particles in that area. Although the data is displayed as a vector field, it is also stored as a numeric table that allows the use of calculations to be applied to the raw data. The results of these calculations are presented below in the form of contour plots of vorticity, turbulence intensity, and Reynolds stress. Non-dimensional profiles of velocity, integral length scale and turbulence are also presented in an effort to collapse the results and forgo the further testing of various clutter shapes and sizes. Data was collected in the region behind the fence and over the fuel pan. However, only the results for the fuel pan are presented here since it is the effects on flame spread that are of concern. A picture of the location used for data acquisition is shown below. The edge of the fuel pan can be seen near the 9" mark on the tape measure.

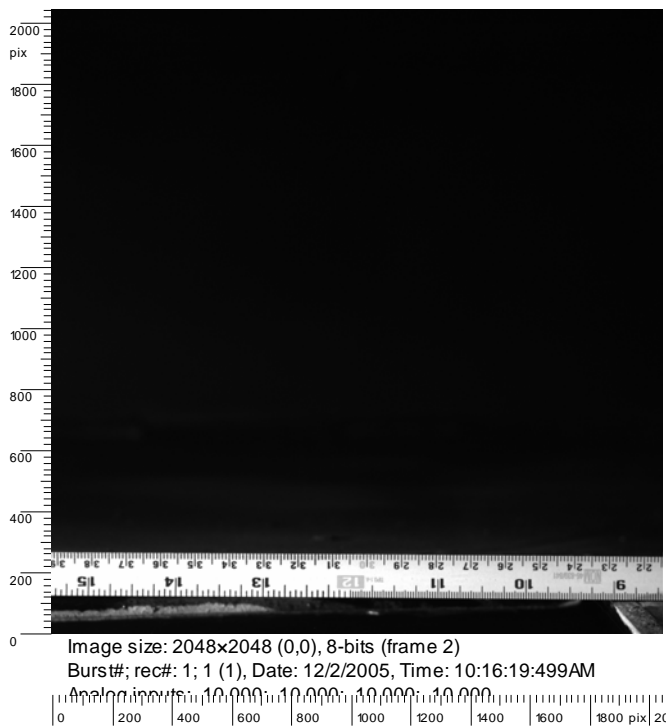


Figure 22. Picture of data acquisition location above the fuel pan. Tape measure extends to the edge of the original clutter location. The edge of the pan can be seen at approximately the 9 in mark.

Matlab was used for all analysis purposes except for vorticity, which was analyzed using a function built into the Dantec Dynamics Flowmanager software. Results are compared for each type of analysis to the original fence, which has the following dimensions. Fence distance of $x_p = 222$ mm, fence height of $h = 50.8$ mm, fence length of $L = 182.9$ cm (width of tunnel), and fence perforation of 0% or $D = 0$. It is important to note the dimensions of the original fence since it is used as a baseline for all the other fences. For specifics, please see the chapter on experimental setup.

4.1 Vorticity

4.1.1 Vorticity Contours

Vorticity contour plots were created using the vorticity data analysis option in the Flow Manager software. The vorticity is calculated by taking the curl of the velocity.

$$\text{curl } \vec{u} = \left(\frac{\partial u_z}{\partial y} - \frac{\partial u_y}{\partial z} \right) \vec{i} + \left(\frac{\partial u_x}{\partial z} - \frac{\partial u_z}{\partial x} \right) \vec{j} + \left(\frac{\partial u_y}{\partial x} - \frac{\partial u_x}{\partial y} \right) \vec{k} \quad (8)$$

However, since the velocity vector is only two-dimensional, the curl only gives the vorticity component perpendicular to the plane of interest and is represented by its scalar value, S . The differentiation is approximated by taking the difference of neighboring vectors and dividing by the grid distance.

$$S(m, n) = \frac{u_y(m+1, n) - u_y(m-1, n)}{\Delta x} - \frac{u_x(m, n+1) - u_x(m, n-1)}{\Delta y} \quad (9)$$

The result is a filled in contour plot that gives the z-component of vorticity for a two-dimensional velocity field and has the units of inverse seconds.

The scale is set from -300 to 450 for each plot, with the violet spectrum at the lower end. The flow direction is from right to left. Each plot begins at the edge of the fuel pan located at where $x/h = 0$. The distance along and above the fuel pan is measured in fence heights.

The first set of plots is shown in Figure 23 below and displays the vorticity for the 2-D flow field for the three blockage ratios tested, $h/H = 1/9, 2/9, 3/9$. It is obvious from inspection that the blockage ratio directly affects the vorticity magnitude. Not only does the vorticity greatly increase with blockage ratio, but there is a significant increase in

negative vorticity as well. However, the non-dimensional location of the vorticity remains relatively unaffected, including the location of negative vorticity, although scarce for the smallest blockage ratio.

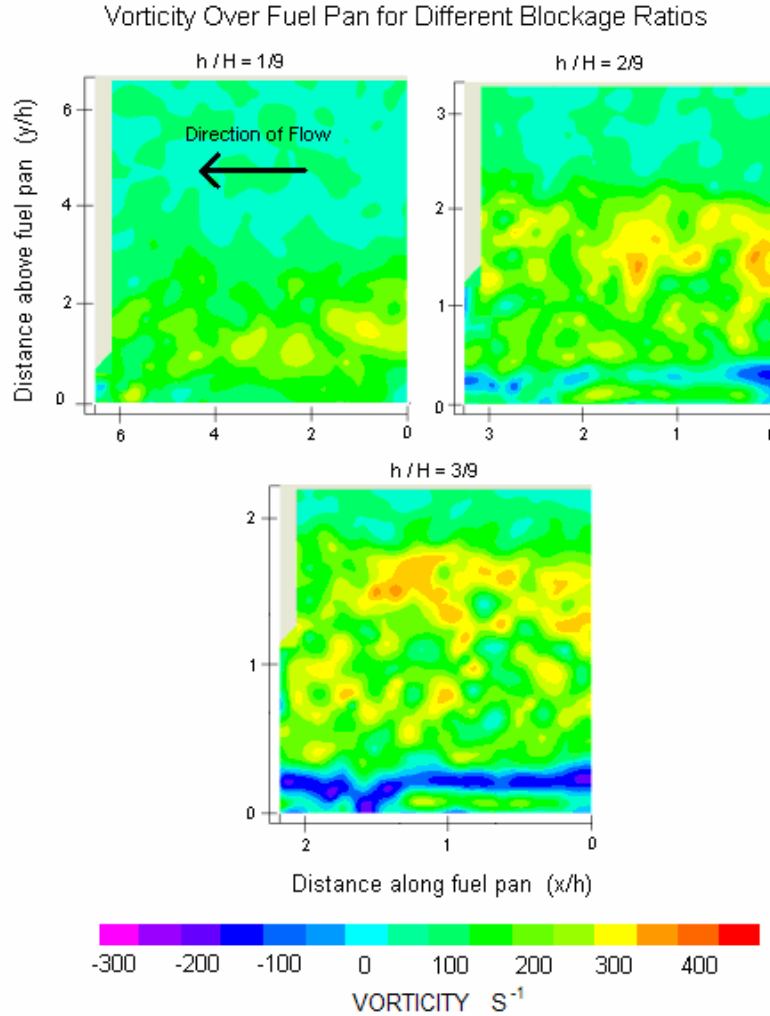


Figure 23. Vorticity plots over the fuel pan for the three blockage ratios tested. Values are time averaged over 20 samples.

The vorticity contour plots displayed below in Figure 24 show the time averaged vorticity over the fuel pan for three different distances to the fuel pan, x_p , levels of perforation, P , and fence lengths, L . The results for the different perforation levels and

fence lengths show that there is relatively little change in vorticity with variation in these parameters. There is a slight change from a length of $L/h = 12$ to $L/h = 6$, which is most likely due to the transition from 2-D to 3-D flow with vortex interactions. The increase in 3-D flow leaves less to contribute to the 2-D vortex generation shown in Figure 24.

Vorticity Over Fuel Pan for Various Clutter Elements at $h/H = 2/9$

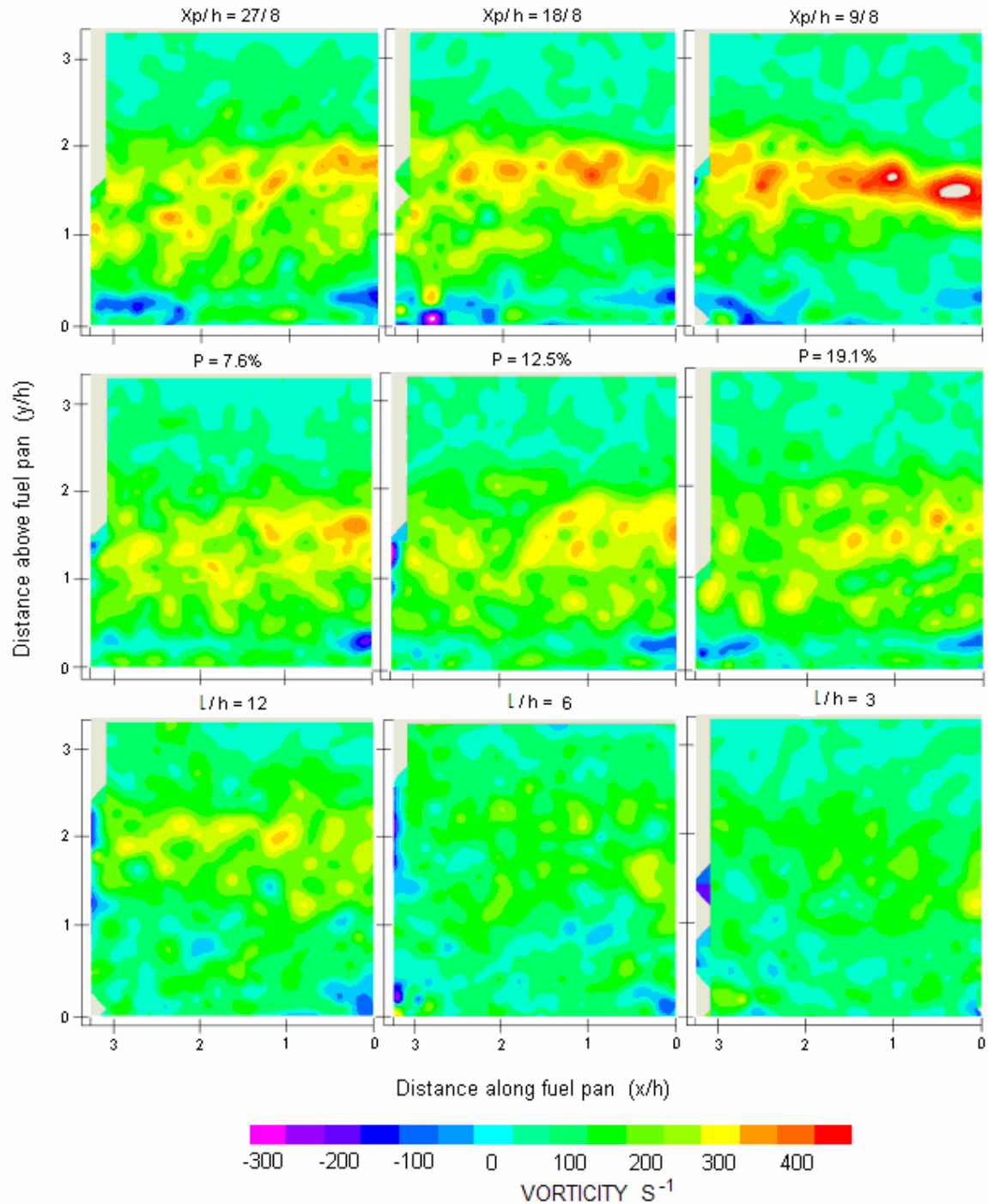


Figure 24. Vorticity plots over the fuel pan for the three fence distances, lengths and perforation levels tested. Values are time averaged over 20 samples.

4.1.2 Vorticity Profile Comparisons

Vorticity profiles for different fence heights and levels of perforation at different downstream locations were created to obtain a better understanding of the affects of fence dimensions on vortex generation. These profiles are shown in Figure 25. The profiles were plotted using non-dimensional parameters in an attempt to collapse the results. The resulting profiles are similar for different blockage ratios at locations close to the fence, but tend to diverge farther downstream. However, the profiles for perforation levels in Figure 26 are similar to the contour plots in that there is little change in vorticity with increased perforation. The vorticity was time averaged using 20 instantaneous vector fields that were filtered. The filtering process replaces questionable vectors with interpolated values to smooth the profiles out slightly for better comparisons.

It should be noted that the even spacing of the holes along each fence resulted in a hole being directly along the center line of the pan, and therefore in the 2-D laser sheet, for only the two largest perforation levels. As a result, the vorticity profiles for 12.5% and 19.1% perforation line up together, but differ from the 7.6 % and 0% profiles near the surface of the tunnel for the closest location to the fence reported in Figure 26. A similar pattern can be seen in the velocity profiles presented further down in Figure 38, where there is a strong forward velocity near the surface directly downstream of the fence. However, the effects on vorticity and velocity seem to be insignificant everywhere else since all four profiles closely overlap higher above the surface and for all elevations further downstream.

Vorticity Profiles for Different Blockage Ratios

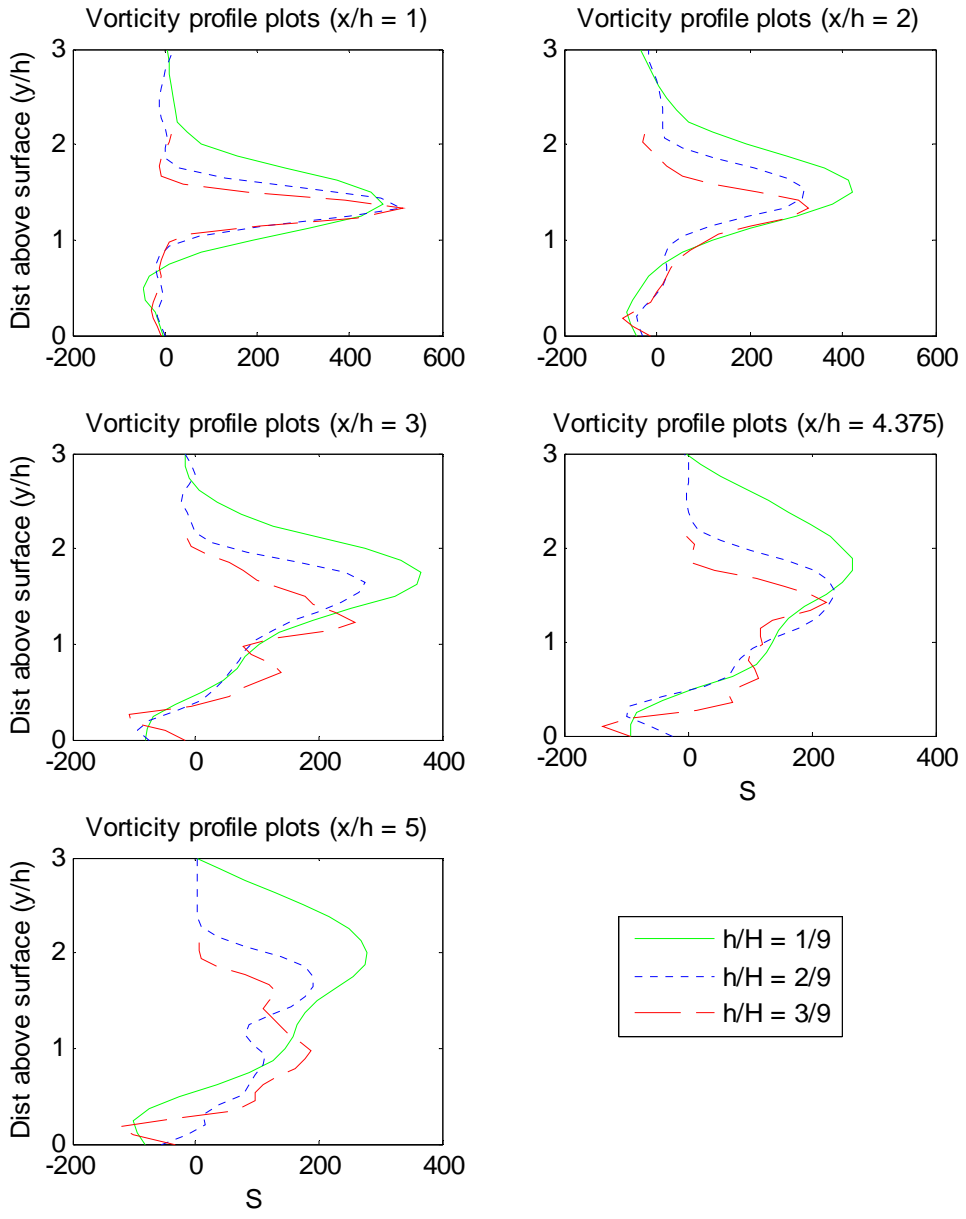


Figure 25. Vorticity profiles for the blockage ratios tested at five different locations downstream of fence. The downstream distance divided by fence height of $x/h = 4.375$ refers to the front edge of the fuel pan.

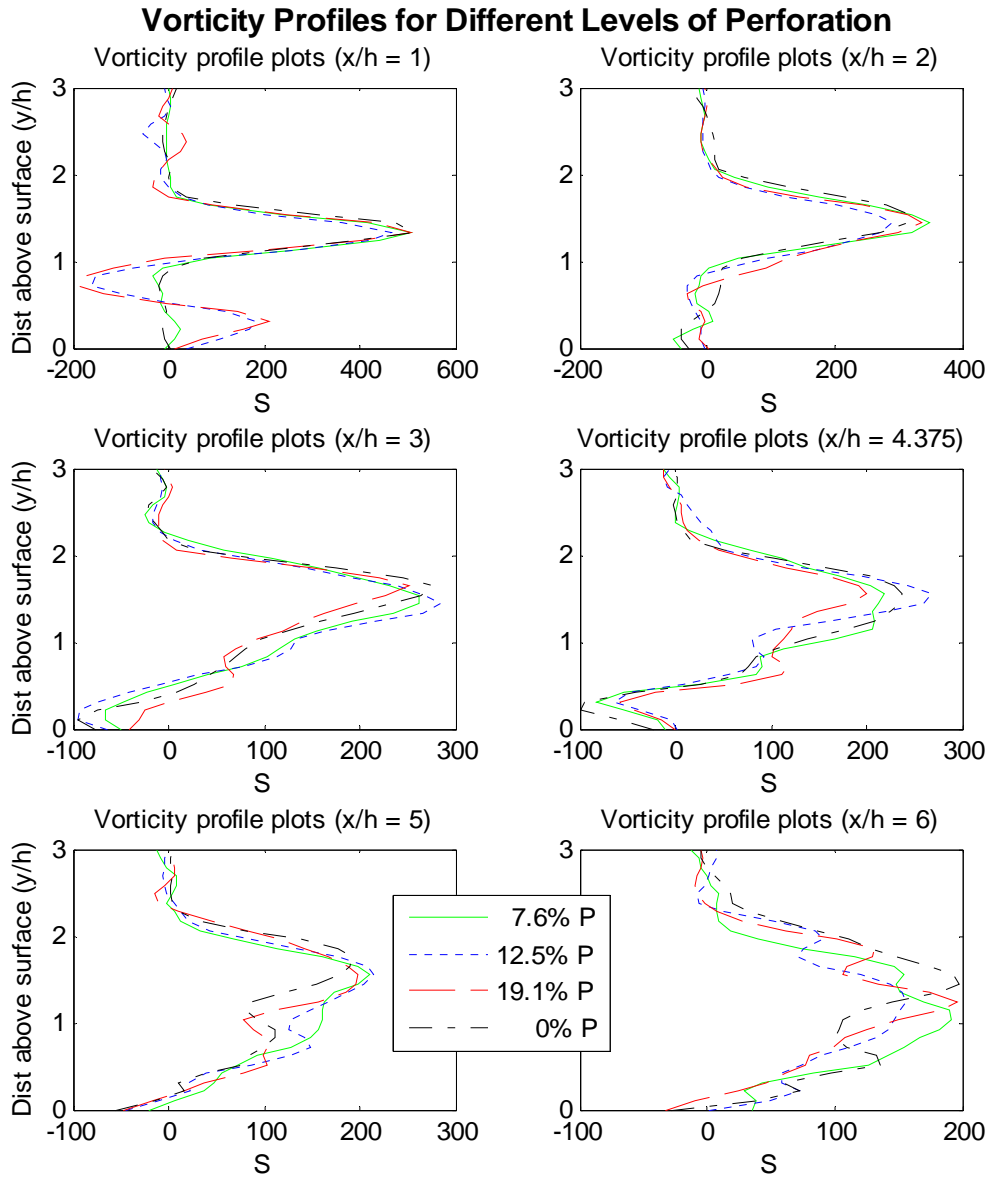


Figure 26. Vorticity profiles for the levels of perforation tested at five different locations downstream of fence. The downstream distance divided by fence height of $x/h = 4.375$ refers to the front edge of the fuel pan.

4.2 Turbulence Intensity

4.2.1 TI Contour Plots

The following plots show the percent turbulence intensity (TI) for each fence setup. The results begin at the edge of the pan and extend three original fence heights downstream. The direction of flow is from right to left and the color scale used is shown at the bottom. Again, the scale is the same for each plot for easy comparison and ranges from 0 to 65 % TI. Like the other plots, the distance along and above the fuel pan are measured in non-dimensional fence heights.

The turbulence was calculated by dividing the magnitude of the root mean square (RMS) velocity by the free stream velocity in the absence of clutter. This is better demonstrated by the equation below.

$$\%TI = \frac{\sqrt{U_{rms}^2 + V_{rms}^2}}{U_1} \times 100 \quad (10)$$

Where U_{rms} and V_{rms} are the RMS velocities in the streamwise and crosswise directions and U_1 is the average free stream velocity in the absence of a fence. The RMS velocities are divided by U_1 instead of the average local velocities, because this makes it possible to compare the turbulence intensity over the entire area of the region of interest. The local velocities that are located at the common center of vortices continuously change direction and the average can be quite small. If this value were used as the numerator in equation (10), then the %TI at these locations would be so large that it would drown out the other locations and a decent comparison would be difficult.

Turbulence Intensity Over Fuel Pan for Various Blockage Ratios

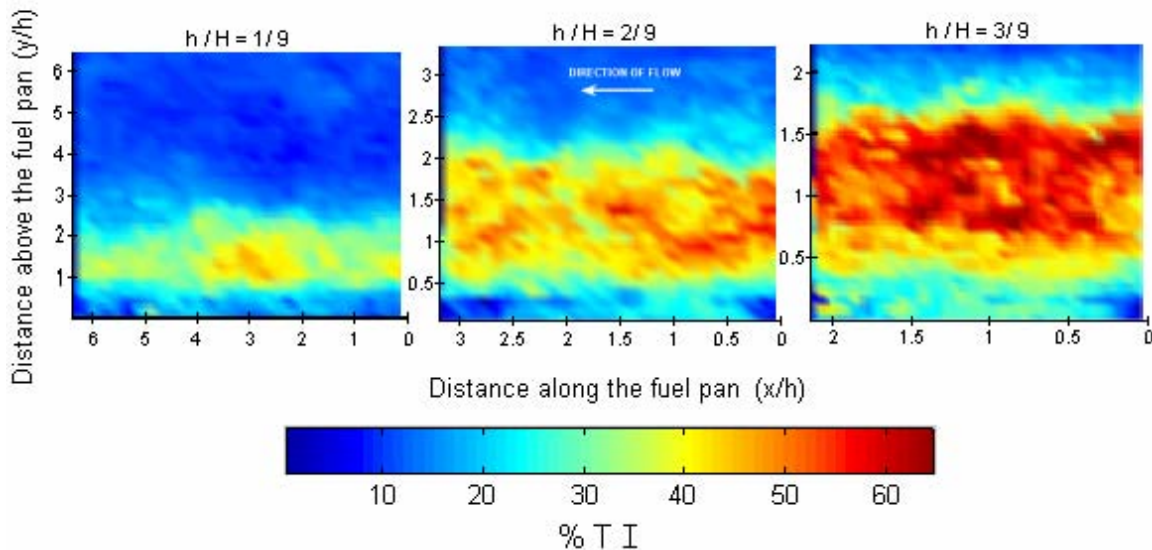


Figure 27. Turbulence intensity (TI) over the fuel pan for 3 different blockage ratios. The TI was calculated from 20 instantaneous velocity measurements and is the RMS velocity divided by the free stream velocity with no fence. The direction of flow is from right to left.

Turbulence Intensity Over Fuel Pan for Various Clutter Elements at $h/H = 2/9$

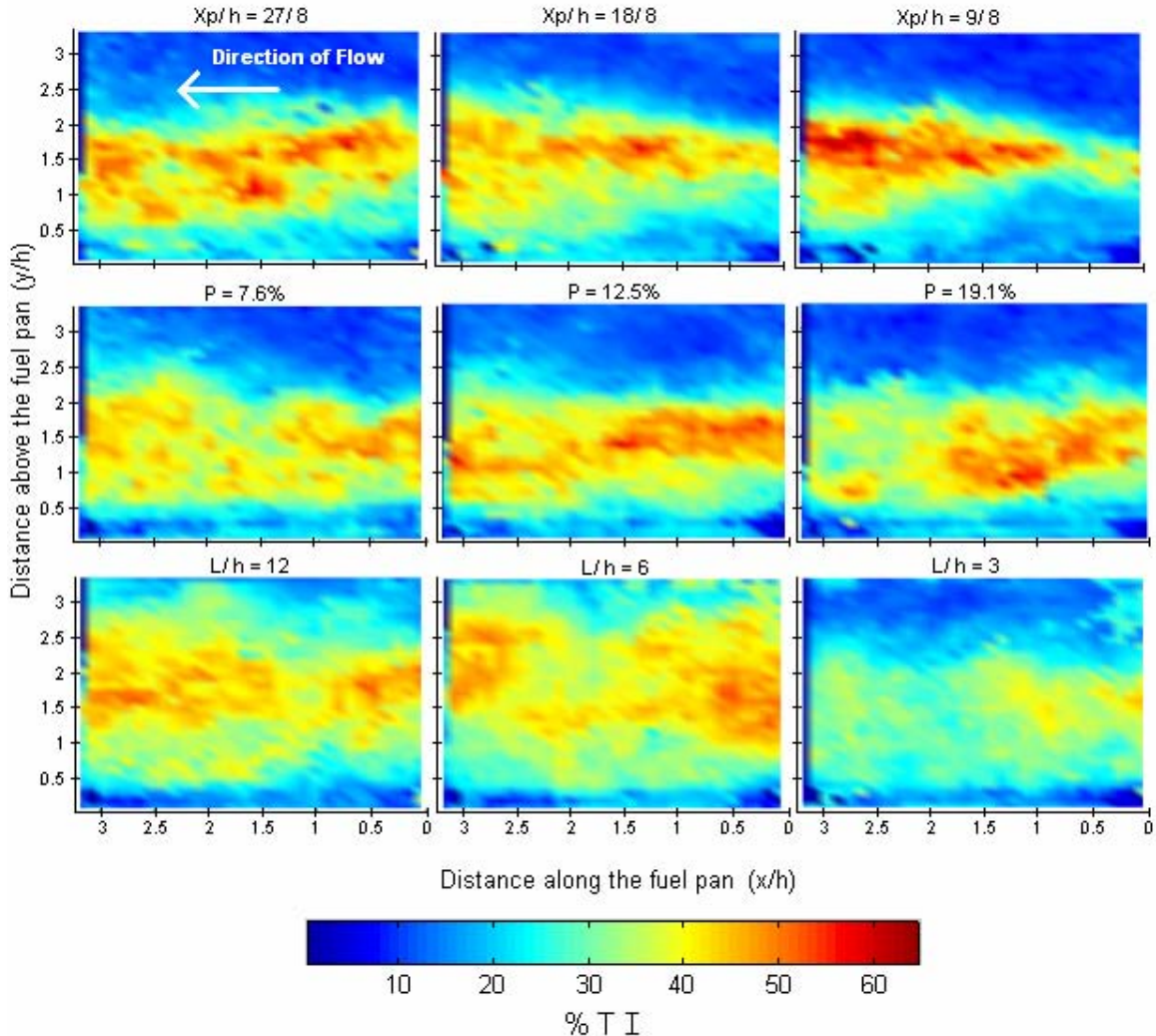


Figure 28. Turbulence intensity (TI) over the fuel pan for 3 fence distances, perforation levels, and fence lengths. Each fence has a blockage ratio of $h/H = 2/9$. The TI was calculated from 20 instantaneous velocity measurements and is the RMS velocity divided by the free stream velocity with no fence. The direction of flow is from right to left.

4.2.2 TI Profile Plots

Vertical profiles of the turbulence intensity for the different blockage ratios and levels of perforation are shown below for different locations downstream of the fence position. The profiles are plotted with non-dimensional variables by using fence heights to describe the distance above the surface and downstream of the fence. The TI for the

different blockage ratios vary greatly from each other and so it was normalized with the square root of the blockage ratio in an attempt to further collapse the profiles.

$$\text{Normalized Turbulence} = \frac{U_{rms}}{U_\infty} \sqrt{\frac{H}{h}} \quad (11)$$

By using the above relation to plot the turbulence profiles, the larger turbulence of the largest blockage ratio better matches the turbulence profile of the smallest blockage ratio. Dividing the RMS velocity by the free stream velocity, U_∞ , for each blockage ratio also aids the collapsing processes since U_∞ is larger for larger blockage ratios. The data collapses fairly well considering the high levels of turbulence intensity, but unfortunately there still exists a considerable amount of variation.

Similar to the contour plots, the TI profiles for different levels of perforation are very close in shape and magnitude. Even when compared to zero percent perforation, the results are still similar. The profiles are so similar, that it was sufficient to divide the RMS velocity by a continuous parameter, U_0 , where U_0 is the free stream velocity for the original fence height. The statistical error for the TI profiles is shown for the location at the edge of the fuel pan. The error for the other locations is similar since the same number of samples is considered and the deviations are comparable.

TI Profile Comparison for Different Blockage Ratios at Various Locations

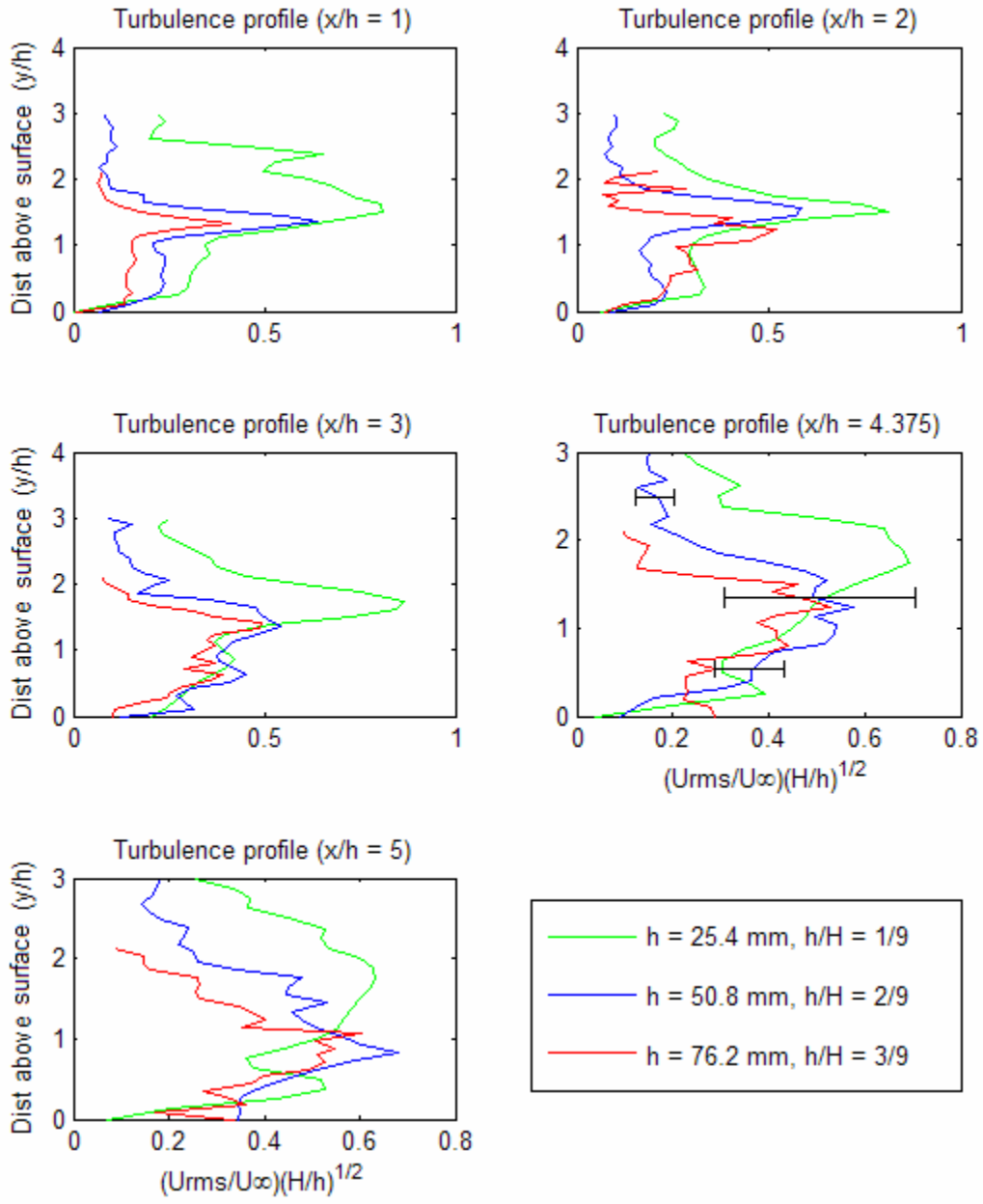


Figure 29. Non-dimensional TI profile comparisons for blockage ratios of $h/H = 1/9, 2/9, 3/9$. The profiles are taken at 1, 2, 3, 4.375, and 5 fence heights downstream of the clutter elements. The height above the surface of the test section is in fence heights, y/h . The streamwise RMS velocity is taken from 20 samples and an example of the associated error is visible for $h = 50.8 \text{ mm}$ at $x/h = 4.375$. The velocity is non-dimensionalized by the free stream velocity and the square root of the blockage ratio. $x/h = 4.375$ represents the edge of the pan.

TI for Different Levels of Perforation at Various Locations

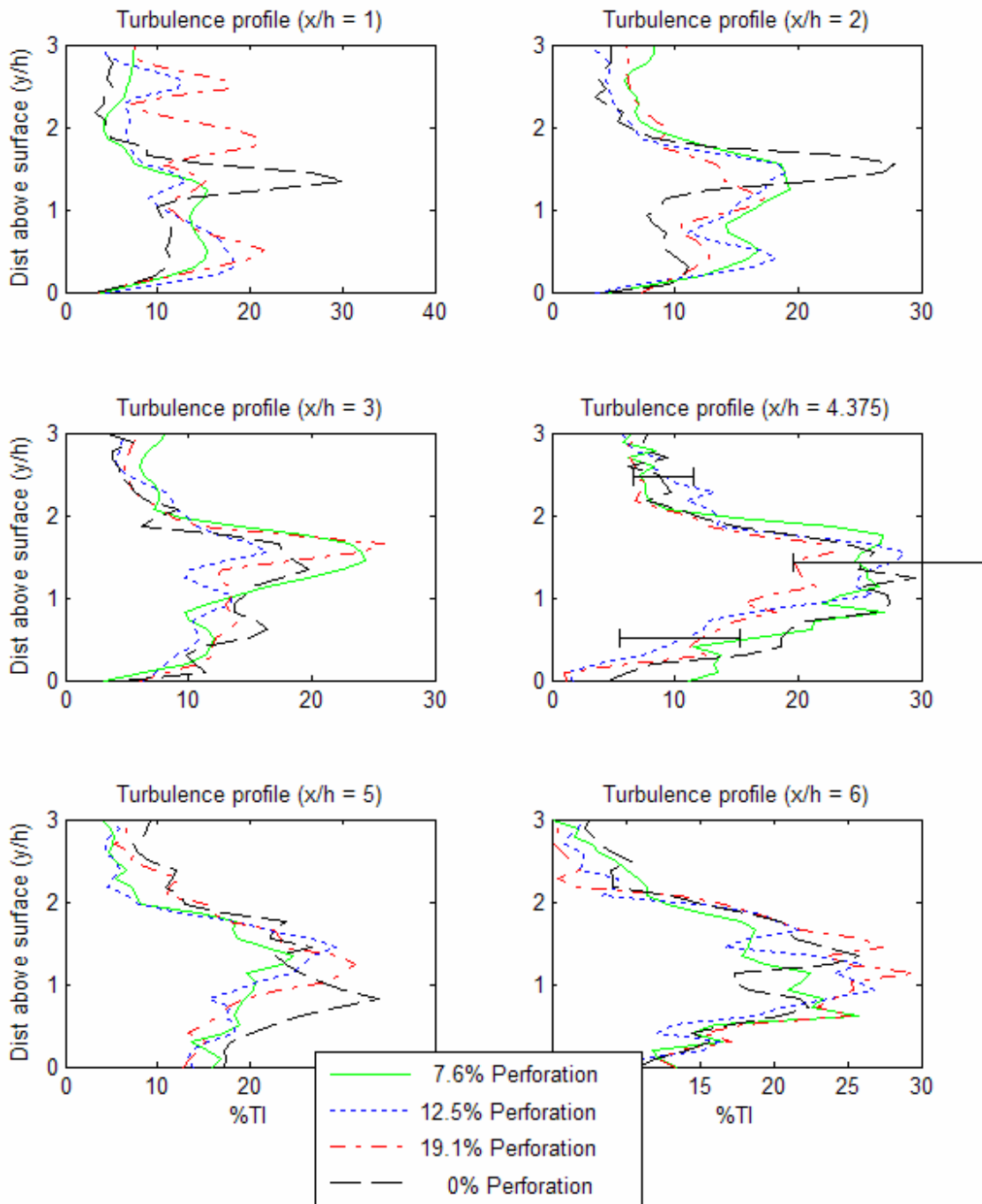


Figure 30. Turbulence profile comparisons for perforation levels of $P = 0, 7.6, 12.5$ and 19.1% . The profiles are taken at 1, 2, 3, 4.375, and 5 fence heights downstream of the clutter elements. The height above the surface of the test section is in fence heights, y/h . The turbulence is taken from 20 samples and an example of the associated error is visible for $P = 12.5\%$ at $x/h = 4.375$. The edge of the pan is located at $x/h = 4.375$.

4.3 Reynolds Stress

The Reynolds stress gives similar results as the turbulence intensity and so only the contour plots are shown for comparison. A contour plot for depicting the Reynolds stress above the fuel pan for each clutter element is shown below in Figure 31 and Figure 32. The same scale is used for each plot for easy comparison. The flow is from right to left and the distance above and along the pan is given in fence heights. The fence heights are of course different for each blockage ratio since the tunnel height never changes.

The Reynolds stress was found by calculating the covariance of the fluctuating components of the 2-D velocity field. Results show a significant change for different blockage ratios and a large difference between the fence lengths of 6 and 3 fence heights. Once again, the level of perforation seems to have little effect. There is also little change with distance to the fuel pan, which differs slightly from the TI plots that show a small increase in turbulence for closer fence positions. However, both results show that the values become spread out as the turbulent shear layer grows downstream of the fence.

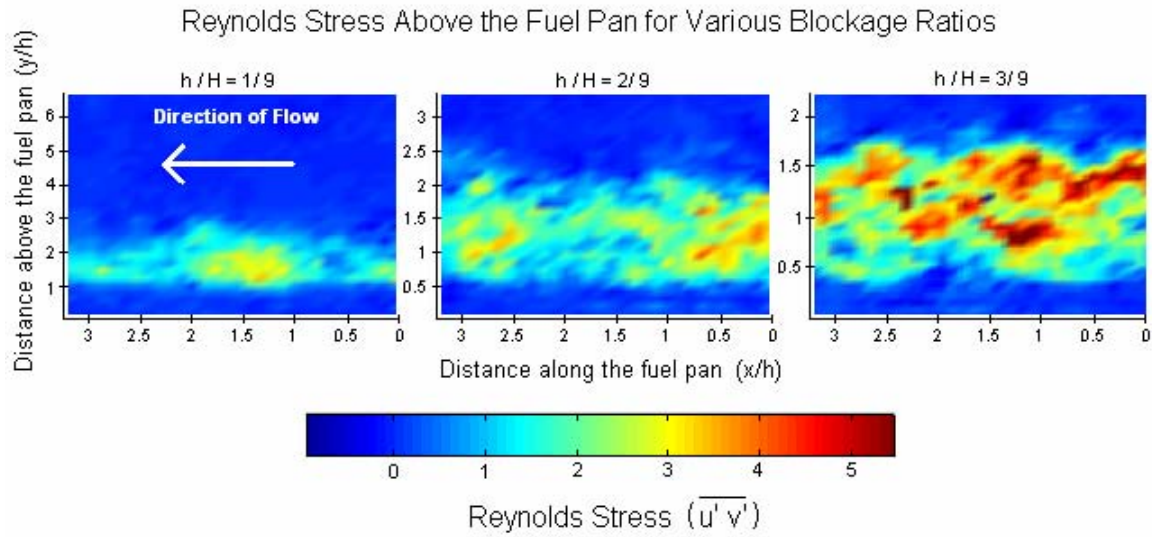


Figure 31. Reynolds stress above the fuel pan for different blockage ratios, h/H . The scale is given at the bottom and is the same for all plots. The flow is from right to left. Values are found by calculating the covariance of the fluctuating components of velocity.

Reynolds Stress Above the Fuel Pan for Various Clutter Elements at $h/H = 2/9$

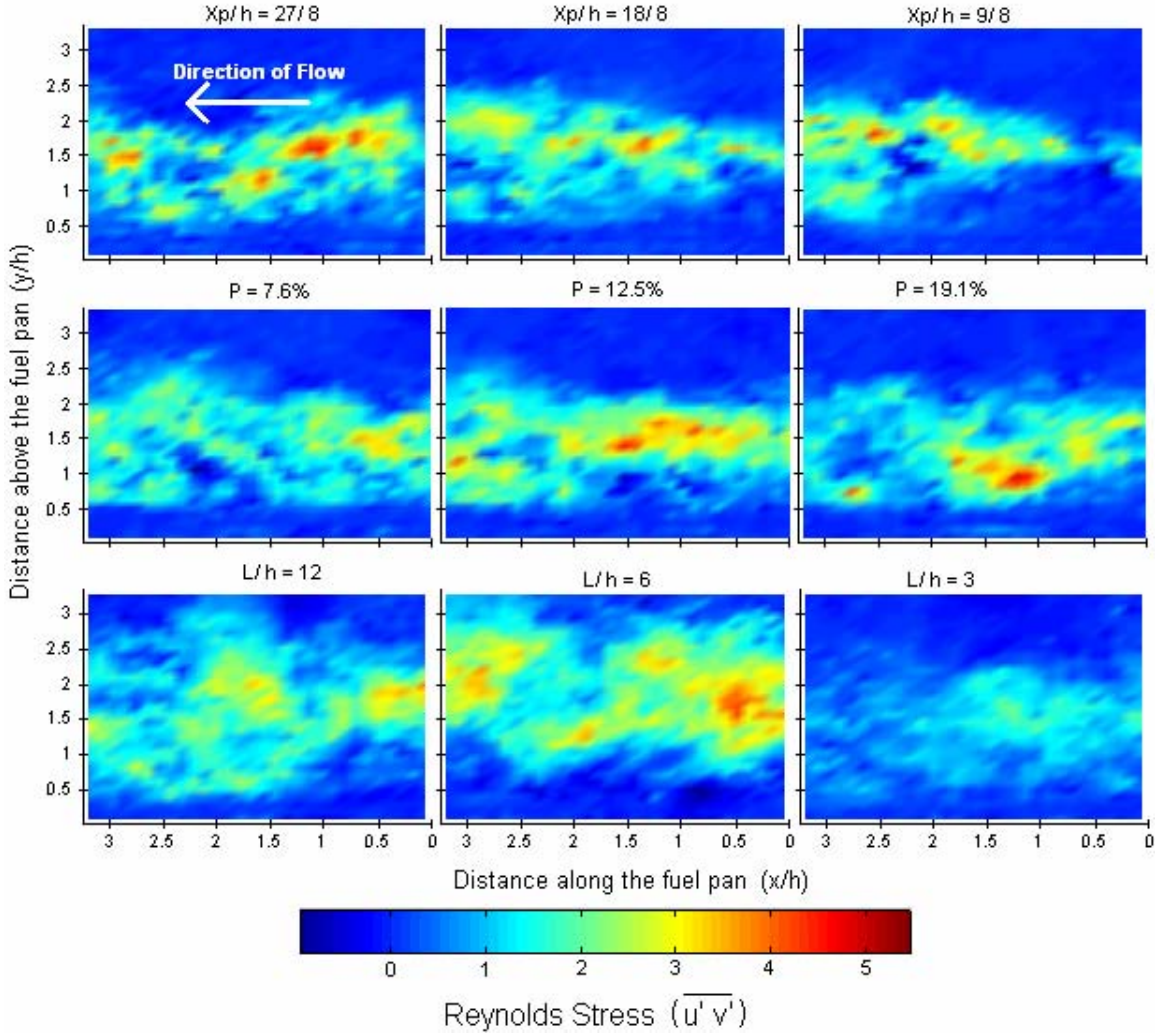


Figure 32. Reynolds stress above the fuel pan for different fence positions, perforation levels and fence lengths. The scale is given at the bottom and is the same for all plots. The flow is from right to left. Values are found by calculating the covariance of the fluctuating components of velocity.

4.4 Integral Length Scale

The Integral length scale over the fuel pan for each clutter element tested is shown below. The values are integrated over a streamwise distance of 3 fence heights and averaged over 20 samples. The values are on the order of 1 fence height, but there is a large variation between samples that result in a statistical error. The associated error is

shown in Figure 33 in the form of error bars and is only given for the original fence since the statistical error is similar for the other fence dimensions.

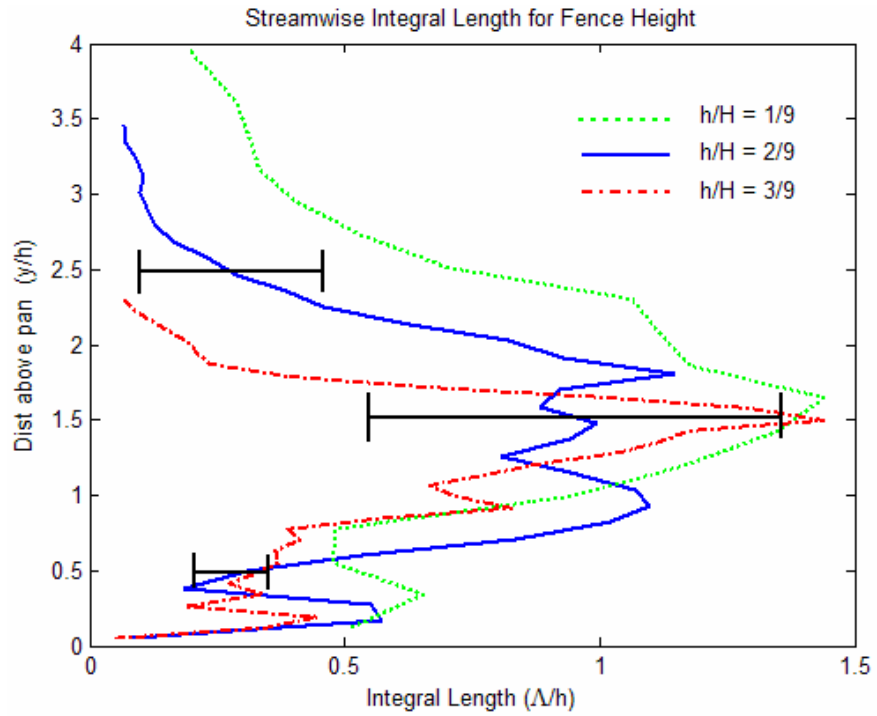


Figure 33. Spatially determined streamwise integral length scale for all fence heights tested. The length scale is averaged over 20 samples in time and the associated error is displayed for $h/H = 2/9$. Length scales were obtained from integration over a streamwise distance of 3 fence heights.

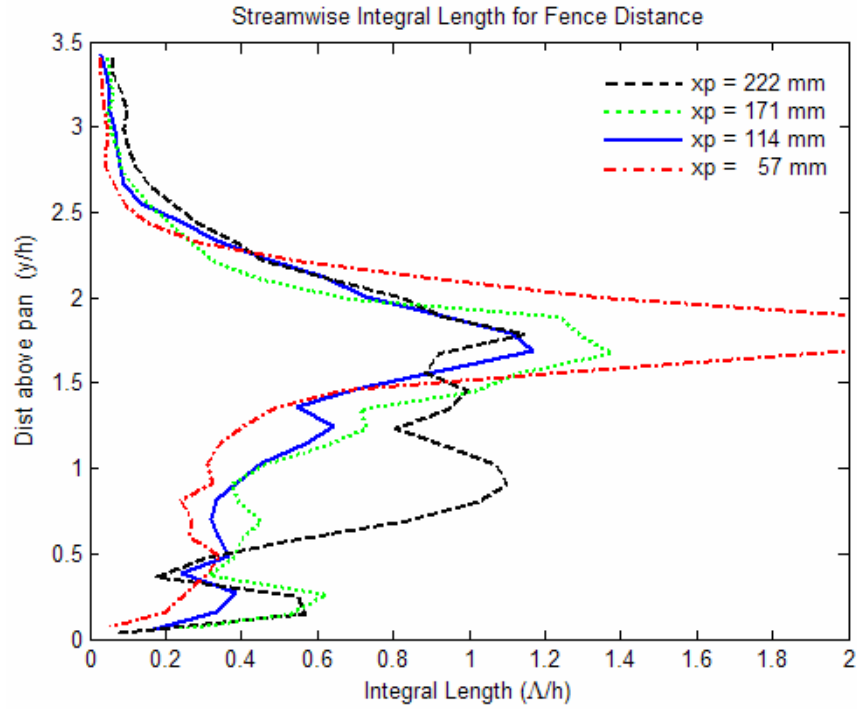


Figure 34. Spatially determined streamwise integral length scale for all fence distances tested, $x_p = 222$, 171 , 114 , and 57 mm. The length scale is averaged over 20 samples in time. Length scales were obtained from integration over a streamwise distance of 3 fence heights.

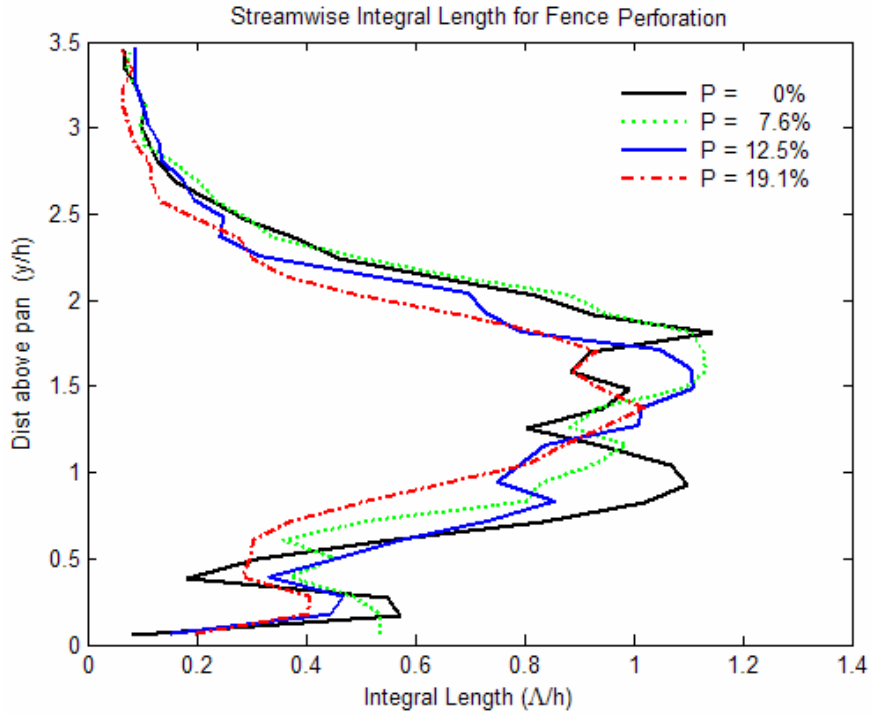


Figure 35. Spatially determined streamwise integral length scale for all fence perforation tested, $P = 0$, 7.6 , 12.5 , and 19.1% . The length scale is averaged over 20 samples in time. Length scales were obtained from integration over a streamwise distance of 3 fence heights.

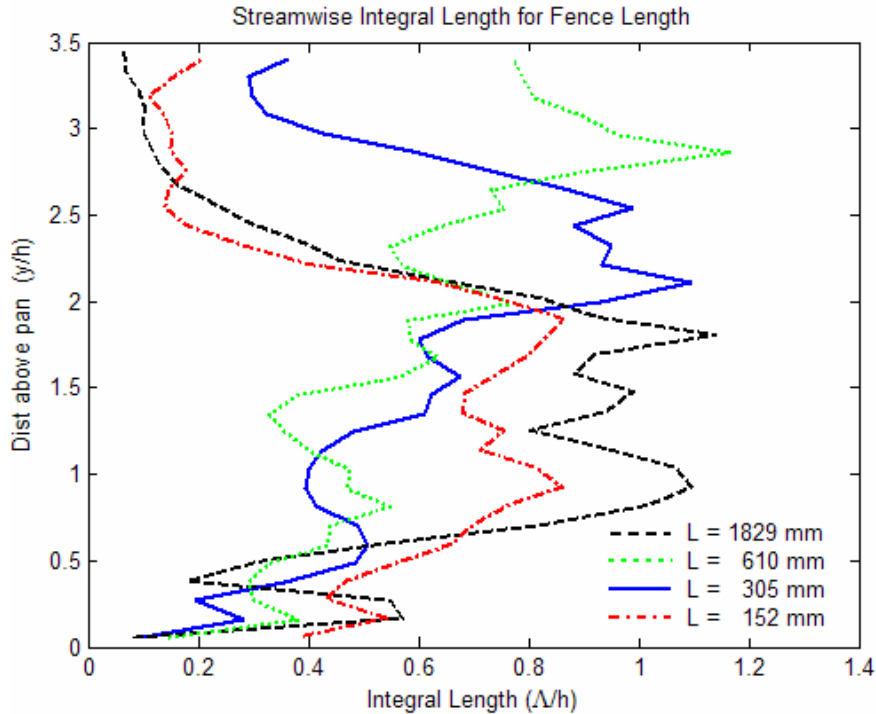


Figure 36. Spatially determined streamwise integral length scale for all fence lengths tested, $L = 152, 305, 610$ and 1829 mm . The length scale is averaged over 20 samples in. Length scales were obtained from integration over a streamwise distance of 3 fence heights.

4.5 Velocity Comparison

4.5.1 Profile Comparisons for Fence Geometries

The following results show the velocity profiles for all three blockage ratios, perforation levels and fence lengths tested. The profiles are shown for the downstream locations of, $x/h = 1, 2, 3, 4.375, 5$, and 6 , where $x/h = 4.375$ represents the upstream edge of the fuel pan. The location $x/h = 6$ is not presented for the variation in blockage ratios because data was not taken that far downstream for the tallest fence height. The results were non-dimensionalized in an attempt to collapse the data into a form that could be used to derive results using fewer variations. The velocity profiles are averaged from 20 samples and, therefore, have a statistical error associated with them. The statistical

error for a select few locations is shown in the form of error bars for $x/h = 4.375$ to give a visual representation of the error involved. A more detailed error analysis including the error associated with the PIV resolution was previously provided in sections 3.3.3 and 3.3.4.

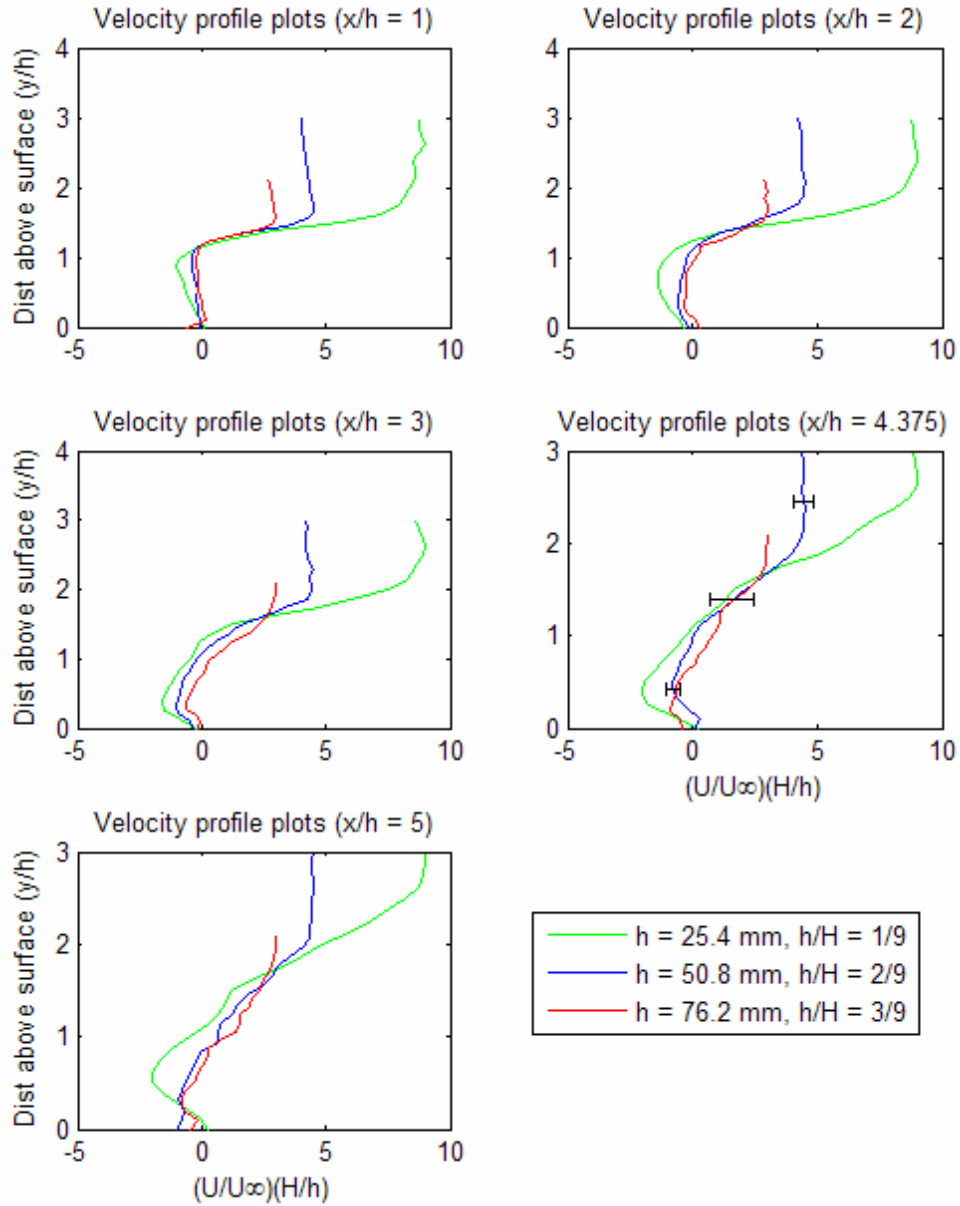


Figure 37. Non-dimensional velocity profile comparisons for blockage ratios of $h/H = 1/9, 2/9, 3/9$. The profiles are taken at 1, 2, 3, 4.375, and 5 fence heights downstream of the clutter elements. The height above the surface of the test section is in fence heights, y/h . The velocity is time averaged over 20 samples and an example of the associated error is visible for $h = 50.8 \text{ mm}$ at $x/h = 4.375$. The velocity is non-dimensionalized by the blockage ratio and the free stream velocity. The edge of the pan is located at $x/h = 4.375$.

Velocity Profiles for Various Levels of Perforation

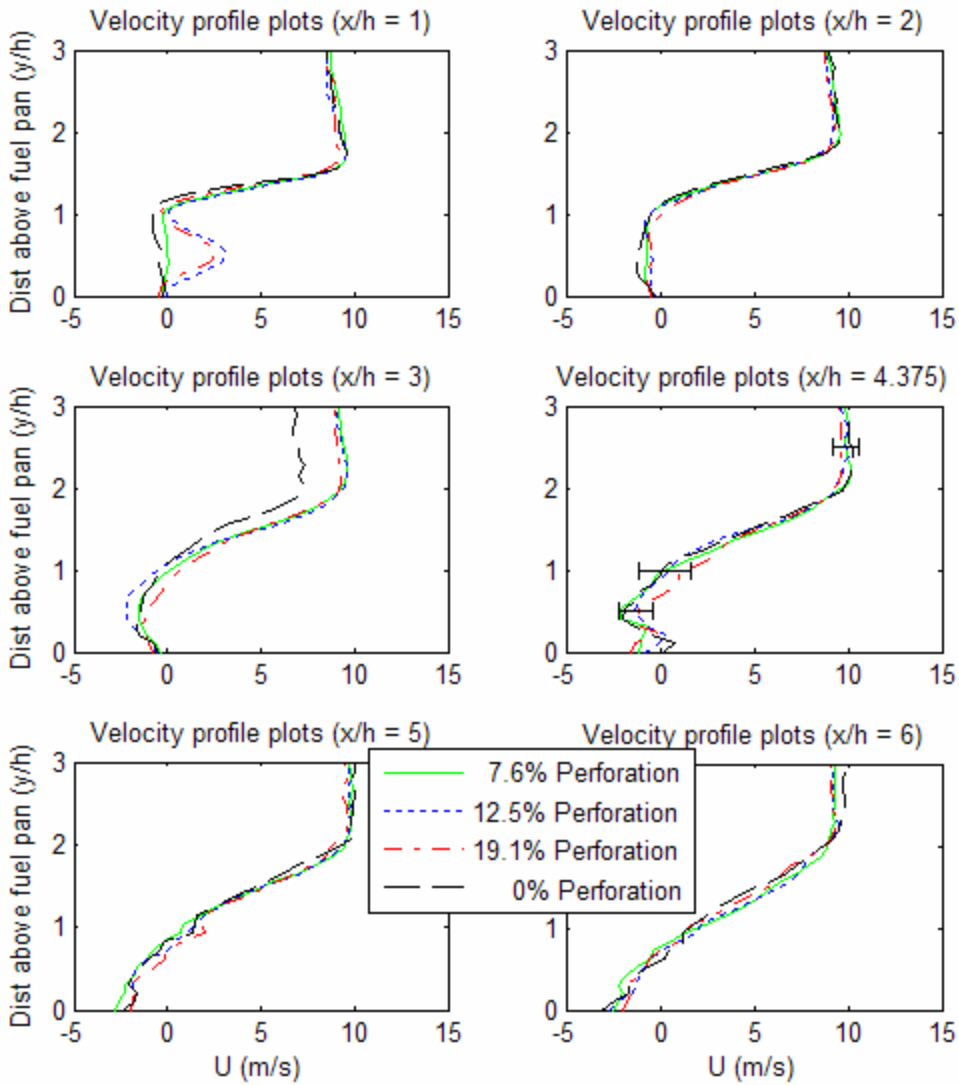


Figure 38. Velocity profile comparisons for perforation levels of $P = 0, 7.6, 12.5$ and 19.1% . The profiles are taken at 1, 2, 3, 4.375, and 5 fence heights downstream of the clutter elements. The height above the surface of the test section is in fence heights, y/h . The velocity is time averaged over 20 samples and an example of the associated error is visible for $P = 12.5\%$ at $x/h = 4.375$. The edge of the pan is located at $x/h = 4.375$.

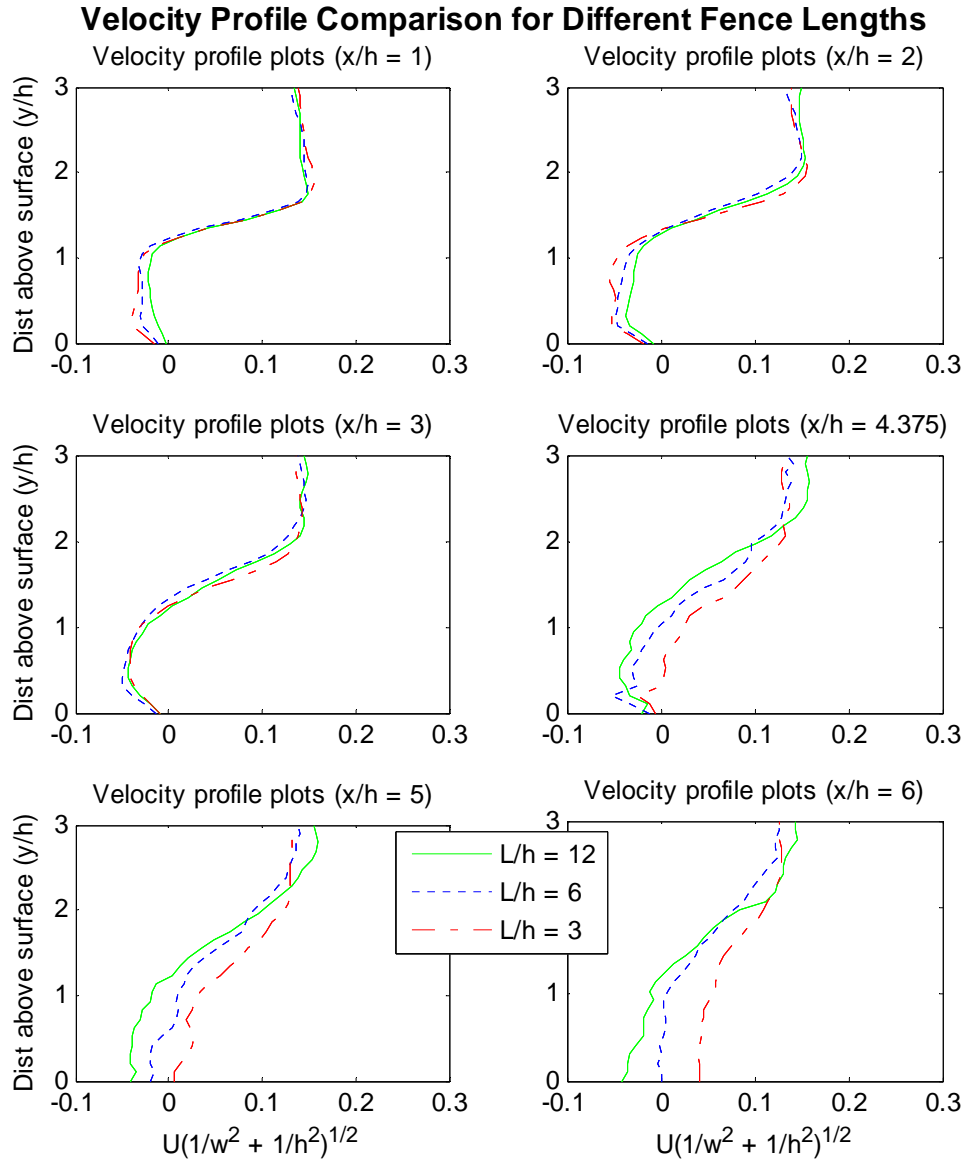


Figure 39. Velocity profile comparisons for fence lengths of $L/h = 12, 6$, and 3 . The profiles are taken at $1, 2, 3, 4.375, 5$, and 6 fence heights downstream of the clutter elements. The height above the surface of the test section is in fence heights, y/h . The velocity is time averaged over 20 samples. The edge of the pan is located at $x/h = 4.375$.

4.5.2 Comparison to Literature

A comparison of the PIV data and the data taken by Good and Joubert [19] is also provided. Good and Joubert used a blockage ratio of $1/9$ and is the same ratio as the smallest one tested during the current research. The two data sets are plotted together in

Figure 40 for four different locations downstream of the fence, determined by the locations measured by Good and Joubert. Their data was taken using pitot static tubes with turbulent flow and without the presence of a fuel pan. The lack of a fuel pan can be seen in the obvious differences between the data at the last two downstream locations. The profile shapes above the shear layer are similar, but a strong difference in the reverse flow can be seen near the surface. The reverse flow for the present data is nearly all but gone at the edge of the pan. The use of intrusive measurement techniques by Good and Joubert most likely has an effect as well. Despite the differences at far downstream locations, the two datasets correlate well for locations closer to the fence.

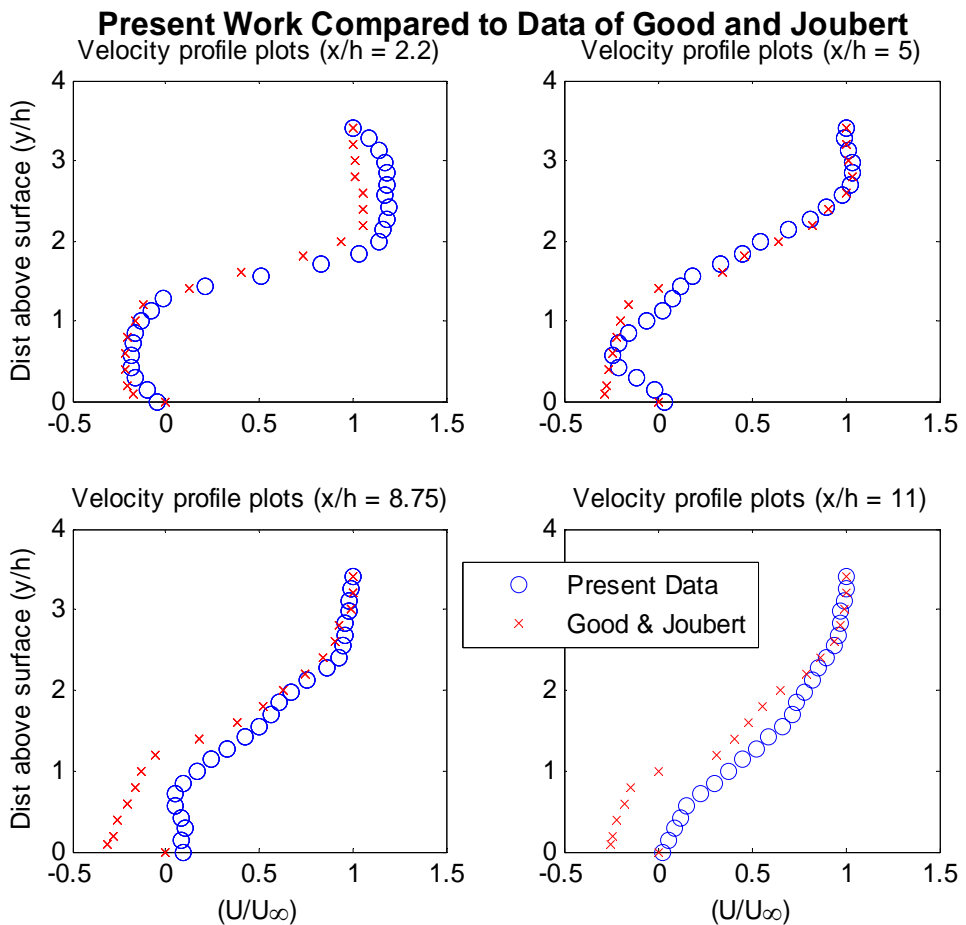


Figure 40. Non-dimensional profile comparison for time averaged PIV data and data from Good and Joubert [0] for a blockage ratio of 1/9. Good and Joubert used pitot static tubes with turbulent flow and no fuel pan. The location of each profile is given by the downstream distance divided by the fence height, x/h .

4.6 Curve Fitting

As shown above, reasonable estimates of the velocity profiles for differing blockage ratios can be obtained from one blockage ratio through careful non-dimensional analysis. It is also possible to take it a step further and create an equation to fit the general shape of the velocity profile curve. This has been done and is shown below for the blockage ration of the original fence, $h/H = 2/9$. In the figure below, the velocity is divided by its free stream velocity, U_∞ . The strong curvature in the velocity profiles make for a difficult and complicated curve fit. The curves are difficult to model because of the significant reverse flow near the surface and the greater than free stream velocity above the shear layer. However, a curve fit was found that follows the shape of the velocity profile rather well as it develops downstream of the fence.

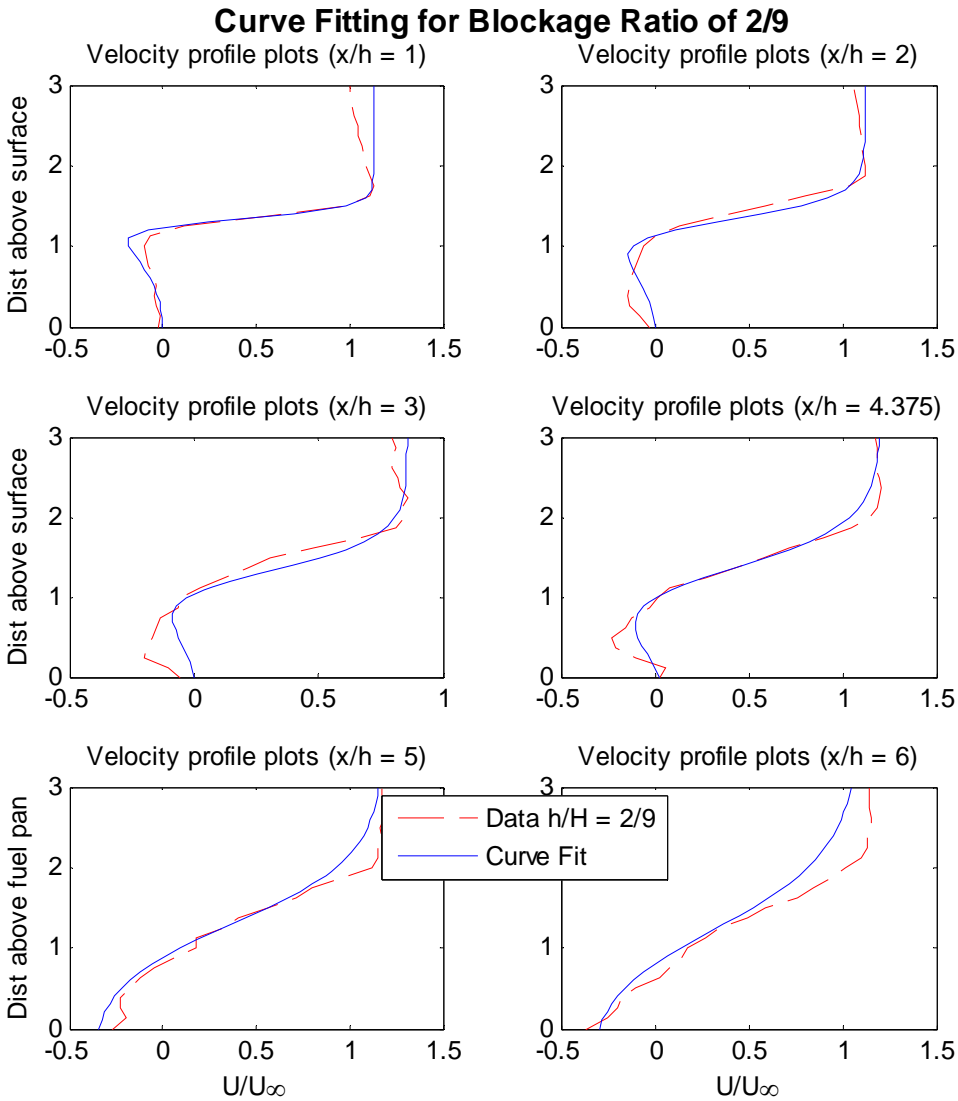


Figure 41. Comparison of curve fit equation and data for a blockage ratio of 2/9. The Velocity is non-dimensionalized with the free stream velocity.

The equation used is of the form of a logistic curve and is a function of the non-dimensional variables, x/h and y/h , and is given as,

$$\frac{U}{U_\infty} = \frac{-U_r}{1 + \exp\left(\frac{13(y_h - 1.3)}{x_h}\right) - \left(\frac{y_h}{3 - x_h / 6}\right)^{2-x_h/6}} + U_r \quad (12)$$

where x/h and y/h have been replaced with x_h and y_h for simplicity and U_r is the maximum velocity divided by the free stream velocity. The basic logistic curve is of the form $1/(1 + \exp)$ and gives the general “S” shape curve that closely resembles the velocity profile [31]. This type of equation is often used for modeling population percentages since the curve gradually rises from zero and levels off at 1. In order to achieve the extra inflection in the curve near zero, which represents the reverse flow, another term had to be added in the denominator with the exponent term.

Due to the presence of the fuel pan, a slight change to the equation had to be made for velocity profiles located over the fuel pan, starting at $x/h = 4.375$. The changes are shown below.

$$\frac{U}{U_\infty} = \frac{-U_r}{1 + \exp\left(\frac{13(y_h - 1.3)}{x_h}\right) - \left(\frac{y_h}{2}\right)^{2+x_h}} + U_r \quad (13)$$

The changes in the curve fit equation for profiles over the pan make the equation simpler because the profiles no longer have to curve towards a zero velocity. The no-slip condition is applied to a moving liquid instead of a stationary surface and the velocity is not required to be zero at the surface. This allows for a stronger reverse flow near the surface and combined with the growth of the shear layer gives a profile that is more linear.

4.7 Flame Spread Rates

The flame spread rates for all fence configurations tested are presented below in Table 3. The spread rate is inconsistent during a single run due to variations in flow speed near the surface, so the average spread rate over the entire pan is reported along with the max and min velocities. It is apparent from looking at these values that there exists a large variation in the flame speed as it progresses upstream. This phenomenon is obvious when viewing the video recordings of the flame spread.

Table 3. Flame spread rate for different fence configurations.

Flame Spread Rate (cm/s)			
Clutter Type	Avg	Max	Min
Height (cm)			
2.54	64	149	0
5.08	213	297	114
7.16	191	206	183
Length (cm)			
61	65	183	0
30.5	31	114	0
15.2	10	76	0
Distance (cm)			
17.2	73	149	0
11.4	213	297	137
5.7	185.5	343	114
Perforation %			
7.6	164	229	114
12.5	121	206	34
19.1	177	228	114

There is a definite reduction in flame spread rate when the clutter height is reduced. However, increasing the height appears to have little effect even though there is a significant increase in reverse flow. Earlier results showed that different levels of perforation have little effect on the flow field and the same seems to be true for the flame spread rate. It changes slightly from one percentage to another, but the changes remain

within the +/- 57 cm/s error. The most surprising result is the relatively small spread rate associated with the fence distance of 17.2 cm. It is possible that this unusual reading is a result of the fuel being cool since it was the first test run made that day. This is further backed by the flame spread video showing the flame propagating upstream but not stabilizing downstream.

A non-surprising result is that decreasing the clutter length drastically reduces the spread rate, which is in agreement with the PIV data showing large reductions in the recirculation region. The presence of the recirculation region is important because it provides a concurrent flow environment for flame spread. According to Hirano and Suzuki [14], the flame spread rate should match the concurrent flow velocity when it is greater than the quiescent flame spread rate. The average flame spread rate and air speed above the portion of the fuel pan that was analyzed is presented below.

Table 4. Comparison of the average flame spread rate to the average air speed above the upstream half of the fuel pan. Negative air speeds indicate opposed direction of flow or lack of reverse flow.

Flame Speed Compared to Air Speed		
Fence Configuration	Air Velocity Above Pan	Avg Vf at Upstream half
Height (cm)	(cm/s)	(cm/s)
2.54	-90	64
5.08	160	213
7.16	170	200
Length (cm)		
61	110	95
30.5	0	82
15.2	-150	10
Distance (cm)		
17.2	190	152
11.4	140	171
5.7	110	160
Perforation %		
7.6	200	205
12.5	140	171
19.1	120	182

The negative air velocities given in Table 4 represent opposed flow, meaning a lack of reverse flow over the fuel pan. If the quiescent flame spread rate is estimated to be approximately 150 to 180 cm/s (the spread rate between 20 and 25 °C for methanol, a similar fuel) then the flame velocity is always within the experimental error of the quiescent spread rate for concurrent air velocities around 200 cm/s or less. These results are sensible and it is expected that the flame spread rate would match the reverse flow should its velocity exceed 200 cm/s. In order to investigate this subject, it is recommended that larger air speeds are used and many test runs are performed to acquire reliable flame spread rates for reverse velocities much greater than the quiescent flame spread rate.

Chapter 5. Conclusion

5.1 Test Matrix Reduction

By using the appropriate non-dimensional parameters, the data for different fence configurations can be collapsed and predictions of flow characteristics can be made. However, the degree of success varies for the different fence types. The velocity and turbulence profiles are very similar when using the fence height as the non-dimensional parameter for measuring distance above the surface and downstream of the fence.

This method works best for different levels of perforation, but that is because the holes placed in the fence seem to have little impact on the flow field. It would, therefore, not be worthwhile to include changes in fence perforation among the different configurations in the experimental test matrix, at least not for the levels of perforation tested and presented in this paper. But it might be interesting to observe the effects of perforation levels much greater than the ones tested, although the minimal variations in flow measurements observed suggest that the results would be insignificant.

The data for different blockage ratios, however, are of great importance and can be collapsed with reasonable success, especially below the shear layer where flow characteristics should have the most impact on flame spread. Therefore, the experimental matrix can be reduced to using the single original clutter element when measuring the downstream flow field for the purpose of analyzing its effects on flame spread. However, this is only advisable when considering heights within 50 % of the original fence height, since values beyond that may result in a considerable amount of variation.

Velocity profiles for varying fence lengths are easily collapsed within one fence length of the shortest fence, but begin to diverge farther downstream. And the profiles are difficult to compare because of the transition from 2-D to 3-D flow, the effects of which can be seen in the decreasing velocity and turbulence intensity measured in the 2-D plane. Because of the 3-D effects and the added unknowns that come about as a result, the quantitative results are unpredictable and changes in fence length should be avoided in order to maintain as much of a 2-D flow as is possible. Introducing variations in the third dimension should only be done if the use of systems with 3-D measuring capabilities is available, such as stereo PIV.

Prediction efforts can also be assisted by curve fitting the data. An equation is available that follows the velocity profile fairly well as it develops downstream of the fence, but the presence of the fuel pan and the liquid inside must be taken into account. The equation models the velocity profile best below the shear layer, where as mentioned before the effects on flame spread are most prominent.

5.2 Effects on Flame Spread Rate

Changes in fence dimensions and location will have a significant impact on the flame spread rate. This is due to the changes in downstream turbulence, vorticity, and reverse flow associated with different fence configurations. The parameter that is likely to have the greatest impact on flame spread is the blockage ratio, which affects all three of the aforementioned flow characteristics. An increase in blockage ratio will result in a considerable increase in turbulence intensity. Not only does the magnitude increase, but the turbulence occupies a larger area and extends farther downstream as well. A lesser,

but still considerable increase in vorticity is also associated with an increasing blockage ratio.

Changes in turbulence intensity and vorticity will have a multitude of effects on the flame spread rate. Increases in these phenomena will affect the flame speed by convectively cooling the reaction, and thereby, slowing it down. This is also accomplished with the movement of cooler air molecules from the free stream to within the vicinity of the flame by means of turbulent transportation. However, flame spread may be aided by enhanced mixing of fuel and oxidizer, but this benefit will be overshadowed by the drastic increase in turbulence and vorticity associated with separated flow behind a fence.

Increases in the blockage ratio also result in a considerable increase in reverse flow along the surface of the fuel pan. This can be seen in the velocity profiles shown earlier and the raw data presented in Appendix A. The presence of reverse flow creates a transition from opposed-flow to concurrent-flow flame spread. This will be the most significant effect of the obstruction since the flame spread rate is known to match the velocity of the concurrent air flow in similar situations. This implies that an increase in block ratio will most likely result in a faster flame spread rate.

The location of the fence relative to the fuel pan will also have a significant impact on the flame spread rate. The turbulence intensity and vorticity are at their largest values when directly behind the fence. Although these values are greater at this location, they exist well above the surface of the fuel and within the shear layer. As the fence is placed further upstream of the fuel pan, the largest values of turbulence intensity and vorticity are less than when the fence is closer. However, the values near the surface of

the fuel are greater due to the growth of the shear layer. This slight increase in turbulence and vorticity will help to retain fuel vapor without drastically increasing the convective cooling. This, combined with an increase in reverse flow, will likely increase the flame spread rate with distance. But it should be mentioned that this effect is not linear since the flow will eventually reattach downstream and the reverse flow will disappear.

Changing the fence height and location will have a significant influence on the flame spread rate, but increasing the amount of fence perforation will have little if no effect. There might be an exception for directly behind the fence, where the spacing of the holes is relevant, but the effects will be mostly nonexistent for more than one or two fence heights downstream. However, changing the fence length will have a considerable effect. As the length is shortened to 3 fence heights, the recirculation region above the fuel pan nearly all but disappears. This means that a decrease in fence length will result in a reduction in flame spread rate. There will also be other effects associated with the emergence of velocity and turbulence components in the third dimension, but these effects are difficult to predict without proper measurement techniques.

It is important not only to consider the effects on gas dynamics, but on the liquid-phase flow as well. As mentioned earlier, the convection of liquid ahead of the flame is one of the primary modes of heat transfer. The strong reverse flow observed will likely aid flame spread since it is in the same direction as the liquid convection. However, it is uncertain how the liquid flow field will react since the fuel pan lies in a recirculation region characterized by chaotic air flow.

5.3 Recommendations for Future Work

Future work should involve extensive flame spread tests, with special attention paid to the flow structures along the surface of the fuel pan. A PIV set up with a faster camera will allow the observation of flow structures as they develop downstream of the fence. PIV is an excellent tool for this, but special considerations must be made for the size of the area investigated since pixel resolution can be an issue when investigating air flow with a large velocity dynamic range. It would also be valuable to use stereo PIV to obtain a 3-D visual representation of the flow field since the 3-D effects of shorter fence lengths will no doubt have an impact on the flame spread.

Another potential area of research would be to investigate the dependence of flame spread on the turbulence intensity of the wind tunnel. This could be easily accomplished by varying the dimensions of the turbulence grid. This information would be vital for understanding flame spread inside an engine nacelle since they are undoubtedly characterized by a wide range of turbulence levels.

It would also be beneficial to investigate the liquid flow field in the fuel pan as different clutter elements are tested and while a flame is propagating. Liquid convection is a primary mechanism in liquid flame spread should be taken into consideration when predicting flame spread behavior.

APPENDIX A

Velocity contour plots overlaid with streamlines are an excellent way to quickly observe information about the flow that is both qualitative and quantitative. The contour plots below show the magnitude of the velocity ranging from 0 to 10.5 m/s. Since only the magnitude is shown, reverse flow can only be identified by the direction of the streamlines. It is also important to note that these plots are made from averaged data and do not depict instantaneous velocities. Instantaneous plots would show the individual eddies, whereas the plots below are better suited for viewing the general characteristics of the separation region. The velocity magnitudes are given by the color bar provided in the first plot. All the proceeding figures use the same scale.

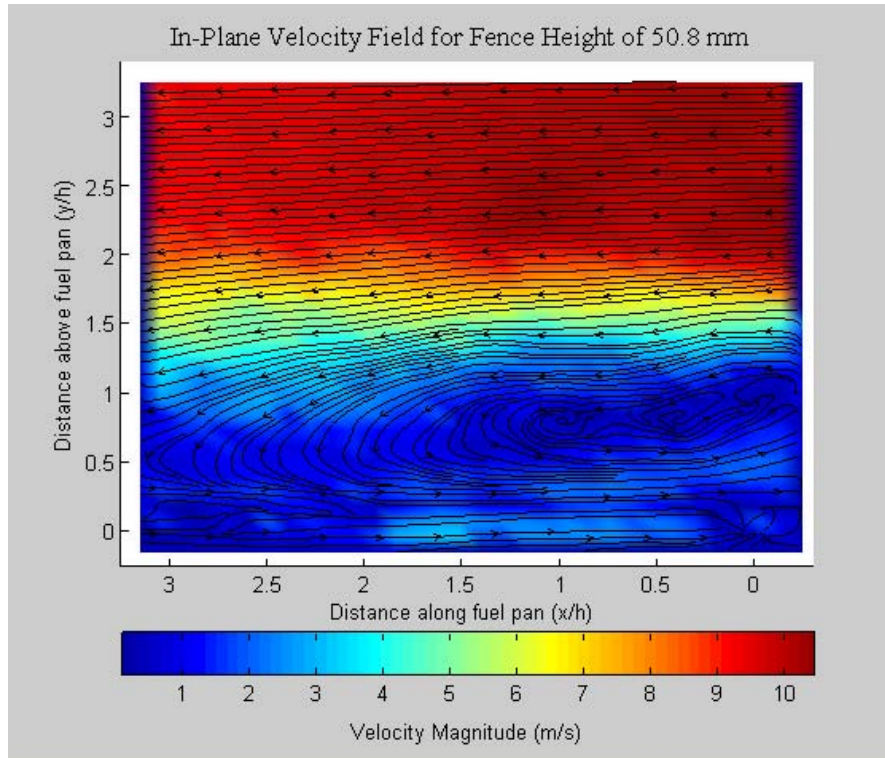


Figure 42. Averaged velocity contour plot with overlaid streamlines at a location over the pan and for a fence height of 50.8 mm (original fence). Position along and above the pan are given in non-dimensional units in terms of the fence height. Velocity scale ranges from 0 to 10.5 m/s. The upstream edge of the fuel pan is given by $x/h = 0$.

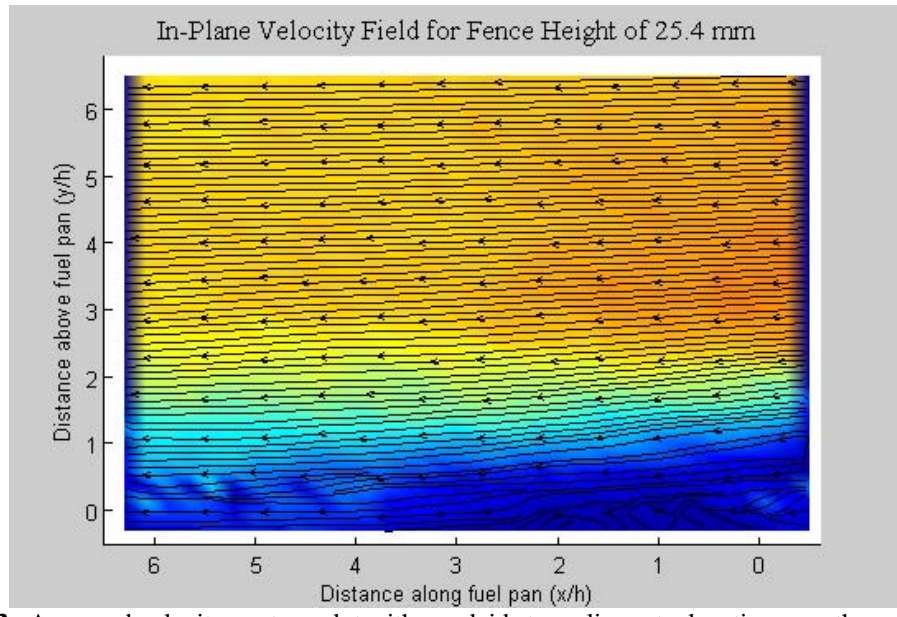


Figure 43. Averaged velocity contour plot with overlaid streamlines at a location over the pan and for a fence height of 25.4 mm. Position along and above the pan are given in non-dimensional units in terms of the fence height. Velocity scale ranges from 0 to 10.5 m/s. The upstream edge of the fuel pan is given by $x/h = 0$.

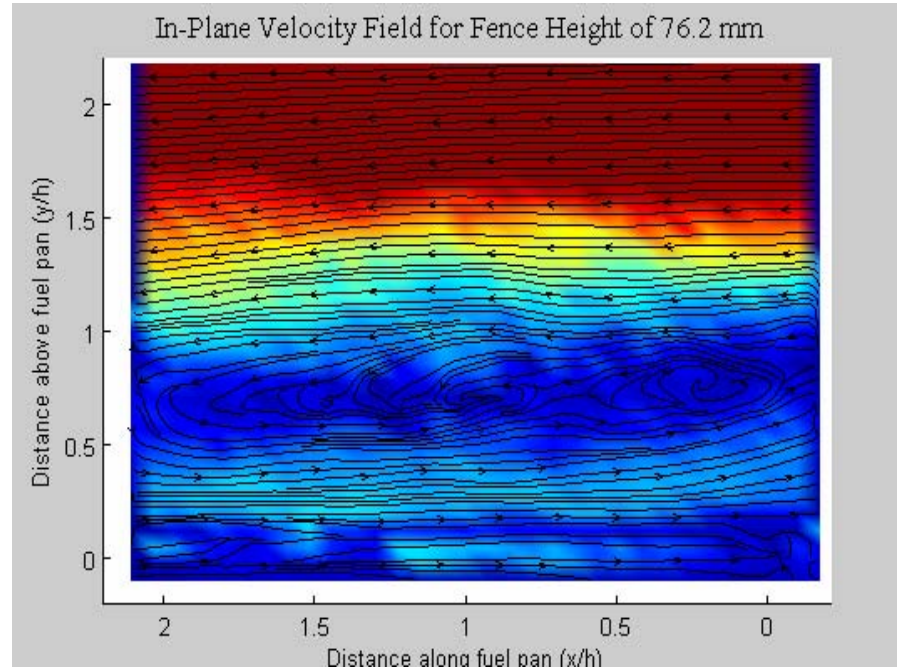


Figure 44. Averaged velocity contour plot with overlaid streamlines at a location over the pan and for a fence height of 76.2 mm. Position along and above the pan are given in non-dimensional units in terms of the fence height. Velocity scale ranges from 0 to 10.5 m/s. The upstream edge of the fuel pan is given by $x/h = 0$.

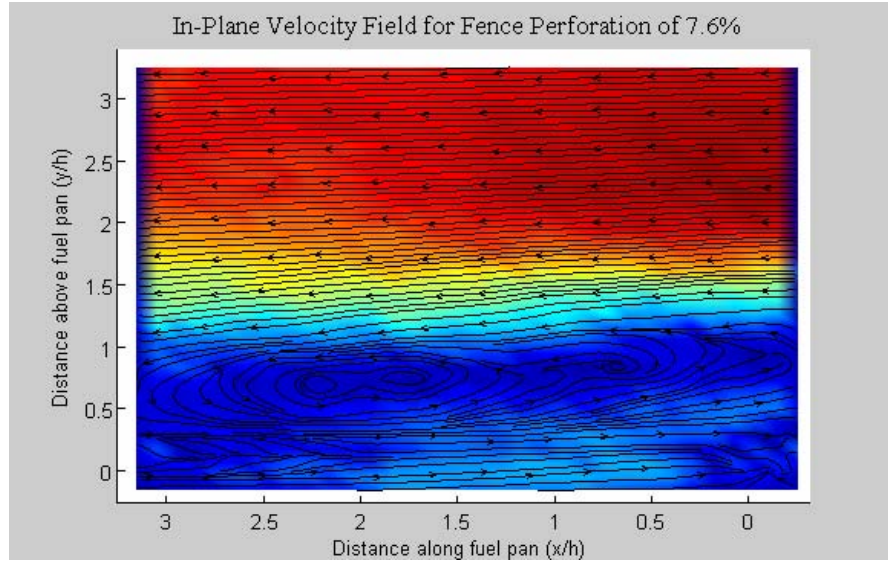


Figure 45. Averaged velocity contour plot with overlaid streamlines at a location over the pan and for a fence perforation of 7.6%. Position along and above the pan are given in non-dimensional units in terms of the fence height. Velocity scale ranges from 0 to 10.5 m/s. The upstream edge of the fuel pan is given by $x/h = 0$.

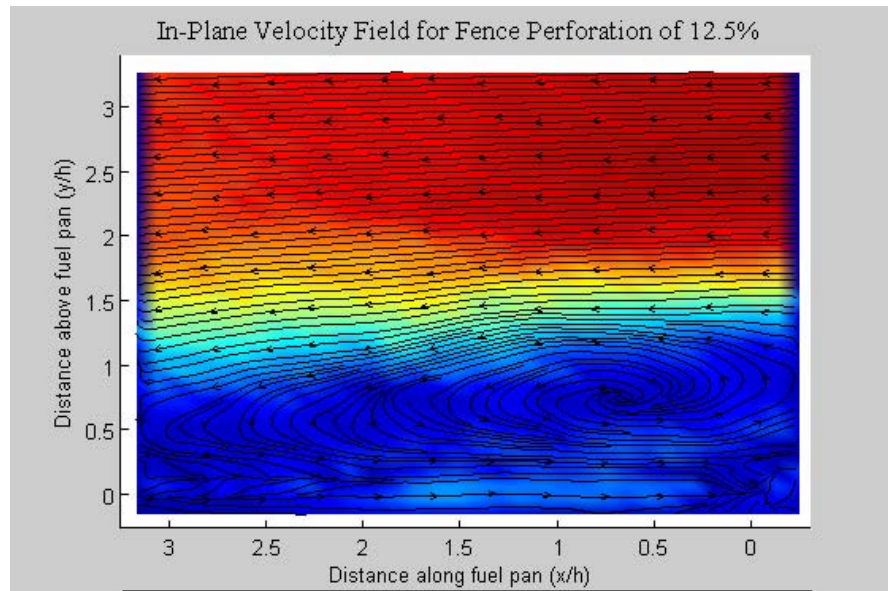


Figure 46. Averaged velocity contour plot with overlaid streamlines at a location over the pan and for a fence perforation of 12.5%. Position along and above the pan are given in non-dimensional units in terms of the fence height. Velocity scale ranges from 0 to 10.5 m/s. The upstream edge of the fuel pan is given by $x/h = 0$.

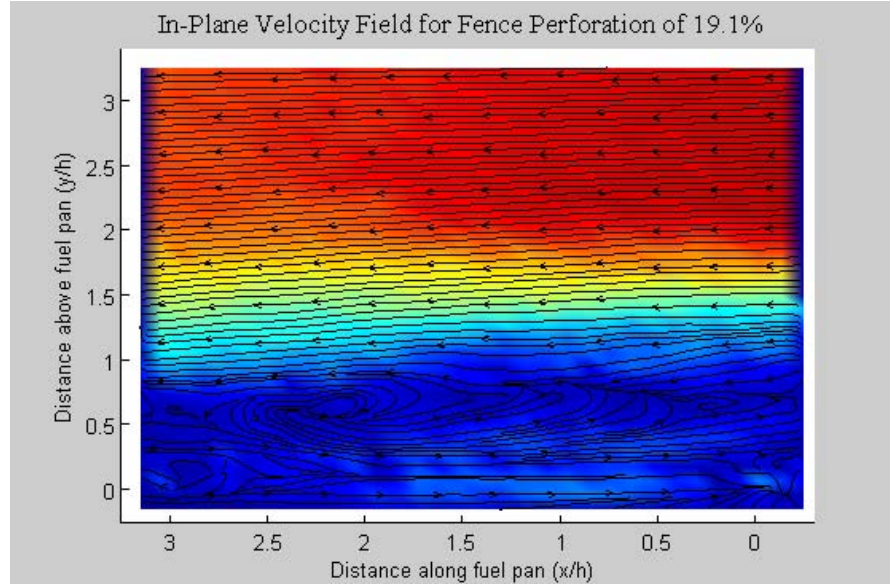


Figure 47. Averaged velocity contour plot with overlaid streamlines at a location over the pan and for a fence perforation of 19.1%. Position along and above the pan are given in non-dimensional units in terms of the fence height. Velocity scale ranges from 0 to 10.5 m/s. The upstream edge of the fuel pan is given by $x/h = 0$.

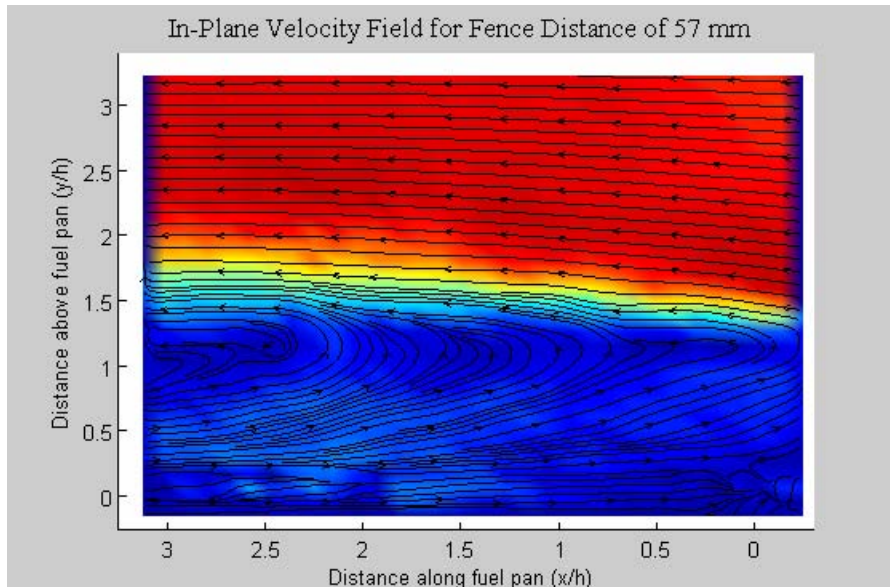


Figure 48. Averaged velocity contour plot with overlaid streamlines at a location over the pan. Fence is located 57 mm upstream of leading edge of pan. Position along and above the pan are given in non-dimensional units in terms of the fence height. Velocity scale ranges from 0 to 10.5 m/s. The upstream edge of the fuel pan is given by $x/h = 0$.

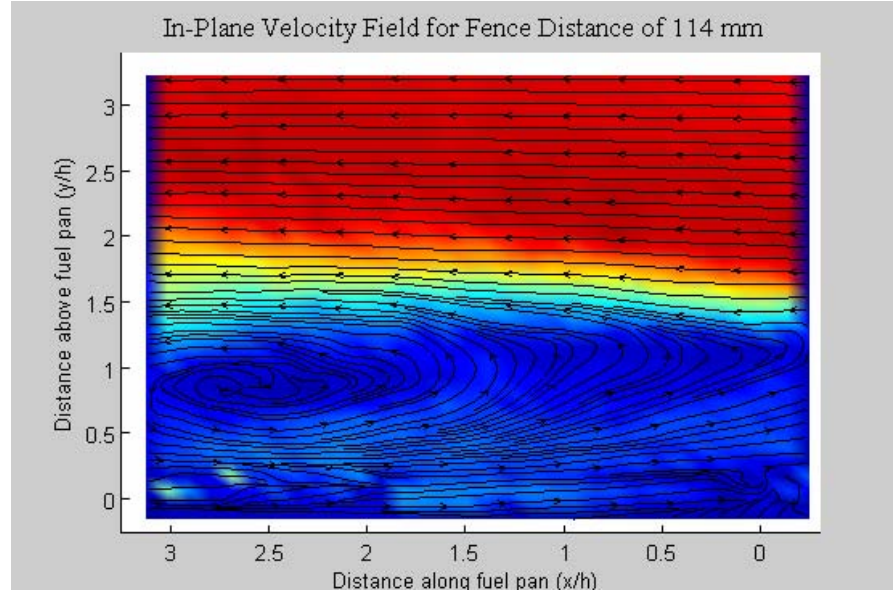


Figure 49. Averaged velocity contour plot with overlaid streamlines at a location over the pan. Fence is located 114 mm upstream of leading edge of pan. Position along and above the pan are given in non-dimensional units in terms of the fence height. Velocity scale ranges from 0 to 10.5 m/s. The upstream edge of the fuel pan is given by $x/h = 0$.

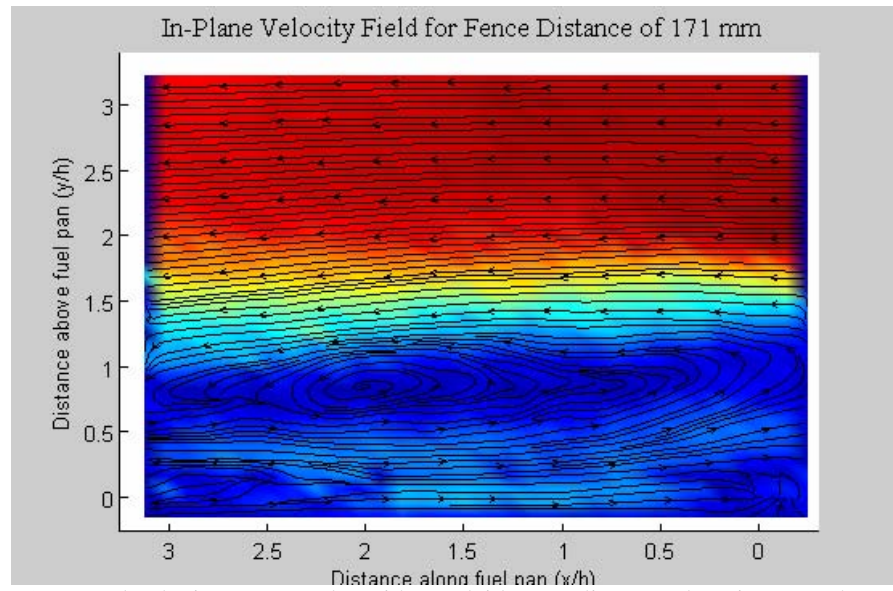


Figure 50. Averaged velocity contour plot with overlaid streamlines at a location over the pan. Fence is located 171 mm upstream of leading edge of pan. Position along and above the pan are given in non-dimensional units in terms of the fence height. Velocity scale ranges from 0 to 10.5 m/s. The upstream edge of the fuel pan is given by $x/h = 0$.

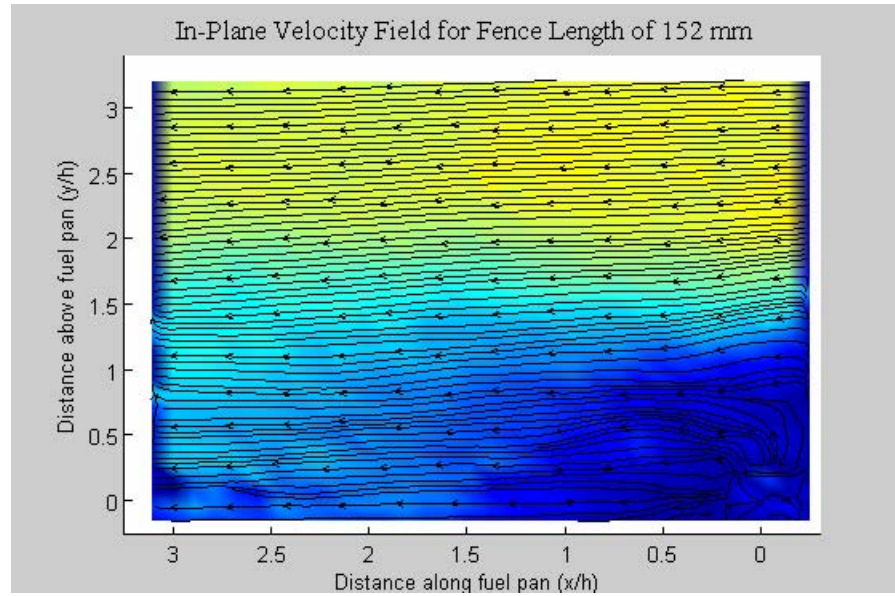


Figure 51. Averaged velocity contour plot with overlaid streamlines at a location over the pan. The fence length is 152 mm along the width of the tunnel and is centered on the pan. Position along and above the pan are given in non-dimensional units in terms of the fence height. Velocity scale ranges from 0 to 10.5 m/s. The upstream edge of the fuel pan is given by $x/h = 0$.

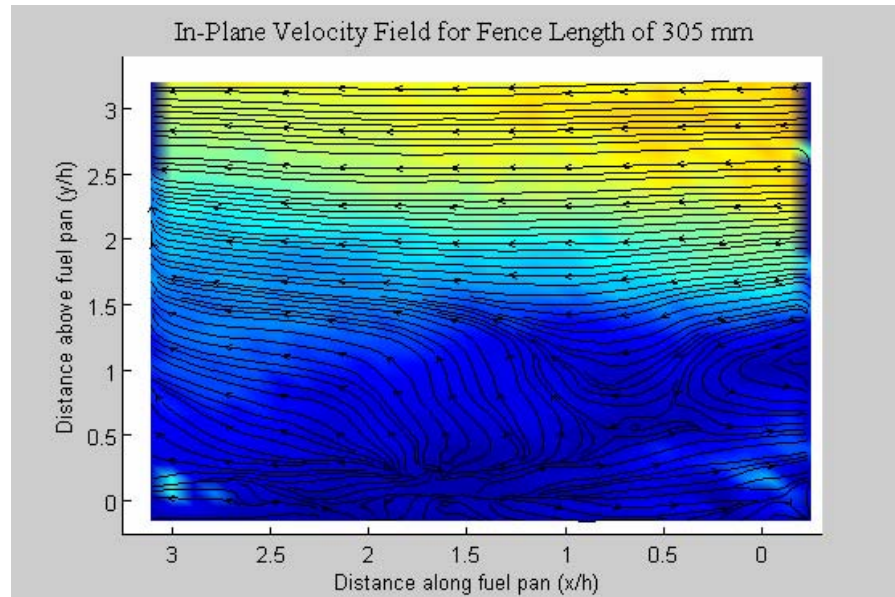


Figure 52. Averaged velocity contour plot with overlaid streamlines at a location over the pan. The fence length is 305 mm along the width of the tunnel and is centered on the pan. Position along and above the pan are given in non-dimensional units in terms of the fence height. Velocity scale ranges from 0 to 10.5 m/s. The upstream edge of the fuel pan is given by $x/h = 0$.

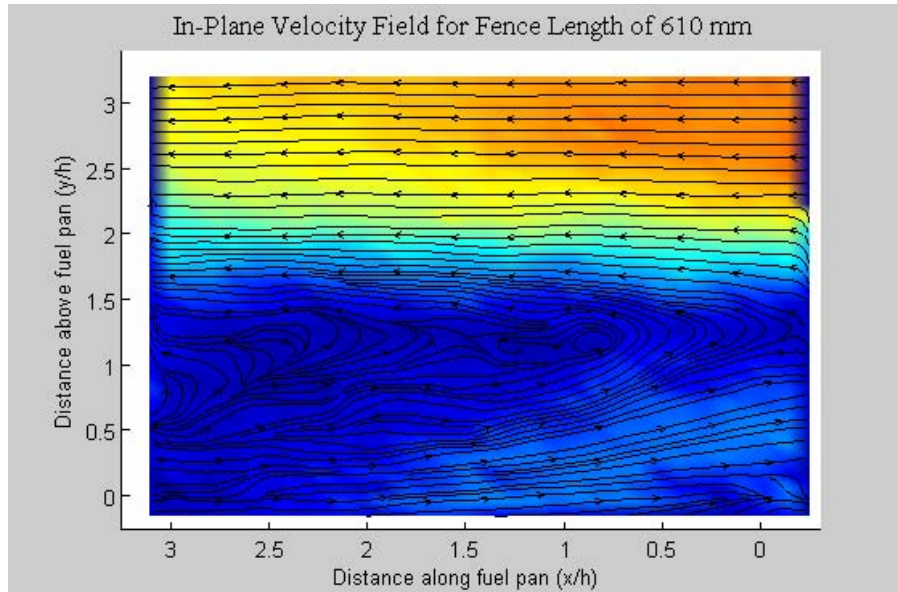


Figure 53. Averaged velocity contour plot with overlaid streamlines at a location over the pan. The fence length is 610 mm along the width of the tunnel and is centered on the pan. Position along and above the pan are given in non-dimensional units in terms of the fence height. Velocity scale ranges from 0 to 10.5 m/s. The upstream edge of the fuel pan is given by $x/h = 0$.

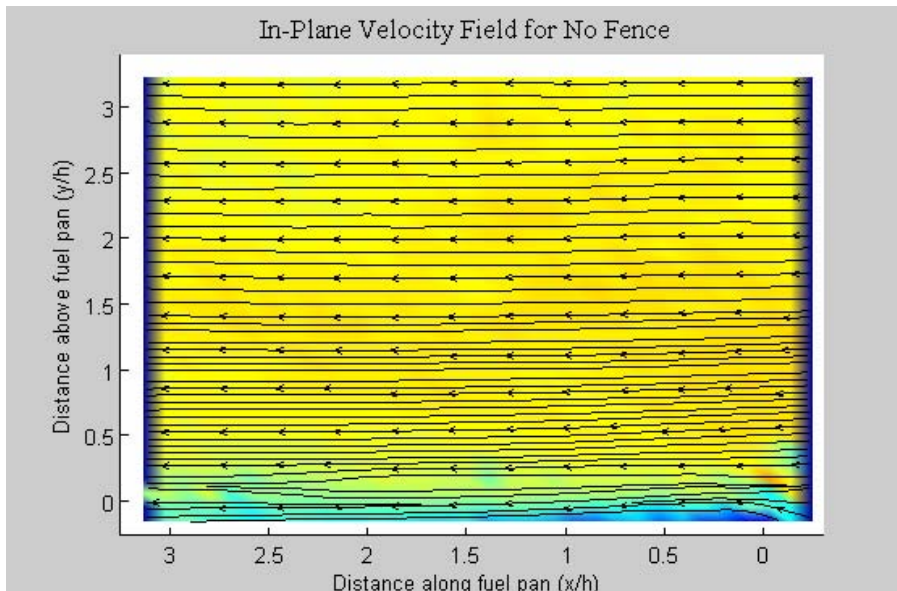


Figure 54. Averaged velocity contour plot with overlaid streamlines at a location over the pan and with no fence in place. Position along and above the pan are given in non-dimensional units in terms of the fence height. Velocity scale ranges from 0 to 10.5 m/s. The upstream edge of the fuel pan is given by $x/h = 0$.

BIBLIOGRAPHY

1. Disimile, P. J., J. R. Tucker, B. Croswell and J. M. Davis. "The Transport of Water Sprays Past Generic Clutter Elements Found Within Engine Nacelles," *Fire Safety Journal*, 40: 65-78 (2005).
2. Hamins, A., D. Baghdadi, P. Borthwick, M. Glover, W. Grosshandler, D. Lowe, L. Melton and C. Presser. "Suppression of Simulated Engine Nacelle Fires," *NIST Annual Conference on Fire Research: Book of Abstracts*, 9-8, 1994.
3. Hamins, A., T. Cleary and J. Yang. "Fire Suppression and Re-ignition Prevention in a Full-Scale Engine Nacelle Simulator," *Fire Safety Science – Proceedings of the Seventh International Symposium*, Worcester, MA. 2002: 703-714.
4. Quintiere, James G. "Surface Flame Spread," in *SFPE Handbook of Fire Protection Engineering*. 3rd ed. 2002, National Fire Protection Association
5. Grosshandler, W., C. Presser, D. Lowe and W. Rinkinen. "Assessing Halon Alternatives for Aircraft Engine Nacelle Fire Suppression," *Journal of Heat Transfer*, 117: 489-501 (1995).
6. Disimile, P. J. and J. M. Davis. "Characterization of a 2-D Pool Fire Simulator," 46th Test Wing, WPAFB.
7. Glassman, I. and F. L. Dryer. "Flame Spreading Across Liquid Fuels," *Fire Safety Journal*, 3: 123-138 (1980).
8. Ross, H. D. "Ignition of and Flame Spread Over Laboratory-Scale Pools of Pure Liquid Fuels," *Prog. Energy Combust. Sci.*, 20: 17-63 (1994).
9. Gottuk, D. T. and D. A. White. "Liquid Fuel Fires," in *SFPE Handbook of Fire Protection Engineering*. 3rd ed. 2002, National Fire Protection Association
10. Akita, K. "Some Problems of Flame Spread Along a Liquid Surface," *Fourteenth Symposium (International) on Combustion*, 1975: 1075-1081.
11. Mackinven, R., J. G. Hansel and I. Glassman. "Influence of Laboratory Parameters on Flame Spread Across Liquid Fuels," *Combust. Sci. and Tech.*, 1: 293-306 (1970).
12. Burgoyne, J. H. and A. F. Roberts. "The Spread of Flame Across a Liquid Surface II. Steady-State Conditions," *Proc. Roy. Soc. A.* 308: 55-68 (1968).

13. Ross, H. D. and F. J. Miller. "Flame Spread Across Liquid Pools With Very Low-Speed Opposed or Concurrent Airflow," *Twenty-Seventh Symposium (International) on Combustion*, Boulder, CO. 1998: 2723-2729.
14. Suzuki, T. and T. Hirano. "Flame Propagation Across a Liquid Fuel in an Air Stream," *Nineteenth Symposium (International) on Combustion*, 1982: 877-883.
15. Schofield W. H. and E. Logan. "Turbulent Shear Flow Over Surface Mounted Obstacles," *Journal of Fluids Engineering*, 112: 376-385 (1990).
16. Durst, F. and A. K. Rastogi. "Turbulent Flow over Two-Dimensional Fences," *2nd Symposium on Turbulent Shear Flows*, London, 1979: 218-232.
17. Roberts, A. F. "Spread of Flame on a Liquid Surface," Ph.D. Thesis. Imperial College, University of London (1959).
18. Sirignano, W. A. and I. Glassman. "Flame Spreading Above Liquid Fuels: Surface Tension-Driven Flows," *Combust. Sci. and Tech.*, 1: 307-312 (1970).
19. Good, M. C. and P. N. Joubert. "The Form Drag of Two-Dimensional Bluff-Plates Immersed in Turbulent Boundary Layers," *J. Fluid Mech.* 31: 547-582 (1968).
20. Santoro, R. J., A. C. Fernandez-Pello, F. L. Dryer, I. Glassman. "Application of a Two-Component LDV to the Measurement of Flows Induced by Flames Propagating Over Condensed Fuels," *Applied Optics*, 17: 3843-3850 (1978).
21. Helmstetter, A. J. MSE Thesis, Dept. Aero. and Mech. Sci., Princeton Univ., Princeton, NJ, 1974.
22. Takeno, K. and T. Hirano. "Behavior of Combustible Liquid Soaked in Porous Beds During Flame Spread," *Twenty-Fourth Symposium (International) on Combustion*, 1988: 1223-1230.
23. White, D., C. L. Beyler, C. Fulper and J. Leonard. "Flame Spread on Aviation Fuels," *Fire Safety Journal*, 28: 1-31 (1997).
24. Akita, K. and O. Fujiwara. "Pulsating Flame Spread along the Surface of Liquid Fuels," *Combustion and Flame*, 17: 268-269 (1971).
25. Ito, A., D. Masuda, and K. Saito. "A Study of Flame Spread Over Alcohols Using Holographic Interferometry," *Combustion and Flame*, 83: 375-389 (1991).
26. Feng, C. C., S. H. Lam and I. Glassman. "Flame Propagation Through Layered Fuel-Air Mixtures," *Combust. Sci. and Tech.*, 10: 59-71 (1975).

27. Zhou, L., A. C. Fernandez-Pello and R. Cheng. "Flame Spread in an Opposed Turbulent Flow," *Combustion and Flame*, 81: 40-49 (1990).
28. Larousse, A., R. Martinuzzi and C. Tropea. "Flow around Surface-Mounted, Three Dimensional Obstacles," *8th Symposium on Turbulent Shear Flows*, Munich, Germnay. 1991: 1-6.
29. "FlowManager Software and Introduction to PIV Instrumentation: Software User's Guide," Dantec Dynamics. Skovlunde, Denmark, 2000.
30. Devore, Jay L. *Probability and Statistics: For Engineering and the Sciences*. Brooks/Cole, 2000.
31. Ellis, R., D. Gullick. "Calculus With Analytic Geometry," 5th ed. Harcourt Publishing, 1998: p. 255.

Vita

Beau was born in Clovis, NM and enjoyed the next few years living in England and Germany. His father, James Brantley, was a USAF Weapon Systems Officer and was eventually assigned to Hanscom AFB in Massachusetts. While living in New England, Beau attended Nashua Senior High School and graduated in 2000. Motivated by a love for the sciences and attracted to the Air Force life style, He decided to attend The University of North Carolina in Charlotte and major in Mechanical Engineering while participating in the ROTC program.

In 2001, Beau transferred to the University of Maryland where he continued ROTC and his previous major and eventually graduated in 2004 with a BSME. He was fortunate enough to be picked up for the direct accession program at AFIT and was provided the opportunity to continue his education in engineering and obtain an MS in Aeronautical Engineering. Upon graduation from AFIT, his next assignment will be to work in the Air Force Research Laboratories for the Propulsion Directorate located at WPAFB.

REPORT DOCUMENTATION PAGE			Form Approved OMB No. 074-0188	
<p>The public reporting burden for this collection of information is estimated to average 1 hour per response, including the time for reviewing instructions, searching existing data sources, gathering and maintaining the data needed, and completing and reviewing the collection of information. Send comments regarding this burden estimate or any other aspect of the collection of information, including suggestions for reducing this burden to Department of Defense, Washington Headquarters Services, Directorate for Information Operations and Reports (0704-0188), 1215 Jefferson Davis Highway, Suite 1204, Arlington, VA 22202-4302. Respondents should be aware that notwithstanding any other provision of law, no person shall be subject to an penalty for failing to comply with a collection of information if it does not display a currently valid OMB control number.</p> <p>PLEASE DO NOT RETURN YOUR FORM TO THE ABOVE ADDRESS.</p>				
1. REPORT DATE (DD-MM-YYYY) 23-03-2006	2. REPORT TYPE Master's Thesis	3. DATES COVERED (From – To) Sep 2004 – Mar 2006		
<p>Quantitative Analysis Of A Turbulent Wind Tunnel With Obstructions For Use In Liquid Flame Spread Experiments</p>			5a. CONTRACT NUMBER	
			5b. GRANT NUMBER	
			5c. PROGRAM ELEMENT NUMBER	
<p>6. AUTHOR(S) Brantley, Beau, M., 2nd Lt, USAF</p>			5d. PROJECT NUMBER	
			5e. TASK NUMBER	
			5f. WORK UNIT NUMBER	
<p>7. PERFORMING ORGANIZATION NAMES(S) AND ADDRESS(S) Air Force Institute of Technology Graduate School of Engineering and Management (AFIT/EN) 2950 Hobson Way WPAFB OH 45433-7765</p>			8. PERFORMING ORGANIZATION REPORT NUMBER AFIT/GAE/ENY/06-M04	
<p>9. SPONSORING/MONITORING AGENCY NAME(S) AND ADDRESS(ES) 46 OG/OGM/AL-OC Attn: Dr. Peter J. Disimile Bldg. 22B WPAFB OH 45433-7765</p>			10. SPONSOR/MONITOR'S ACRONYM(S)	
			11. SPONSOR/MONITOR'S REPORT NUMBER(S)	
<p>12. DISTRIBUTION/AVAILABILITY STATEMENT APPROVED FOR PUBLIC RELEASE; DISTRIBUTION UNLIMITED.</p>				
<p>13. SUPPLEMENTARY NOTES</p>				
<p>14. ABSTRACT The research was done as part of an effort to develop alternative fire suppressant technologies for aircraft engine nacelles. The turbulent shear flow behind a surface mounted fence inside an open circuit wind tunnel was investigated experimentally. The tunnel test section was designed to be 2-D and exhibit flow qualities similar to those found in a typical engine nacelle. A 279 mm wide fuel pan was inserted approximately four fence heights downstream of the fence location. The fuel pan was filled using water to simulate fuel with a depth of 32 mm. Cold flow tests were done on different fence configurations with turbulent airflow. The average turbulence intensity in the streamwise direction was 12% at the forward edge of the pan and with no fence in place. The Reynolds number was 2×10^4 in the free stream and based on a fence height of 50.8 mm. Several fences were used to simulate general types of clutter elements. The height, length, degree of perforation, and distance to the fuel pan were all fence geometries that were tested. Measurements were taken of the 2-D flow field along the centerline of the test section using Particle Image Velocimetry (PIV). A separation region with strong reverse flow was found to exist above the pan and have flow characteristics that were largely sensitive to fence dimensions. It was also found that the results for different configurations can be collapsed using the appropriate non-dimensional parameters.</p>				
<p>15. SUBJECT TERMS Flame Propagation, Turbulent Flow, Clutter, Shear Flow, Particle Image Velocimetry, Liquid Flame Spread, Reverse Flow, Separation, Engine Nacelle, Obstacle</p>				
16. SECURITY CLASSIFICATION OF: REPORT U		17. LIMITATION OF ABSTRACT UU	18. NUMBER OF PAGES 122	19a. NAME OF RESPONSIBLE PERSON Ralph A. Anthenien AFIT/ENY 19b. TELEPHONE NUMBER (Include area code) (937) 255-3636 x4643; e-mail: @afit.edu

Standard Form 298 (Rev: 8-

98)

Prescribed by ANSI Std. Z39-18